Monthly Notices of the ROYAL ASTRONOMICAL SOCIETY

MNRAS **473,** 2020–2059 (2018) doi:10.1093/mnras/stx2279

The optical + infrared L dwarf spectral sequence of young planetary-mass objects in the Upper Scorpius association

N. Lodieu,[1,2]★ M. R. Zapatero Osorio,[3] V. J. S. Béjar[1,2] and K. Peña Ramírez[4]

[1]*Instituto de Astrofísica de Canarias (IAC), C/ Vía Láctea s/n, E-38200 La Laguna, Tenerife, Spain*
[2]*Departamento de Astrofísica, Universidad de La Laguna (ULL), E-38206 La Laguna, Tenerife, Spain*
[3]*Centro de Astrobiología (CSIC-INTA), Carretera de Ajalvir km 4, 28850 Torrejón de Ardoz, Madrid*
[4]*Unidad de Astronomía, Facultad de CsḂásicas, Universidad de Antofagasta, Av. U. de Antofagasta 02800, Antofagasta, Chile*

Accepted 2017 August 31. Received 2017 August 31; in original form 2017 March 31

ABSTRACT

We present the results of photometric and spectroscopic follow-ups of the lowest mass member candidates in the nearest OB association, Upper Scorpius (∼5–10 Myr; 145 ± 17 pc), with the Gran Telescopio de Canarias (GTC) and European Southern Observatory (ESO) Very Large Telescope (VLT). We confirm the membership of the large majority (>80 per cent) of candidates originally selected photometrically and astrometrically based on their spectroscopic features, weak equivalent widths of gravity-sensitive doublets and radial velocities. Confirmed members follow a sequence over a wide magnitude range ($J = 17.0$–19.3 mag) in several colour–magnitude diagrams with optical, near- and mid-infrared photometry and have near-infrared spectral types in the L1–L7 interval with likely masses below 15 Jupiter masses. We find that optical spectral types tend to be earlier than near-infrared spectral types by a few subclasses for spectral types later than M9. We investigate the behaviour of spectral indices, defined in the literature as a function of spectral type and gravity, by comparison with values reported in the literature for young and old dwarfs. We also derive effective temperatures in the 1900–1600 K range from fits of synthetic model-atmosphere spectra to the observed photometry, but we caution that the procedure carries large uncertainties. We determine bolometric corrections for young L dwarfs with ages of ∼5–10 Myr (Upper Sco association) and find them to be similar in the J band but larger by 0.1–0.4 mag in the K band with respect to field L dwarfs. Finally, we discover two faint young L dwarfs, Visible and Infrared Survey Telescope for Astronomy (VISTA) J1607−2146 (L4.5) and VISTA J1611−2215 (L5), that have Hα emission and possible flux excesses at 4.5 μm, pointing to the presence of accretion from a disc on to the central objects of mass below $\sim 15 M_{\rm Jup}$ at an age of 5–10 Myr.

Key words: techniques: photometric – techniques: spectroscopic – surveys – brown dwarfs – stars: low-mass – stars: luminosity function, mass function.

1 INTRODUCTION

Various independent groups have explored the very low-mass end of the initial mass function (IMF: Salpeter 1955; Miller & Scalo 1979; Scalo 1986; Chabrier 2005; Kroupa et al. 2013) in young clusters and star-forming regions, following L- to T-type spectral sequences. Barrado y Navascués et al. (2007) conducted a deep ($K \sim 17$ mag) 1-deg^2 survey in λ Orionis down to the low-mass and substellar regimes, with subsequent optical and near-infrared spectroscopy (Bayo et al. 2011) and in-depth study of the physical properties of the confirmed members (Bayo et al. 2012). Scholz et al. (2009) reported a possible mass cut-off in NGC 1333 in the range 0.02–0.012 $M_\odot$ from a deep photometric and spectroscopic survey of 0.25 deg^2 down to $J = 20.8$ mag with a spectroscopic follow-up (Scholz et al. 2012a). The census of spectroscopic members in this region is now complete down to ∼0.01 $M_\odot$ at an age of 3 Myr (Luhman, Esplin & Loutrel 2016). In IC 348, Alves de Oliveira et al. (2013) presented optical and near-infrared spectroscopy of late-M/early-L dwarf candidates, while Burgess et al. (2009) reported one high-probability T-type candidate. The current census of spectroscopic members in IC 348 amounts to 478 objects down to $K = 16.2$ mag and $A_J < 3$ mag (Luhman et al. 2016). In σ Orionis, Peña Ramírez et al. (2012) reported 23 new candidates, extending the previous mass functions (e.g. Zapatero Osorio et al. 2000; Béjar et al. 2001, 2011; Caballero et al. 2007; Bihain et al. 2009; Lodieu et al. 2009) down to a completeness of 0.006 $M_\odot$. The membership of T-type sources (Zapatero Osorio et al. 2000, 2002, 2008;

★ E-mail: nlodieu@iac.es

Burgasser et al. 2004) towards the cluster was revised in Peña Ramírez et al. (2011) and Peña Ramírez, Zapatero Osorio & Béjar (2015). Many independent surveys investigated the substellar population of the Orion nebula cluster spectroscopically (Lucas et al. 2001; Weights et al. 2009; Hillenbrand, Hoffer & Herczeg 2013; Ingraham et al. 2014; Suenaga et al. 2014). In ρ Oph, Geers et al. (2011) selected member candidates from a deep ($J = 20.6$ mag) multi-band survey of 0.25 deg^2, with near-infrared spectroscopic follow-up down to the deuterium-burning limit (Mužić et al. 2012). In the same region, Alves de Oliveira et al. (2012) presented optical spectroscopy of brown dwarf candidates as faint as $J \sim 20.5$ mag (Alves de Oliveira et al. 2010), casting doubts about the membership of the T2-type member (Marsh, Kirkpatrick & Plavchan 2010) identified in a deep near-infrared survey (Marsh et al. 2010). Chiang & Chen (2015) presented two young early T-type candidates as well as an L-type dwarf identified in their methane and mid-infrared survey (Chiang et al. 2015). In Serpens, Spezzi et al. (2012) reported a few T-type candidates that require additional follow-up before deriving the IMF below the deuterium-burning limit. In Lupus-3, Mužić et al. (2014) conducted an optical and near-infrared survey of 1.4 deg^2 down to planetary masses (0.009 $M_\odot$ or $J = 18.3$ mag) with one probable new brown dwarf (Mužić et al. 2015). In more mature clusters, Zapatero Osorio et al. (2014) confirmed seven early-L and L/T transition members in the Pleiades, with masses in the 0.035–0.010 $M_\odot$ range from a deep *JH* 0.8-deg^2 survey (Zapatero Osorio et al. 2014). Bouvier et al. (2008) confirmed astrometrically and spectroscopically two early-T dwarfs with masses around 0.05 $M_\odot$ in a deep optical survey of 16 deg^2 in the 625-Myr-old Hyades cluster.

The spectroscopic characterization of L dwarf members of young open clusters and star-forming regions has revealed key features sensitive to gravity. After photometric selection and astrometric confirmation (when possible depending on the mean proper motion of the cluster/region), weak gravity-sensitive features such as alkali lines (e.g. the potassium and sodium doublets) at optical and infrared wavelengths add strong credit to the membership of candidates (Martín, Rebolo & Zapatero Osorio 1996; Luhman et al. 1998; McLean et al. 2000; Martín et al. 2001b; Gorlova et al. 2003). Other criteria include weaker hydride (e.g. FeH and CrH) and stronger oxide (e.g. VO, TiO) bands (Kirkpatrick et al. 2006) and the presence of the triangular or peaked shape of the *H*-band spectra (Lucas et al. 2001), which, together with the aforementioned features, are well-accepted low-surface-gravity features (Zapatero Osorio et al. 2000; Martín & Zapatero Osorio 2003; Lodieu et al. 2008; Cruz, Kirkpatrick & Burgasser 2009; Scholz et al. 2012b; Allers & Liu 2013; Bonnefoy et al. 2014; Manjavacas et al. 2014; Mužić et al. 2014, 2015; Martin et al. 2017).

Upper Scorpius (hereafter UpSco) is part of the nearest OB association to the Sun, Scorpius Centaurus. The region is nearby, with a distance of ∼145 pc from *Hipparcos* (de Bruijne et al. 1997) and a recent update from *Gaia* (144.2 ± 17.6 pc: Fang, Herczeg & Rizzuto 2017). UpSco is young, with different age determinations and a possible spread among its members (Preibisch & Zinnecker 1999; Preibisch, Guenther & Zinnecker 2001; Pecaut, Mamajek & Bubar 2012; Song, Zuckerman & Bessell 2012; Pecaut 2016; Rizzuto et al. 2016). The members of UpSco exhibit a significant mean proper motion ($\mu_\alpha \cos\delta = -10.5$ and $\mu_\delta = -23.2$ mas yr^{-1}, with a standard dispersion of about 6.4 mas yr^{-1}: de Bruijne et al. 1997; de Zeeuw et al. 1999; Fang et al. 2017). The bright end of the UpSco population has been examined in X-rays (Walter et al. 1994; Kunkel 1999; Preibisch et al. 1998), astrometrically (de Bruijne et al. 1997; de Zeeuw et al. 1999) and spectroscopically (Preibisch & Zinnecker 2002). The low-mass and substellar population has been investigated over the past decade in great detail with the advent of modern detectors, permitting wide and/or deep surveys (Ardila, Martín & Basri 2000; Martín, Delfosse & Guieu 2004; Slesnick, Carpenter & Hillenbrand 2006; Lodieu, Hambly & Jameson 2006; Lodieu et al. 2007, 2011b; Kraus et al. 2008; Béjar et al. 2008; Slesnick, Hillenbrand & Carpenter 2008; Lafrenière, Jayawardhana & van Kerkwijk 2010; Dawson, Scholz & Ray 2011; Lafrenière et al. 2011, 2014; Dawson et al. 2013, 2014; Lodieu 2013; Peña Ramírez, Béjar & Zapatero Osorio 2016; Best et al. 2017). The first transiting systems in the association have been announced in the last years, thanks to the *Kepler* K2 mission (Borucki et al. 2010; Lissauer, Dawson & Tremaine 2014; Batalha 2014), including a triple system composed of an F star and two solar-type stars (Alonso et al. 2015) and several M dwarf eclipsing binaries (Kraus et al. 2015; Lodieu et al. 2015; David et al. 2016). These systems are of prime importance, because they provide the first mass and radius measurements independent of models in this region. Finally, we should note the existence of a transiting Neptune-size planet candidate around an M3 member of UpSco (Mann et al. 2016; David et al. 2016).

Our group has recently identified several tens of substellar and isolated planetary-mass candidates from a deep infrared survey of 13.5 deg^2 in the central region of UpSco (Lodieu et al. 2013, hereafter L13), which represents the basis of the work presented in this article. This photometric survey is among the widest and deepest in a young star-forming region, to investigate the shape of the IMF at very low masses. Here, we present optical photometry in the Sloan *i* filter obtained with the Optical System for Imaging and low Resolution Integrated Spectroscopy (OSIRIS: Cepa et al. 2000) on the 10.4-m Gran Telescopio de Canarias (GTC). We also present optical and near-infrared spectroscopy of photometrically confirmed member candidates with GTC/OSIRIS and the European Southern Observatory (ESO) Very Large Telescope (VLT) X-shooter spectrograph (Vernet et al. 2011). In Section 2, we describe the optical photometric observations obtained with the GTC and its associated data reduction. In Section 3, we detail the spectroscopic follow-up conducted with ESO VLT for 15 member candidates in UpSco, including optical spectroscopy of a subsample with GTC/OSIRIS. In Section 4, we show mid-infrared photometry from the AllWISE: Wide Field Infrared Survey Explorer (Wright et al. 2010) public catalogue for the coolest UpSco members. In Section 5, we present an analysis of the photometric and spectroscopic properties of the L-type members in UpSco and discuss their membership and physical properties. We define the first sequence for young L-dwarf members of the UpSco association with an age of ∼5–10 Myr. In the literature, it has been shown that the low-gravity sequence of L dwarfs does not logically flow from the high-gravity sequence. In this article, we are looking to create a uniform sample from the UpSco objects, which have the same metallicity and age.

2 OPTICAL PHOTOMETRY WITH GTC

2.1 SDSS *i* photometry

The OSIRIS instrument (Cepa et al. 2000) is mounted on the 10.4-m GTC operating at the Observatory del Roque de Los Muchachos (La Palma, Canary Islands). The detector consists of two 2048 × 4096 Marconi CCD42-82 with an 8-arcsec gap between them and operates at optical wavelengths from 0.365–1.0 μm. The unvignetted instrument field of view is about 7 × 7 arcmin^2 with an unbinned pixel scale of 0.125 arcsec. We employed a 2 × 2 binning, because

Table 1. Logs of the GTC OSIRIS photometric observations. We list the names of the targets according to the IAU nomenclature, coordinates in sexagesimal format (J2000), *J* magnitudes from VISTA (L13; MKO system), dates of observations, number of repeated on-source integration times, seeing rounded to the nearest digit, mean airmass, Sloan *i*-band magnitudes (AB system) measured for the GTC/OSIRIS images with their uncertainties (values quoted without errors are 3σ limits) and derived $i - J$ colours (or lower limits).

Name VISTA *J*	RA hh:mm:ss.ss	Dec. °:′:″	ExpT sec	Date yyyy-mm-dd	Seeing arcsec	Airmass	SDSS *i* mag	$i - J$ mag
16073161−2146544	16:07:31.61	−21:46:54.4	11×60	2014-08-27	0.7	1.87	23.42 ± 0.21	5.38 ± 0.27
16041304−2241034	16:04:13.04	−22:41:03.4	11×60	2014-08-28	0.8	1.87	22.16 ± 0.22	3.99 ± 0.23
16140756−2211522	16:14:07.56	−22:11:52.2	11×60	2014-08-23	1.3	1.92	22.65 ± 0.28	4.39 ± 0.28
16084343−2245162	16:08:43.43	−22:45:16.2	11×60	2014-08-23	1.3	1.86	23.08 ± 0.21	3.48 ± 0.64
16053909−2403328	16:05:39.09	−24:03:32.8	11×60	2014-08-23	1.3	1.84	23.18 ± 0.26	4.86 ± 0.26
16042042−2134530	16:04:20.42	−21:34:53.0	11×60	2014-08-31	1.2	1.89	22.32 ± 0.22	3.91 ± 0.23
16020000−2057341	16:02:00.00	−20:57:34.1	11×60	2014-08-21	0.9	1.80	22.77 ± 0.21	4.27 ± 0.21
16041234−2127470	16:04:12.34	−21:27:47.0	11×60	2014-08-24	1.3	1.79	22.69 ± 0.21	4.17 ± 0.22
16082915−2116296	16:08:29.15	−21:16:29.6	11×60	2014-08-21	0.9	1.70	23.24 ± 0.22	4.55 ± 0.22
16013692−2212027	16:01:36.92	−22:12:02.7	30×60	2014-08-01	1.2	1.80	23.67 ± 0.23	4.40 ± 0.24
16151270−2229492	16:15:12.70	−22:29:49.2	30×60	2014-08-17	1.5	1.79	23.50 ± 0.22	4.16 ± 0.23
16114892−2105286	16:11:48.92	−21:05:28.6	30×60	2014-08-18	1.6	1.69	>24.05	>4.38
16162104−2355201	16:16:21.04	−23:55:20.1	30×60	2014-08-12	0.9	1.62	>24.05	>4.05
16125183−2316500	16:12:51.83	−23:16:50.0	30×60	2014-08-16	0.9	1.74	23.91 ± 0.23	4.07 ± 0.25
16130655−2255327	16:13:06.55	−22:55:32.7	30×60	2014-08-03	0.9	1.68	22.45 ± 0.21	2.65 ± 0.23
16102763−2305543	16:10:27.63	−23:05:54.3	30×60	2014-08-11	0.9	1.71	21.26 ± 0.20	1.26 ± 0.25
16091868−2229239	16:09:18.68	−22:29:23.9	11×60	2014-08-26	0.9	1.70	22.87 ± 0.21	4.93 ± 0.25
16114437−2215446	16:11:44.37	−22:15:44.6	11×60	2014-08-24	1.0	1.71	22.45 ± 0.21	4.59 ± 0.26
16051705−2130449	16:05:17.05	−21:30:44.9	10×60	2014-08-28	0.8	1.88	22.33 ± 0.21	3.95 ± 0.21
16142256−2331178	16:14:22.56	−23:31:17.8	2×60	2014-08-28	0.8	1.91	21.74 ± 0.21	4.29 ± 0.21
16130231−2124285	16:13:02.31	−21:24:28.5	1×65	2014-08-28	0.8	2.05	21.96 ± 0.21	4.78 ± 0.21
15593638−2214159	15:59:36.38	−22:14:15.9	1×65	2014-08-31	1.7	2.00	21.80 ± 0.21	4.83 ± 0.21
16072782−2239042	16:07:27.82	−22:39:04.2	1×70	2014-08-28	0.8	2.20	21.14 ± 0.21	4.28 ± 0.21
16161064−2151243	16:16:10.64	−21:51:24.3	1×65	2014-08-28	0.8	2.17	20.32 ± 0.20	3.69 ± 0.20
16071478−2321013	16:07:14.78	−23:21:01.3	2×60	2014-08-28	0.8	2.33	20.89 ± 0.21	4.33 ± 0.21
16130140−2142547	16:13:01.40	−21:42:54.7	1×60	2014-08-28	0.8	2.07	19.94 ± 0.20	3.62 ± 0.20
16060629−2335135	16:06:06.29	−23:35:13.5	2×60	2014-08-31	1.6	2.26	under spike	–
16064554−2121593	16:06:45.54	−21:21:59.3	2×60	2014-08-31	1.6	2.12	20.45 ± 0.20	4.31 ± 0.20
16081842−2232252	16:08:18.42	−22:32:25.2	2×60	2014-08-28	0.8	2.25	20.26 ± 0.20	4.17 ± 0.20

it is currently the standard mode of observations. We placed all targets in the CCD2, because it provides the largest unvignetted field of view.

The observations were conducted in service during 2014 August over several days (programme GTC4-14A; PI Lodieu). We list the dates of observations, exposure times, mean seeing at the time of observations and airmass in Table 1. The conditions at the time of the observations were grey and clear or photometric, except on 2014 August 28. However, the exposure times, seeing conditions and airmass at the time of observations span wide ranges, resulting in a globally inhomogeneous photometric data set. Bias and skyflats were obtained during the afternoon or morning of the respective nights. A photometric standard star was also observed with the same instrumental configuration as the science targets as part of the GTC calibration plan, except for the nights of 2014 August 1, 11, 17, 27 and 28. Four different standards were taken over the full period of observations for our programme (SA 110-232, G 158-100, PG 1528, SA 109-381).

We imaged 31 member candidates in the UpSco association published by L13. We used mainly individual on-source integrations of 60 sec repeated many times to detect (or attempt a detection of) all UpSco candidates. The 60-sec integration is set by the brightness of the sky in the Sloan *i* filter, where exposures longer than 120 s usually saturate the detector completely. Table 1 provides the coordinates of the UpSco targets, along with the measured *i*-band magnitudes and inferred $i - J$ colours. We plot the positions of the GTC OSIRIS pointings in Fig. 1.

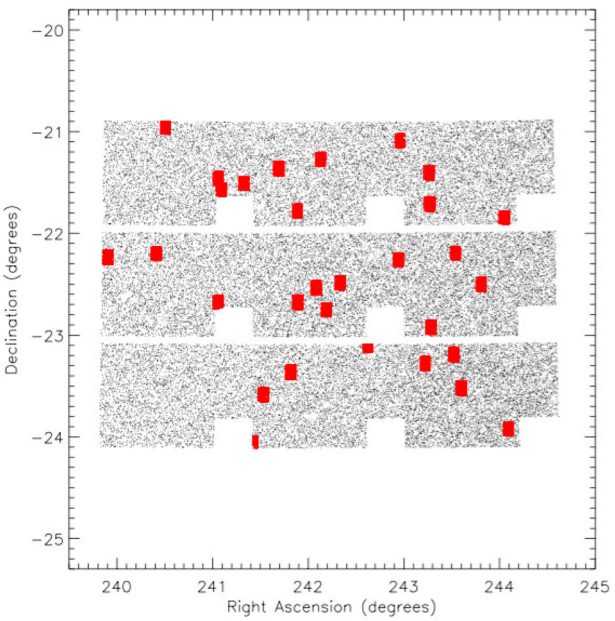

Figure 1. Location of the GTC OSIRIS CCD2 pointing (red regions) overlapping with the deep VISTA *ZYJ* survey (L13; light grey; only 1 every 20 sources plotted). Some of the GTC fields do not overlap fully with the VISTA survey.

2.2 Data reduction and photometry

We reduced the OSIRIS optical images in a standard manner under the IRAF environment[1] (Tody 1986, 1993). We considered only the CCD2 of the detector where the target was located. First, we subtracted the median-combined bias and divided every single raw frame by the median-combined flat-field. Then, we averaged all frames to produce a final combined image for each target. All OSIRIS pointings contain one single UpSco target, keeping in mind that the Visible and Infrared Survey Telescope for Astronomy (VISTA) survey covered 13.5 deg^2 of UpSco (Fig. 1), except in one case where two nearby sources were placed in the same OSIRIS field of view to save telescope time.

First, we calibrated the combined images astrometrically with a sequence of IRAF tasks: `ccxymatch`, `ccmap` and `mscimage`. We identified bright sources with their pixel coordinates using `daofind` with a 10σ detection threshold and used the 2MASS point-source catalogue (Cutri et al. 2003; Skrutskie et al. 2006) as a reference to convert pixels into the world coordinate system. We included non-linear distortion terms to the tangent plane projection due to the slight rotation of the detector on the focal plane creating distortions at the edges of the images. We found that the x-axis is rotated by 180° towards the east and the y-axis by 1/10°. The precision of the final astrometry solution is of the order of or better than 0.15 arcsec for both axes.

We performed aperture and point-spread function (PSF) photometry with the task `phot` in IRAF. The full catalogue of sources in all OSIRIS pointings contains 15 354 objects. The depths of the combined images vary from pointing to pointing because of the observing strategy, which was strongly dependent on the on-source integration times (see Table 1) and the distinct airmass and seeing conditions at the time of observations. We adapted the photometric aperture to the seeing conditions of each combined image, choosing apertures of the order of four times the full width at half-maximum (FWHM).

We divided our candidates into two groups to perform aperture photometry.

(i) For candidates detected clearly in the OSIRIS images, we extracted the photometry directly from the full catalogue (red filled dots in Fig. 2).

(ii) For the two remaining candidates below the 3σ limit of detection (VISTA J16114892−2105286 and VISTA J16162104−2355201), we estimated the limited magnitudes as three times the root-mean-square (rms) at the expected location of the candidates as their flux peak and compared these with the peak fluxes of three nearby isolated and well-detected stars with measured photometry (red arrows in Fig. 2).

To calibrate the OSIRIS images photometrically, we proceeded as follows: we obtained PSF photometry for both the target data and the standard stars using a zero-point of 25 mag as a starting point. The derived photometric zero-points from the standard stars agree within ± 0.05 mag with those published by the observatory. For the targets observed on the nights with no photometric standard star available, we calibrated photometrically using the following procedure. First, we cross-matched the catalogue of OSIRIS sources with the full VISTA+UKIDSS GCS catalogue. We produced a histogram of the $i - H$ colours for all sources in the non-calibrated fields using the instrumental magnitudes in the i band and compared them with the combination of the same histograms of the UpSco fields with already calibrated photometry using standard stars. We shifted instrumental magnitudes in the i band to match the distribution of both histograms and convert them into apparent magnitudes. The uncertainty of this procedure is limited to the dispersion of the histograms and can be as high as 0.15–0.20 mag. We added this calibration error in quadrature to the photometric uncertainties derived from `phot` in IRAF.

The final i-band magnitudes and their uncertainties (in the case of detections) are listed in Table 1, along with the associated $i - J$ colours. The error bars are dominated by the photometric calibration in most cases. We display the ($i - J$, J) colour–magnitude diagram with all optical detections with infrared counterparts in Fig. 2. We highlighted our candidates with larger symbols and 3σ non-detections with right-pointing arrows. We conclude that most of our photometric candidates remain as potential UpSco members based on optical-to-near-infrared indices. Only two sources, VISTA J16130655−2255327 and J16102763−2305543, have blue $i - J$ colours that might indicate that they are field contaminants. This suggests that the minimum level of contamination in our original photometric sample is of the order of ∼7 per cent. For comparison, we overplotted the sequence of field M and L dwarfs from M5–L8 from the Sloan team (West et al. 2008; Schmidt et al. 2010) shifted to a distance of 145 pc.

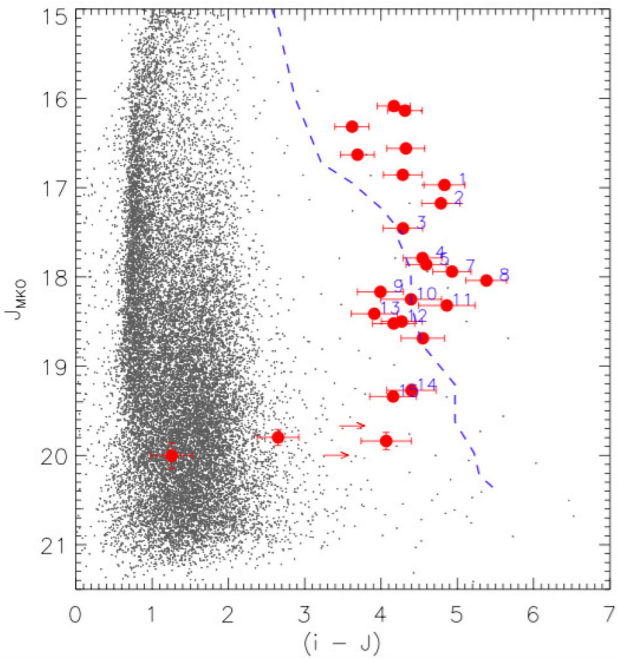

Figure 2. ($i - J$, J) colour–magnitude diagram for all sources in the GTC OSIRIS CCD2 field of view (grey dots) with infrared photometry from the deep *ZYJ* VISTA survey (L13). Overplotted as red dots are the *ZYJ* candidates detected in GTC OSIRIS. We give lower limits for two objects (VISTA J16114892−2105286 and VISTA J16162104−2355201). The two objects with the bluest $i - J$ colours are VISTA J16130655−2255327 and VISTA J16102763−2305543, marked with a right-pointing red arrow. Blue numbers correspond to IDs as in Table 4. Overplotted as a blue dashed line is the sequence of M and L dwarfs (M5–L8) from SDSS shifted to the distance of UpSco.

[1] IRAF is distributed by National Optical Astronomy Observatory, which is operated by the Association of Universities for Research in Astronomy, Inc., under contract with the National Science Foundation.

3 SPECTROSCOPIC DATA SETS

3.1 VLT/X-shooter spectroscopy

We carried out spectroscopy from the UV- to the *K* band with the X-shooter spectrograph (D'Odorico et al. 2006; Vernet et al. 2011) mounted on the Cassegrain focus of the Very Large Telescope (VLT) Unit 2. X-shooter is a multi wavelength cross-dispersed echelle spectrograph made of three independent arms, simultaneously covering the ultraviolet (UVB: 0.3–0.56 μm), visible (VIS: 0.56–1.02 μm) and near–infrared (NIR: 1.02–2.48 μm) wavelength ranges, thanks to the presence of two dichroics splitting the light. The spectrograph is equipped with three detectors: a 4096×2048 E2V CCD44-82, a 4096×2048 MIT/LL CCID 20 and a 2096×2096 Hawaii 2RG for the UVB, VIS and NIR arms, respectively.

3.1.1 New X-shooter near-infrared spectroscopy

We performed our observations in visitor mode during the second half of four nights on 2015 April 11–14. We set the read-out mode to 400k and low gain without binning. We used the 1.3-arcsec slit in the UVB and 1.2-arcsec slits in the VIS and NIR, yielding nominal resolving powers of 4000 (8.1 pixels per FWHM), 6700 (7.9 pixels per FWHM) and 3900 (5.8 pixels per FWHM) in the UVB, VIS and NIR arms, respectively. Conditions during the first part of the second half on the night of April 11 were affected by thin cirrus but the seeing remained around 1.0 arcsec or better. The third target, VISTA J16020000−2057341, turns out to be the most affected by cirrus, which increased in size and number during the observing blocks. The sky was clear and the seeing sub-arcsec during the remaining half nights. In addition, we retrieved the X-shooter spectra of six previously known UpSco members with optical spectral types, as well as another seven M/L-type transition members confirmed spectroscopically (Table 3), all of them belonging to the sequence of VISTA candidates (L13). We report the list of targets and detailed logs of observations in Table 4.

We set the individual on-source integration times to 300 s in the NIR arm and used multiple AB patterns to correct for the sky contribution (mainly) in the near-infrared. All observations were conducted with the slit oriented at the parallactic angle. We acquired the faintest targets ($J \geq 17.5$ mag) with blind offsets, i.e. we pointed to a bright star within 30 arcsec or less and applied an offset using the positions of the bright star and the target measured on the deep VISTA images. We provide the coordinates of the targets observed with X-shooter and their *J*-band magnitudes in Table 4. We also give the dates of the observations, number of exposures and individual on-source integrations in each arm. We did not detect any of our targets in the UVB region and saw little flux in the VIS arm even for the brightest sources, so we focus on the data reduction and analysis of the NIR spectra only in the rest of the article.

3.1.2 Data reduction of X-shooter spectra

We reduced the X-shooter NIR spectra of 15 targets listed in Table 4 with the `esoreflex` pipeline version 2.8.1. It is a graphical interface using a sequence of command lines from the `esorex` package that produces fully calibrated 2D and 1D spectra. The pipeline includes the following steps: first a bad pixel map is created using a set of 40 linearity frames taken within 10 days of our run to identify

Table 2. Cross-match between the catalogue of GTC OSIRIS *i*-band (SDSS AB system) and the deep *ZYJ* (MKO system) VISTA catalogue. Columns 1 and 2 give the coordinates (J2000) for the GTC OSIRIS images in sexagesimal format; columns 3 and 4 give the coordinates for the GTC OSIRIS images in pixels; column 5 provides the *i*-band photometry and its uncertainty; columns 6 and 7 give the coordinates for the VISTA images in sexagesimal format; columns 8–10 provides the VISTA *ZYJ* photometry and its error bars; columns 11–13 give the classification of the source according to the UKIDSS scheme (negative and positive values indicate point sources and galaxies, respectively: Lawrence et al. 2007); column 14 gives the separation between the positions on the GTC and VISTA images. The full version of this table will be available in the electronic version of the article.

RA (GTC)	Dec. (GTC)	*xc*	*yc*	*i*	RA (VISTA)	Dec. (VISTA)	*Z*	*Y*	*J*	*z* Class	*y* Class	*j* Class	Sep
hh:mm:ss.ss	°:′:″	pix	pix	mag	hh:mm:ss.ss	°:′:″	mag	mag	mag				arcsec
15:59:22.34	−22:14:26.9	975.417	936.077	20.188 ± 0.047	15:59:22.34	−22:14:27.3	20.007 ± 0.020	19.703 ± 0.046	19.482 ± 0.081	−1	−1	−1	0.382
...	...	...	...	...	...	...	...	...	...	...	...	...	...
16:16:24.47	−23:51:50.9	21.189	1776.340	17.189 ± 0.002	16:16:24.48	−23:51:51.0	16.948 ± 0.004	16.699 ± 0.004	16.335 ± 0.005	−1	−1	−1	0.119

Table 3. Coordinates (J2000), magnitudes (*ZYJ* from VISTA and *HK* from the UKIDSS Galactic Clusters Survey, all in the MKO system) and spectral types of candidates previously confirmed as members of the UpSco association. LM12 stands for Luhman & Mamajek (2012), L08a for Lodieu et al. (2008), H09 for Herczeg, Cruz & Hillenbrand (2009) and L11a for Lodieu, Dobbie & Hambly (2011a). Objects observed with VLT/X-shooter and publicly available from the ESO archive are highlighted in the last column with 'XSH'.

RA	Dec.	*Z* mag	*Y* mag	*J* mag	*H* mag	*K* mag	SpT	References
16:00:43.17	−22:29:14.5	17.112 ± 0.004	16.051 ± 0.003	15.197 ± 0.003	14.646 ± 0.006	14.174 ± 0.004	M6.5	LM12
16:06:03.75	−22:19:30.2	18.292 ± 0.007	16.911 ± 0.004	15.811 ± 0.004	15.112 ± 0.008	14.416 ± 0.005	M8.75,L2	LM12,L08a
16:06:06.29	−23:35:13.5	–	17.220 ± 0.007	16.231 ± 0.006	15.619 ± 0.012	14.999 ± 0.010	L0,M8.5	L08a,LM12,XSH
16:07:14.78	−23:21:01.3	19.090 ± 0.015	17.677 ± 0.009	16.561 ± 0.007	15.807 ± 0.016	15.103 ± 0.009	M9.25,L0	LM12,L08a
16:07:23.81	−22:11:02.1	17.270 ± 0.004	16.045 ± 0.003	15.145 ± 0.003	14.565 ± 0.006	13.995 ± 0.004	M7.5,M8.5,L1	H09,L11a,L08a,XSH
16:07:27.82	−22:39:04.2	19.478 ± 0.015	18.014 ± 0.009	16.856 ± 0.008	16.153 ± 0.021	15.471 ± 0.013	M9,L1	LM12,L08a
16:07:37.98	−22:42:47.1	19.291 ± 0.013	17.875 ± 0.008	16.781 ± 0.007	16.091 ± 0.020	15.403 ± 0.012	M8.75,L0	LM12,L08a,XSH
16:08:18.42	−22:32:25.2	18.555 ± 0.008	17.157 ± 0.005	16.086 ± 0.004	15.387 ± 0.011	14.699 ± 0.007	M9.25,L0	LM12,L08a,XSH
16:08:28.47	−23:15:10.5	17.724 ± 0.006	16.424 ± 0.004	15.423 ± 0.003	14.795 ± 0.007	14.137 ± 0.004	M9,L1	LM12,L08a,XSH
16:08:47.44	−22:35:48.1	17.870 ± 0.006	16.639 ± 0.004	15.722 ± 0.003	15.080 ± 0.009	14.526 ± 0.006	M8,M9	LM12,L08a
16:10:47.13	−22:39:49.6	17.483 ± 0.005	16.205 ± 0.003	15.236 ± 0.003	14.631 ± 0.006	14.027 ± 0.004	M8.5,M9	L11a,L08a,XSH
16:14:41.68	−23:51:06.0	18.589 ± 0.012	17.157 ± 0.006	16.078 ± 0.004	15.357 ± 0.010	14.643 ± 0.006	M9.25,L1	LM12,L08a
16:15:16.66	−23:40:46.5	17.989 ± 0.008	16.674 ± 0.004	15.631 ± 0.003	14.935 ± 0.006	14.288 ± 0.004	M9	L08a

Table 4. Logs of the VLT X-shooter spectroscopic observations. We provide the coordinates (J2000) of the targets with the ID used in figures, their *J*-band magnitudes, the date of observations and the exposure times for the NIR arm. The exposure times chosen for the NIR arm are used for the UVB and VIS arms to optimize overheads.

ID	Name VISTA J	*J* mag	Date yyyy-mm-dd	ExpT sec
5	16114437−2215446	17.861 ± 0.016	2015-04-11	10×300
10	16140756−2211522	18.251 ± 0.022	2015-04-11	12×300
12	16020000−2057341	18.320 ± 0.032	2015-04-11	12×300
11	16053909−2403328	18.320 ± 0.032	2015-04-11	12×300
2	16130231−2124285	17.175 ± 0.011	2015-04-12	4×300
14	16013692−2212027	19.270 ± 0.066	2015-04-12	12×300
9	16041304−2241034	18.167 ± 0.025	2015-04-12	10×300
13	16042042−2134530	18.413 ± 0.029	2015-04-12	12×300
7	16091868−2229239	17.940 ± 0.017	2015-04-12	10×300
1	15593638−2214159	16.970 ± 0.009	2015-04-12	4×300
15	16151270−2229492	19.339 ± 0.057	2015-04-13	12×300
8	16073161−2146544	18.040 ± 0.022	2015-04-13	10×300
4	16051705−2130449	17.788 ± 0.017	2015-04-13	10×300
6	16095636−2222457	17.867 ± 0.016	2015-04-13	10×300
3	16142256−2331178	17.456 ± 0.012	2015-04-13	6×300

non-linear pixels. Next, a master bias and master dark are created for the optical and near-infrared data, respectively. Afterwards, a first-guess order and arc line tables created by illuminating the X-shooter pinhole mask with a continuum and arc lamp are produced. Later, a master flat and an order table tracing the flat edges before establishing the 2D map of the instrument are constructed. Subsequently, the efficiency of the whole system, composed of the telescope, instrument and detector, is determined. Finally, 2D spectra for the targets, telluric standards and flux standards are generated. We used the final 2D spectra produced by `esoreflex` rather than the final 1D spectra, because of the faintness of our targets. We should also emphasize that the pipeline does not correct for telluric bands. Moreover, the ESO staff have informed us about a problem with the sky illumination of the last order of X-shooter, which leads to a jump in the spectra at ∼2.27 μm, where the last and the next to last order are joined. This issue affects solely the determination of the CO spectral index (Section 5.3) by making it larger; because of this artefact, we do not use the CO spectral index (Burgasser et al. 2002) in our analysis. We also note the presence of a possible artefact around 2.1 μm in some of our targets, which affects indices including the *K*-band region of the spectra (CH4-K, KH, H2O-D2, H2O-2, sH2OK).

We carried out the next steps under the IRAF environment. First, we extracted a 1D spectrum for our targets and their associated telluric standard stars with the IRAF routine `apsum`. To correct for telluric bands and lines, we fitted the 1D spectrum of the telluric stars taken each night within `splot` and normalized the continuum to one. We removed the strongest Paschen and Bracket lines in the spectrum of the telluric late-B star in the resulting spectrum. Finally, we divided the spectra of our targets by this spectrum of the telluric standard and multiplied by a blackbody with the effective temperature of the telluric standard. The final NIR spectra of the UpSco member candidates are displayed in Fig. 3. We compare the X-shooter spectra of our candidates with known low- and high-gravity dwarfs in Fig. 4. We present the internal UpSco comparison in Fig. 5, where the spectral change of some key features can be seen from earlier to later spectral types. We use this figure to establish a relative spectral sequence of our data in Section 5.2.

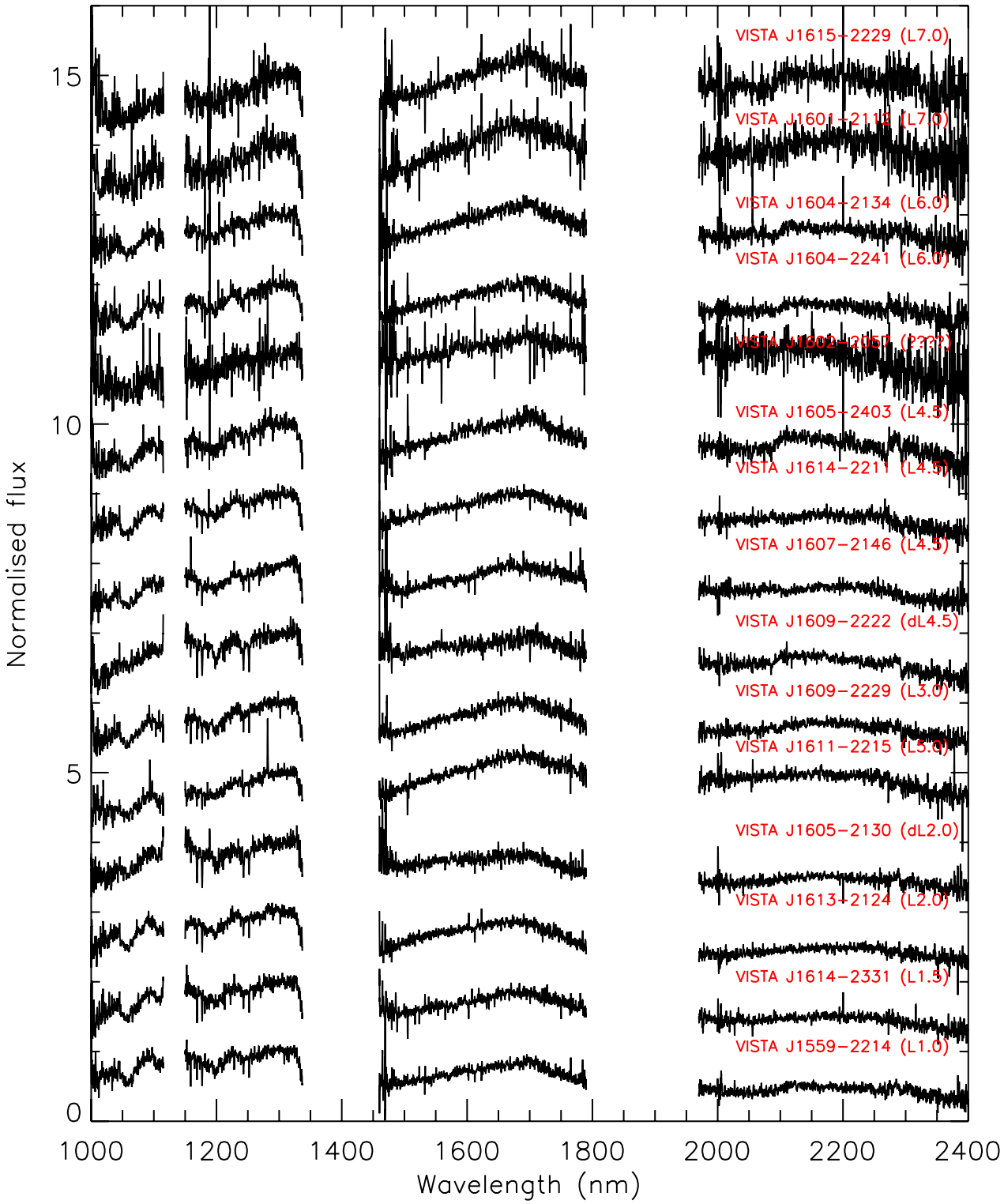

Figure 3. VLT X-shooter spectra of 15 UpSco member candidates (this work). We note that 1611−2215 might be of earlier type with an infrared excess (L2.0 exc). All spectra are normalized at 1.30–1.32 μm.

3.1.3 Known UpSco members with X-shooter spectra

We cross-matched our list of VISTA candidates with the literature and found that several candidates have been previously confirmed as members of the UpSco association in the literature. A few of them (6) have also been observed with VLT/Xshooter by other groups. We list these objects with their infrared magnitudes and spectral types in Table 3.

We reduced the six X-shooter spectra downloaded from the ESO archive with the same version of the pipeline. We extracted the 1D spectra from the 2D images created by the pipeline. We corrected those spectra for telluric bands with the `molecfit` package

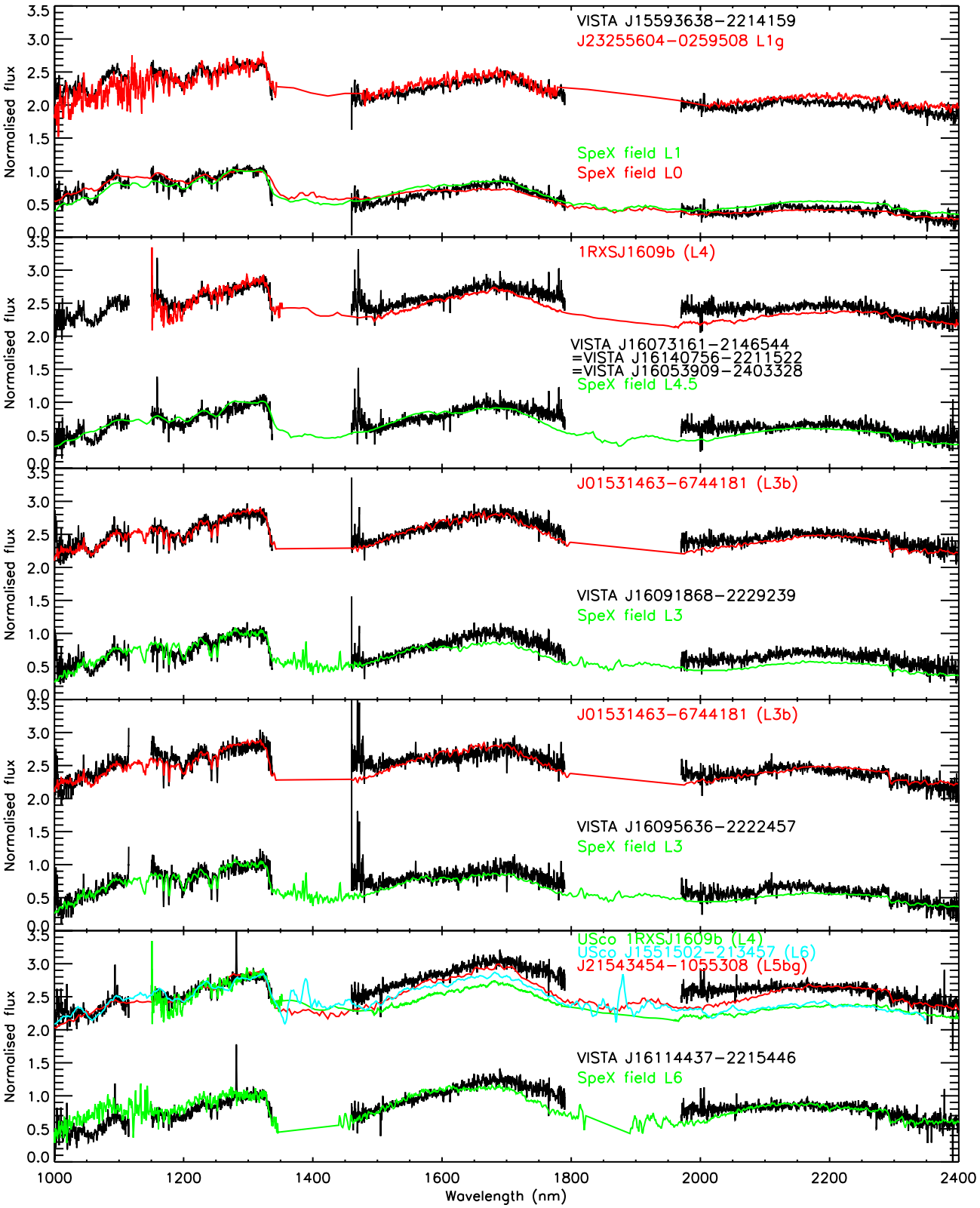

Figure 4. VLT X-shooter spectra of all UpSco member candidates presented in this work, compared with smoothed spectra of field L-dwarf templates of similar spectral types and known young objects. The names of our targets and the templates are given on each plot with their spectral types (b = β, g = γ). We note that 1611−2215 might be of earlier type with an infrared excess (L2.0 exc). All spectra are normalized at 1.30–1.32 μm.

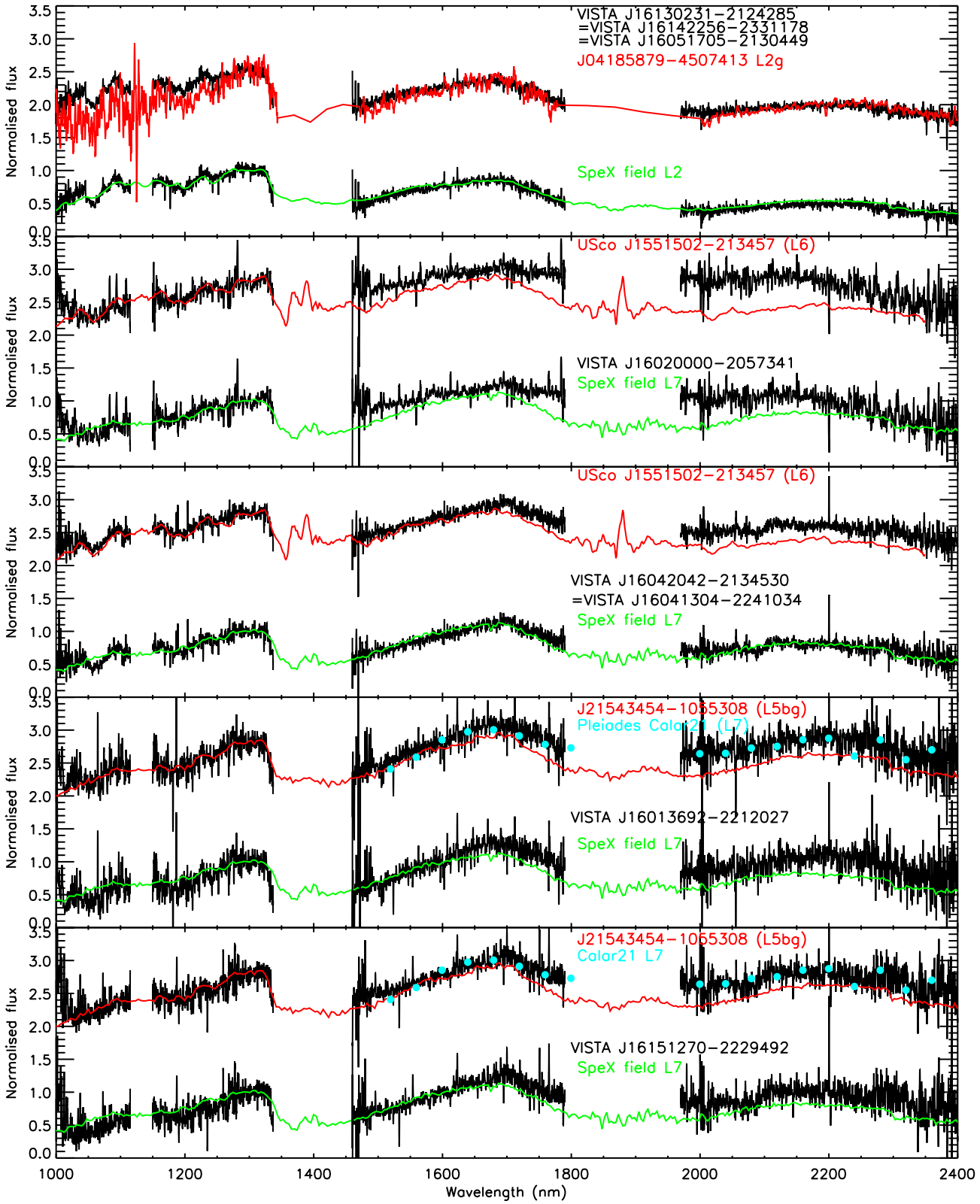

Figure 4 – *continued.*

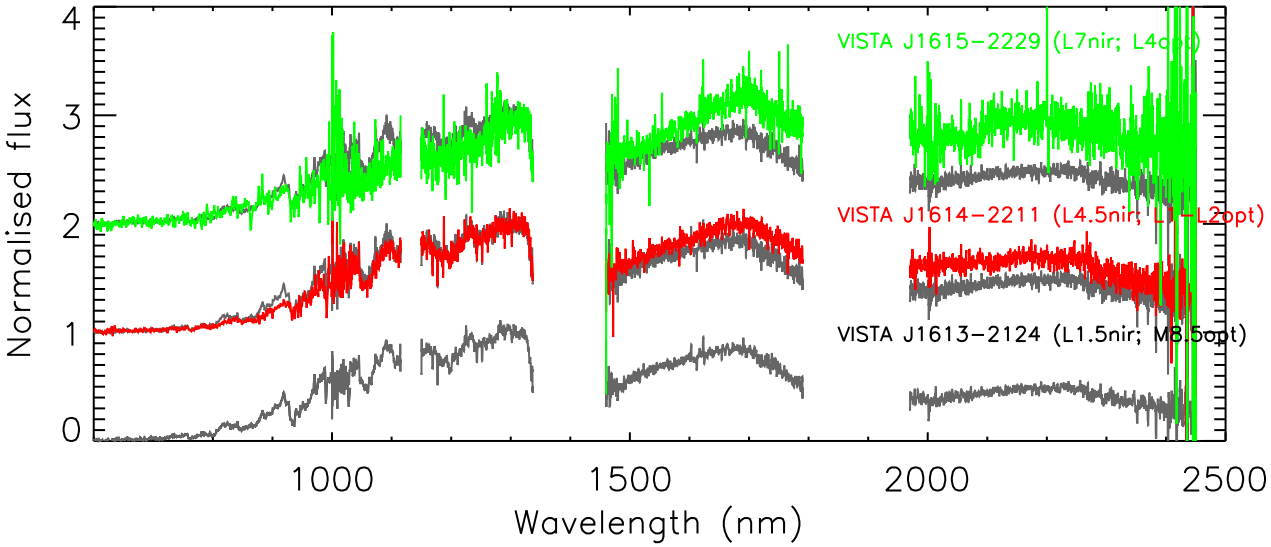

Figure 5. Optical and near-infrared spectra of VISTA J1613−2124 (grey; L1.5nir; M8.5opt), VISTA J1614−2211 (red; L4.5nir; L2opt), and VISTA J1615−2229 (green; L7nir; L4opt) showing evolution as a function of spectral type among our UpSco sequence. All spectra are normalized at 1.30–1.32 μm.

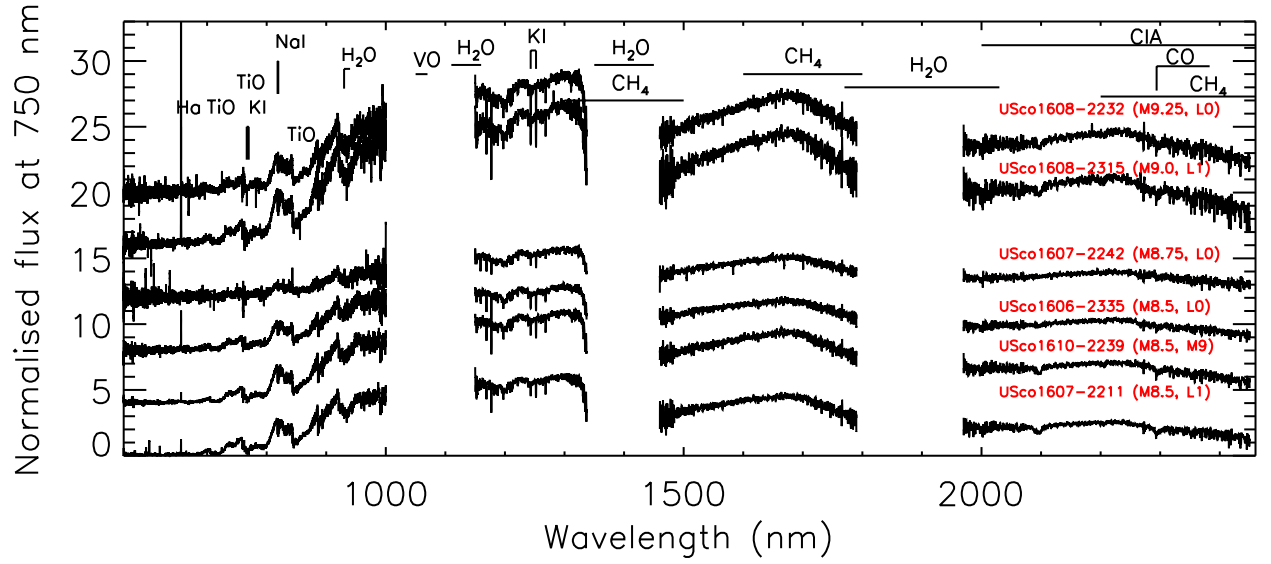

Figure 6. VLT X-shooter spectra of known UpSco members in the ESO archive with their optical (first value) and near-infrared (second value) spectral classification. All spectra are corrected for telluric bands. From bottom to top: VISTA J16072381−2211021 (M8.5, L1), USco16104713−2239496 (M8.5,M9), USco16060629−2335135 (M8.5,L0), USco16073798−2242471 (M8.75,L0), USco16082847−2315105 (M9.0,L1), USco16081842−2232252 (M9.25,L0).

distributed by ESO (Kausch et al. 2015; Smette et al. 2015),[2] mainly because no specific telluric standard was taken at the same time and airmass as these targets. The 0.55–2.4 μm optical-to-infrared spectra of these six M8.5–M9.25 UpSco members are displayed in Fig. 6. They represent benchmark 5–10 Myr old objects for future discoveries of young brown dwarfs in moving groups, due to the high quality of their spectra and the intermediate spectral resolution.

3.2 GTC OSIRIS optical spectroscopy

We collected low-resolution optical spectra with GTC OSIRIS for all 15 UpSco targets with X-shooter near-infrared spectra (Table 5).

[2] http://www.eso.org/sci/software/pipelines/skytools/molecfit

We carried out the observations in two-visitor mode run over six half-nights between 2016 June 7 and 13 (programme GTC25-16A; PI Lodieu) and five half-nights on 2017 May 25–29 (programme GTC40-17A; PI Lodieu). In 2016, the nights were dark to grey, with the moon increasing from 20 per cent illumination up to 57 per cent between 2016 June 7 and 12. The seeing was typically sub-arcsec during the first three nights, except during the first 1 h on the night of June 9. The night of June 10 was lost, due to technical problems and high humidity. The night of June 11 was affected by strong wind altering the seeing (measured between 1.5 and 2.0 arcsec). The last night was affected by bad seeing (>2.5 arcsec). We collected a spectrum for VISTA J16140756−2211522 on 2016 July 2 in service mode under dark time, clear conditions and seeing around 0.8 arcsec. In 2017 May, the nights were also dark and the skies clear every night. The seeing was sub-arcsec during the first four

Table 5. Journal of observations for GTC OSIRIS optical spectroscopy (Section 5.2): the top part lists UpSco candidates with X-shooter spectra, whereas the bottom part lists backup targets from Lodieu et al. (2008), with their near-infrared spectral types in brackets. The photometry comes from our VISTA deep survey (top panel) and UKIDSS Galactic Clusters Survey (bottom panel; MKO system).

Name	Z mag	Date yyyy-mm-dd	ExpT sec	Hα
15593638−2214159 (L1.0)	19.523	2016-06-07	2 × 1200	
16130231−2124285 (L1.5)	19.955	2016-06-11	4 × 1500	
16140756−2211522 (L4.5)	21.027	2016-07-02	4 × 1800	
16042042−2134530 (L6.0)	21.138	2016-06-07	4 × 1200	
16013692−2212027 (L7.0)	22.250	2016-06-08	5 × 2300	
16151270−2229492 (L7.0)	22.402	2016-06-09	6 × 2300	Yes
16142256−2331178 (L2.0)	20.236	2017-05-25	4 × 1200	
16051705−2130449 (L2.0)	20.356	2017-05-25	4 × 1200	
16091868−2229239 (L3.0)	20.777	2017-05-28	4 × 1800	
16073161−2146544 (L4.5)	20.760	2017-05-26	4 × 1500	Yes
16114437−2215446 (L5.0)	20.946	2017-05-27	4 × 1800	Yes
16053909−2403328 (L4.5)	21.103	2017-05-27	4 × 1800	
16020000−2057341 (????)	21.372	2017-05-28	4 × 1800	Yes
16041304−2241034 (L6.0)	20.652	2017-05-26	4 × 1500	
16042042−2134530 (L6.0)	21.138	2017-05-29	3 × 1200	
15472282−2139143 (L0)	19.94	2016-06-12	1 × 1200	Yes
16060629−2335133 (L0)	18.43	2016-06-12	1 × 1200	
16072782−2239040 (L1)	19.36	2016-06-12	1 × 1200	
16073799−2242470 (L0)	19.24	2016-06-12	1 × 1800	
16082847−2315104 (L1)	17.64	2016-06-12	1 × 1200	Yes
16083049−2335110 (M9)	16.95	2016-06-12	1 × 900	Yes
16122895−2159361 (L1)	–	2016-06-12	1 × 1800	
16144168−2351059 (L1)	18.40	2016-06-12	1 × 1800	

nights and variable between 1.1 and 1.5 arcsec on the last night (May 29).

We obtained low-resolution optical spectra with the R300R grating covering 4800–10 000 Å and a slit of 1 arcsec, resulting in a spectral resolution below 300. We acquired our targets in the Sloan z-band filter, due to their faintness at optical wavelengths. We used on-source integrations between 20 and 40 min for the brightest and faintest targets, shifted along the slit several times by a few arcsec (between 5 and 12 arcsec) to avoid nearby stars in constant AB patterns (a similar technique was used in the near-infrared). We provide the journal of observations in Table 5. We placed a bright ($Y \leq 18$ mag) nearby (<50 arcsec) reference star in the slit to calculate the shifts along the slit with the highest precision possible, implying that our targets were not observed at a parallactic angle. However, prior to three of our targets, we observed the reference star alone at a parallactic angle to evaluate the loss of light. We concluded that the effect of the angle was negligible redwards of 6500 Å. Hence, our targets remain unaffected because very little or no flux is seen at these blue wavelengths.

Because of the poor seeing on June 12, we obtained optical spectra of a few bright late-M and L dwarf members of Upper Sco classified in the near-infrared based on Gemini spectra (Lodieu et al. 2008). The targets are listed in the bottom part of Table 5. We opted for this backup programme because of the earlier spectral types reported by Herczeg et al. (2009) for two L dwarfs (VISTA J160723.82−221102.0 and VISTA J160603.75−221930.0) published in Lodieu et al. (2008). We plot these objects in Fig. 9 and discuss the discrepancy between optical and near-infrared classifications in Section 5.4.

We reduced the optical spectra under the IRAF environment (Tody 1986, 1993) in a standard manner. First, we median-combined the bias and flat-fields taken during the afternoon used only for spectrophotometric standard stars and reference stars. We calibrated the 1D spectra with the response function derived from two spectrophotometric standard stars: Ross 640 classified as DZA5.5 (Greenstein & Trimble 1967; Harrington & Dahn 1980; Wesemael et al. 1993; Cutri et al. 2003; Monet et al. 2003; Lépine & Shara 2005) and the sdB1 Feige 66 (Reed 2003; Gontcharov 2006; van Leeuwen 2007). We also corrected for second-order contamination by observing the standard star with the R300R grating and the R300R+SDSSz filter. We calibrated our spectra in wavelength with HgAr+Xe+Ne lamps taken during the afternoon with a dispersion of ∼7.9 Å and rms better than 0.5 Å. For the reference stars, we subtracted the mean bias from the raw spectrum of the target and divided by the normalized flat-field. We extracted the one-dimensional spectrum by choosing the aperture and the background level optimally. For the targets, we produce images subtracting the 'B' position from the 'A' position to improve the sky subtraction in the red optical part, where most of the flux of our targets is concentrated. Then, we extracted the 1D spectra optimally and averaged them to produce the final spectra displayed in Fig. 7, separating the objects observed in 2016 June (left panel) and 2017 May (right panel). We display the two strong Hα emitters in Fig. 8. We normalized the final OSIRIS optical spectra at 8250 Å and compared them with field late-M and early-L dwarfs.

3.3 GTC EMIR infrared spectroscopy

We also used the Multi-object Infrared Spectrograph (EMIR: Garzón & EMIR Team 2016) mounted on the Naysmith-A focus of the GTC to obtain the near-infrared spectrum of USco J155150.2−213457. We collected these data as part of an EMIR science verification project. This object was first identified by Peña Ramírez et al. (2016) using photometric, astrometric and spectroscopic techniques and was classified as a low-gravity L6 ± 1 dwarf based on the presence of strong VO absorption at 1.06 μm, the triangular shape of the H-band pseudo-continuum and the red nature of its spectrum. EMIR is equipped with a 2048 × 2048 pixel Teledyne HAWAII-2 HgCdTe detector with a pixel scale of 0.2 arcsec on the sky. We acquired the EMIR data of USco J155150.2−213457 with the YJ spectroscopic filter, a 0.8-arcsec long slit and the YJ grism as the dispersive optical element. This instrumental configuration yields low-resolution spectra (R ∼ 740) covering the wavelength interval 0.92–1.33 μm. We obtained a total of 32 individual spectra of 120 s each (total on-source integration time 3840 s) following a nodding ABBA pattern with offsets of ∼10 arcsec. The observing conditions were photometric and the seeing was 1.2 arcsec on the night of 2017 April 8. We also observed the field L6 dwarf 2MASS J10101480−0406499 (Cruz et al. 2003; Jameson et al. 2008) with the same instrumental configuration and an exposure time of 4 × 360 s. We used this field L6 dwarf as a spectral standard indicative of high-gravity features. We reduced the EMIR raw spectra in the same manner as the X-shooter data. We performed wavelength calibration using observations of an HgAr lamp and we corrected the instrumental response with observations of a hot B3V-type star. We removed the telluric contribution from the target data using the same hot star, since it was observed at related airmasses.

Fig. 10 shows the EMIR spectra. Although the optical-to-near-infrared rising slope of both USco J155150.2−213457 and the L6 standard are very similar at these wavelengths, some individual

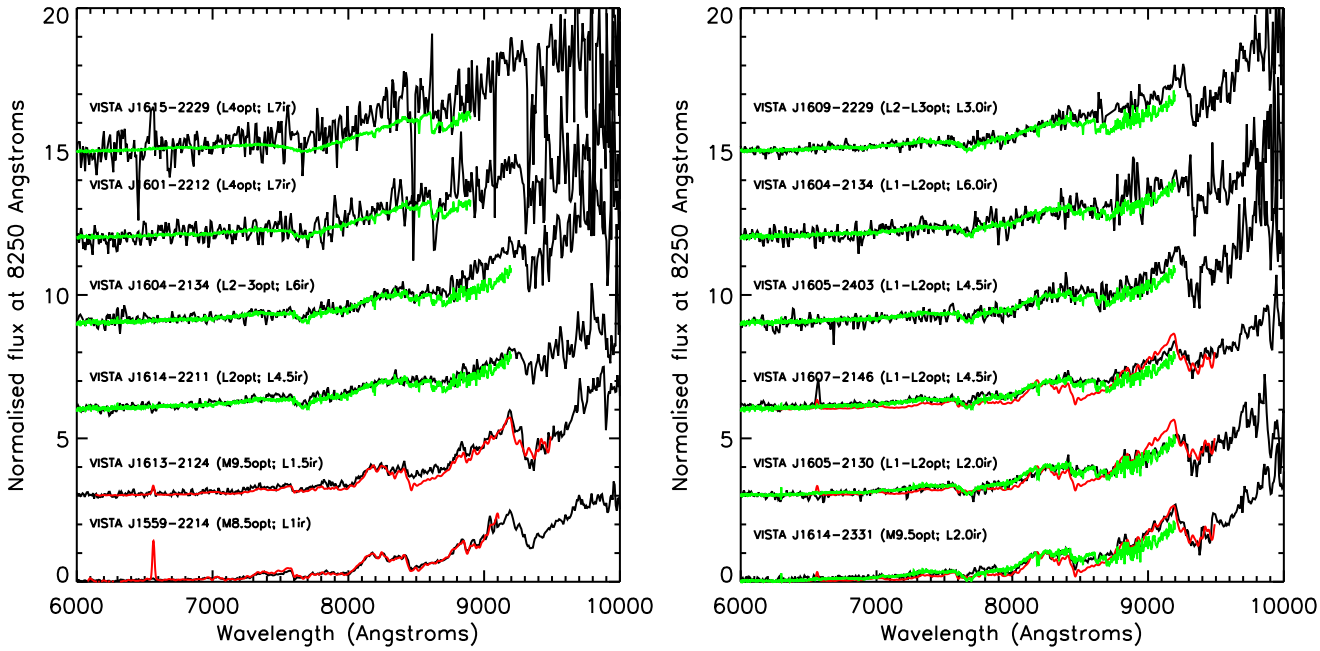

Figure 7. GTC/OSIRIS low-resolution optical spectra of UpSco member candidates taken in 2016 June (left) and 2017 May (right). The spectral types derived in this work from the VLT/X-shooter near-infrared spectra and GTC/OSIRIS optical spectra are quoted next to the names. Overplotted in red are young spectral template members of the Taurus star-forming region (KPNO 06 (M8.5) and KPNO 4 (M9.5): Briceño et al. 1998; Luhman et al. 2003a) and in green are Sloan L-type spectral templates marked next to the name of the targets (Schmidt et al. 2010). Spectra are shifted for clarity.

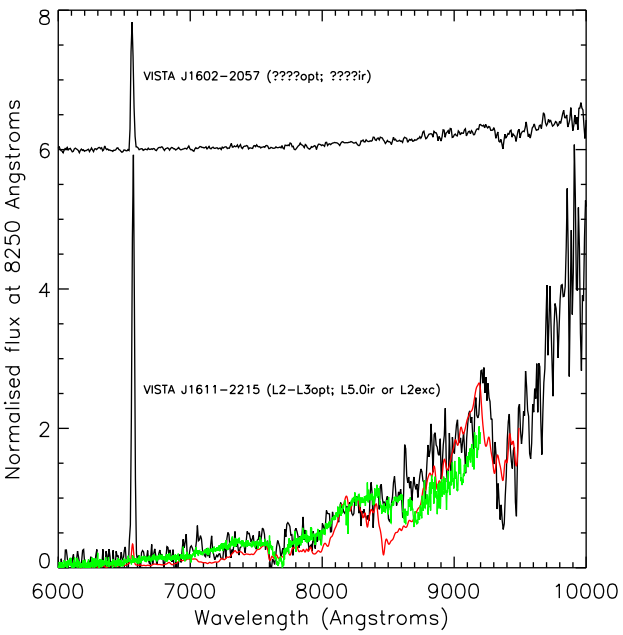

Figure 8. GTC/OSIRIS low-resolution optical spectra (black) of the two sources with strong Hα emission lines: VISTA J1602−2057 (top) and VISTA J1611−2215 (bottom). The coordinates and spectral types derived from the VLT/X-shooter near-infrared spectra and optical spectra (Section 5.2.4) are quoted next to the names. We note that VISTA J1602−2057 is most likely a non-planetary-mass member of the association, because its optical spectrum is not as red as those of the other targets and its infrared spectrum does not exhibit strong water bands. Overplotted in red and green respectively are a member of Taurus classified as M9.5 (KPNO 4: Briceño et al. 1998; Luhman et al. 2003a) and a Sloan L2 dwarf template (Schmidt et al. 2010). Spectra are shifted for clarity.

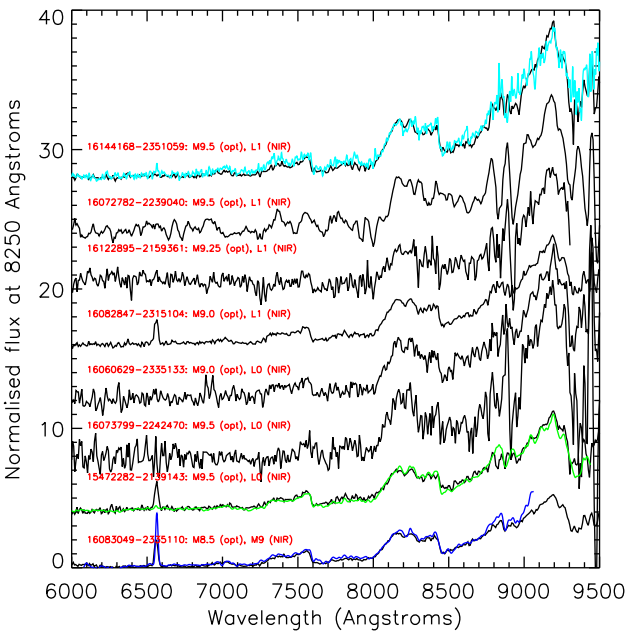

Figure 9. GTC/OSIRIS low-resolution optical spectra of eight M9–L1 UpSco brown dwarf members with near-infrared spectral types from Lodieu et al. (2008). Overplotted in colour are three young spectral templates, members of Taurus (KPNO06; M8.5; blue: Briceño et al. 1998; Luhman et al. 2003a), Chamaeleon (11122250−7714512; M9; green: Luhman 2004; Luhman et al. 2007) and USco (UScoCTIO 108B; M9.5; cyan: Béjar et al. 2008). Spectra are shifted for clarity. More details are given in Section 5.2.4.

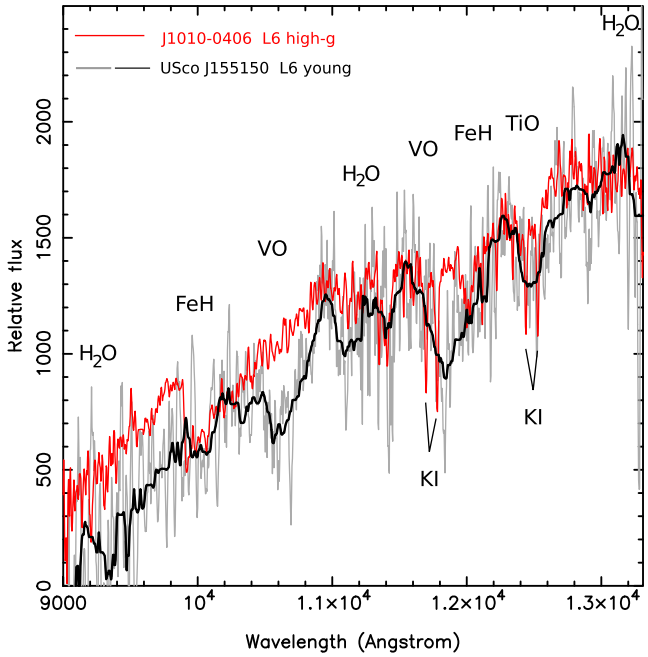

Figure 10. GTC EMIR spectra of 2MASS J10101480−0406499 (red) and USco J155150.2−213457 (the grey line depicts the original spectrum, while the thick black line illustrates the median-filtered data). The objects are classified as L6 high- and low-gravity dwarfs, respectively. The size of the median filter is 41 pixels. The spectrum of the field dwarf was normalized to the observed flux of the UpSco object at 1.28–1.32 μm.

features are clearly different. The molecular absorption at ∼1.06 μm (VO), ∼1.18 μm (VO) and ∼1.25 μm (TiO) appears significantly stronger in the UpSco object, while the absorption at ∼0.99 μm (FeH) is weaker in relative terms, probably because of the low-gravity atmosphere of the UpSco source (see also the discussion in McGovern et al. 2004; Martin et al. 2017).

4 ALLWISE MID-INFRARED PHOTOMETRY

We cross-matched the list of 15 candidates with X-shooter spectra with the AllWISE catalogue (Wright et al. 2010) using a matching radius of 5 arcsec. Most targets were found within 0.3 arcsec of the position extracted from our VISTA catalogue. We found that 11 of them have reliable WISE *w*1 and *w*2 photometry (flags of A and B) with signal-to-noise ratios larger than six and a minimum of 19 flux measurements in each band (Table 6). The remaining four sources (abbreviated names are VISTA J1602−2057, VISTA J1605−2403, VISTA J1609−2222 and VISTA J1614−2331) are detected in the images at 3.6 and 4.5 μm, but have no entry in the AllWISE catalogue, mainly because they are either very faint (two cases) or close to another brighter star (three cases, one common to the very faint case).

To define a clean infrared sequence of the lowest mass members in UpSco, we also cross-correlated the list of 67 VISTA *ZYJ* candidates (table 2 of L13) with AllWISE. This query retrieved 51 sources with no deblending and reliable *w*1 and *w*2 photometry. We show the resulting near-infrared versus mid-infrared colour–magnitude diagrams for these two samples in Fig. 11. We overplotted the sequence of field M/L/T dwarfs derived from the polynomial fits given in table 14 of Dupuy & Liu (2012), shifted to the distance of UpSco. The field sequence lies well below the UpSco sequence, because of the difference in age between the association (∼5–10 Myr:

Table 6. *Top panel:* AllWISE photometry (MKO system) with errors for 11 of the 15 UpSco candidates with VLT/X-shooter (Table 4). Numbers in brackets listed after the photometry depict the signal-to-noise ratio (SNR). The other targets do not have entries in the AllWISE catalogue, but are detected on the 3.6- and 4.5-μm images. *Bottom panel:* WISE photometry for M9–L1 dwarfs in Lodieu et al. (2008) observed with GTC/OSIRIS. Only VISTA J16083049−2335110 is detected in *w*3 (11.621+/-0.266 mag), with a signal-to-noise ratio of 4.1.

Name	*w*1 mag (SNR)	*w*2 mag (SNR)
15593638−2214159	15.214 ± 0.045 (24)	14.784 ± 0.071 (15)
16130231−2124285	15.495 ± 0.055 (19)	14.993 ± 0.083 (13)
16142256−2331178	− ± − (−)	− ± − (−)
16051705−2130449	15.958 ± 0.060 (18)	15.925 ± 0.172(6)
16114437−2215446	15.303 ± 0.045 (24)	14.726 ± 0.070 (15)
16095636−2222457	− ± − (−)	− ± − (−)
16091868−2229239	15.539 ± 0.051 (21)	15.317 ± 0.114(9)
16073161−2146544	15.147 ± 0.040 (27)	14.596 ± 0.062 (17)
16041304−2241034	15.462 ± 0.049 (22)	15.254 ± 0.105 (10)
16140756−2211522	15.570 ± 0.051 (21)	15.290 ± 0.105 (10)
16053909−2403328	− ± − (−)	− ± − (−)
16020000−2057341	− ± − (−)	− ± − (−)
16042042−2134530	15.695 ± 0.051 (21)	15.332 ± 0.110(9)
16013692−2212027	16.300 ± 0.076 (14)	15.520 ± 0.139(7)
16151270−2229492	16.529 ± 0.100 (10)	15.729 ± 0.156(6)
15472280−2139143	13.690 ± 0.072 (15.0)	13.029 ± 0.033 (33.3)
16060629−2335133	14.534 ± 0.030 (35.8)	13.987 ± 0.042 (26.0)
16072782−2239040	15.015 ± 0.038 (28.3)	14.455 ± 0.066 (16.4)
16073799−2242470	15.098 ± 0.039 (27.7)	14.743 ± 0.075 (14.4)
16082847−2315104	13.765 ± 0.027 (40.2)	13.179 ± 0.030 (36.3)
16083049−2335110	13.360 ± 0.026 (41.4)	12.841 ± 0.029 (37.8)
16122895−2159361	14.197 ± 0.029 (37.2)	13.639 ± 0.039 (28.2)
16144168−2351059	14.300 ± 0.029 (37.4)	13.881 ± 0.041 (26.8)

Preibisch et al. 2001; Pecaut et al. 2012; Song et al. 2012) and field dwarfs (typically 1 Gyr or older). We also added to this diagram the WISE photometry for the eight M9–L1 UpSco members with near-infrared photometry from Lodieu et al. (2008) listed in Table 6. In Fig. 12, we plot the ($J - K$, $J - w1$) colour–colour diagram with the same symbology.

5 CHARACTERIZATION OF YOUNG L-TYPE MEMBERS OF UPSCO

As illustrated in Figs 2, 3, 5 and 6, we have optical and near-infrared photometry and spectroscopy of a significant number of high-probability member candidates of UpSco (∼5–10 Myr, $d \sim 145$ pc, solar metallicity) that span almost 2.5 mag in the J band (from 17.0–19.3 mag). We discuss the morphological changes observed in the spectra in subsequent sections. Because our targets likely share the same age and metallicity and are located at the same distance (the intracluster distances have a negligible impact in the following discussion), we attribute these changes to a sequence of spectral types and different effective temperatures ($T_{\rm eff}$), although additional effects, like the presence of dusty clouds or veiling due to strong accretion, may also imprint complex spectral signatures. Our goal is to establish a proper classification of these coeval objects, thus complementing the efforts made by other groups regarding the analysis of spectra of members of intermediate-age (>10 Myr) stellar moving groups (e.g. Allers & Liu 2013; Filippazzo et al. 2015; Gagné et al. 2015; Faherty et al. 2016; Liu, Dupuy & Allers 2016).

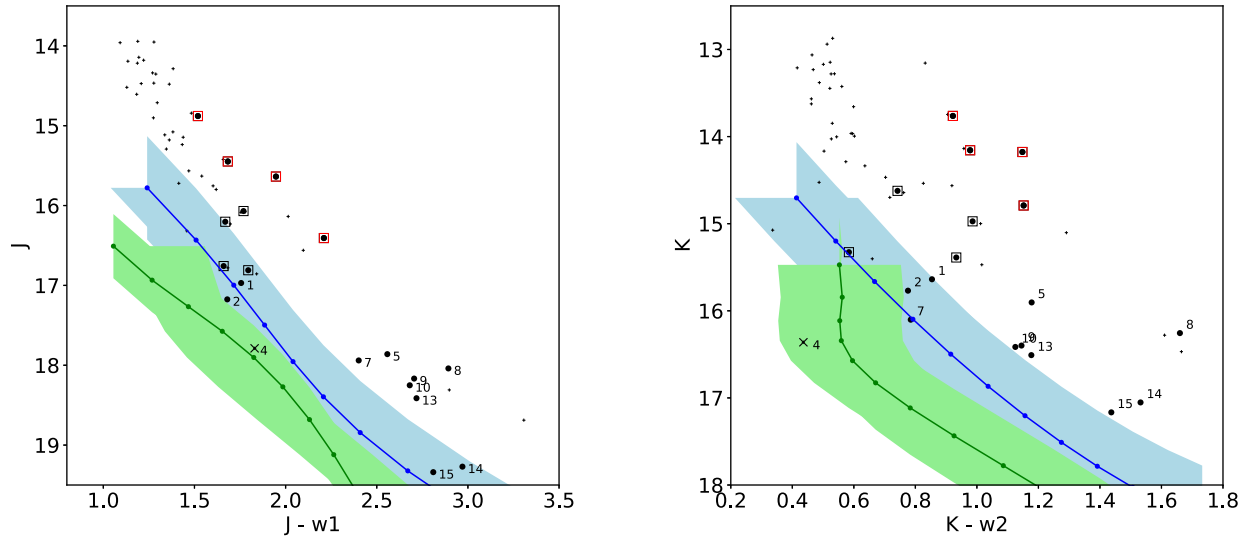

Figure 11. *Left:* $(J - w1, J)$ colour–magnitude diagram for all VISTA *ZYJ* candidates identified in L13 with WISE photometry (grey crosses). Overplotted as black dots with their ID numbers are the UpSco candidates with X-shooter spectra (Table 6) and the M9–L1 from Lodieu et al. (2008) with GTC optical spectra as dots surrounded by squares (those with red squares show mid-infrared excess). We added the sequence of young and field M7–L8 dwarfs from Faherty et al. (2016) with their dispersion in blue and green, respectively.

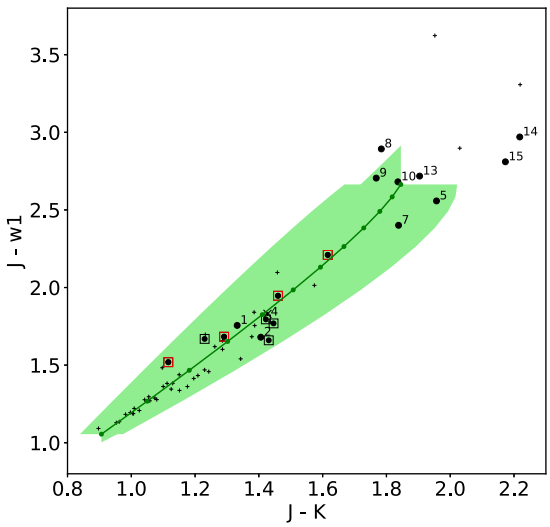

Figure 12. $(J - K, J - w1)$ colour–colour diagram for all VISTA *ZYJ* candidates identified in L13 with WISE photometry (grey crosses). Overplotted as black dots with their ID numbers are the UpSco candidates with X-shooter spectra (Table 6) and the M9–L1 from Lodieu et al. (2008) with GTC optical spectra as dots surrounded by squares (those with red squares show mid-infrared excess). We added the sequence of field M7–L8 dwarfs from Faherty et al. (2016) with its dispersion in green.

5.1 Photometric properties

We assessed the membership of our VISTA candidates further with the SDSS*i* imaging obtained with the GTC. Using the $(i - J, J)$ colour–magnitude diagram of Fig. 2, we already removed two likely contaminants from the sample of UpSco VISTA candidates (see Section 2). The remaining sources, including *i*-band non-detections, follow a sequence redder than field stars along the line of sight of UpSco.

We also check the mid-infrared photometry of our candidates. We find that UpSco members define a sequence with a high level of dispersion in the near-infrared versus mid-infrared diagrams presented in Fig. 11, from $J = 14$ mag down to $J = 19.5$ mag (equivalent to $K \sim 13$–17.5 mag). Late-M dwarfs show a trend towards brighter magnitudes with lower ages. However, studies in young moving groups suggest that younger L dwarfs have similar magnitudes to older field L dwarfs in the near-infrared (*JHK* bands), with a tendancy to be brighter in the WISE passbands (Gagné et al. 2015; Faherty et al. 2016; Liu et al. 2016). We overplotted the sequence of field L dwarfs with its dispersion in the near-infrared to mid-infrared diagrams to gauge the redness of our UpSco member candidates. We observe that UpSco members lie above the field sequence shifted to the distance of the association. The candidates presented in this article overlap and extend the sequence of M9–L1 dwarfs confirmed spectroscopically in the near-infrared with Gemini/GNIRS (dots with open squares in Fig. 11: Lodieu et al. 2008; Herczeg et al. 2009). We note that VISTA J16083049−2335110 (M8.5opt, M9ir: Lodieu et al. 2008) is clearly detected in the WISE *w*3 band with a magnitude of 11.621 ± 0.266, advocating that this object most likely harbours a disc (Table 6). This source lies on top of the UpSco sequence in both near-infrared to mid-infrared colour–magnitude diagrams (Fig. 11), particularly in the $(K - w2, K)$ diagram (black dots with open red squares). Three other sources appear above the sequence in the $K - w2$ colours (VISTA J16082847−2315104, VISTA J15472280−2139143 and VISTA J16060629−2335133), which might suggest the presence of either a disc or a close-in companion, although additional effects cannot be discarded at these ages (e.g. photometric errors, extinction; Table 6). The other possible explanation lies in the role of the accretion history of low-mass stars and brown dwarfs during the early stages of their formation (Baraffe et al. 2017). In contrast, one of the 15 candidates with X-shooter spectra, USco 16051705−2130449, lies below the sequence, even below the sequence of field stars shifted to the distance of UpSco, suggesting that it might not be true member of UpSco but rather older. One of the 15 targets might exhibit considerable flux excesses in the *w*2 passband: VISTA J1607−2146

(#8). This object is discussed further in Section 5.2.4, where we report the detection of Hα emission in its GTC/OSIRIS optical spectrum.

Overall, the positions of 14 out of 15 of our candidates in several colour–colour magnitude diagrams over a wide wavelength range add credit to their membership of the UpSco association.

5.2 Spectral classification

5.2.1 Word of caution

First, we note that several authors have reported discrepancies between the optical and near-infrared spectral classifications of young late-M and L dwarfs. This trend was mentioned first by Martín et al. (2001a) and corroborated by the optical spectra of faint σ Ori members (Barrado y Navascués et al. 2001). Later, Luhman et al. (2003b) found a systematic offset between optical and *K*-band (2.0–2.4 μm) spectral types of young late-M dwarf members of IC 348, the latter being consistently 1–2 subclasses later. This effect had already been pointed out for members of the ρ Oph region (Luhman & Rieke 1999) and confirmed in Taurus (Luhman et al. 2017) and in other moving groups and associations (Pecaut 2016). Lucas et al. (2001) mentioned this effect independently, comparing observed optical and *H*-band spectra with the physical parameters derived from the synthetic models of Allard et al. (2001). Allers & Liu (2013) also emphasize the fact that their qualitative classification of young L dwarfs shows an offset of ∼1 subclass between infrared and optical spectral types.

In UpSco, Béjar et al. (2008) classified UScoCTIO 108B as an M9.5 dwarf from its low-resolution optical (0.55–0.95 μm) spectrum, by comparison with Ophiuchus members and old field stars. However, they quote a spectral type of L3 from their *J*-band spectrum (1.15–1.3 μm) by comparison with field L dwarfs. This discrepancy is comparable with the inconsistency between the infrared and optical spectral types of VISTA J160723.82−221102.0 (L1 versus M8.5) and VISTA J160603.75−221930.0 (L2 versus M8.75) reported by Lodieu et al. (2008) and Herczeg et al. (2009), respectively.

In this article, we will classify our targets independently in the optical and near-infrared for those followed up in both wavelength regions. We stress the importance of stellar clusters in defining reliable photometric and spectroscopic sequences of members that have distinct masses (therefore varying luminosities and magnitudes) but the same age, distance and metallicity. The increasing numbers of bright, young L dwarf member candidates (typically <L5) of stellar moving groups during the past years (e.g. Gagné et al. 2014, 2015; Malo et al. 2014; Faherty et al. 2016; Liu et al. 2016) contrasts with the limited numbers of late-M and early-L type members of young clusters and star-forming regions with good-quality optical and near-infrared spectra (Barrado y Navascués et al. 2001; Martín & Zapatero Osorio 2003; Allers et al. 2007; Lodieu et al. 2008; Herczeg et al. 2009; Cruz et al. 2009; Bayo et al. 2011), some of them used for comparison in this work. With this article, we will alleviate this lack of data and will provide a sequence of young L-type spectra with ages of 5–10 Myr and solar metallicity.

5.2.2 Relative near-infrared classification

First, we compare the set of X-shooter spectra of our targets (Section 3.1; Figs 3 and 5) against each other to reveal similarities and differences and define a relative classification where later objects have steep pseudo-continuum slopes, the strongest water bands and less intense VO. We use abbreviated names below.

(i) VISTA J1559−2214 is the earliest target of all, with $J = 16.970 \pm 0.009$ mag and $J - K = 1.33 \pm 0.02$ mag.

(ii) VISTA J1613−2124 ($J = 17.18 \pm 0.01$, $J - K = 1.41 \pm 0.02$) is similar to VISTA J1559−2214 in the *J* band, while the blue part of the *H* band appears in between the fluxes of VISTA J1559−2214 and VISTA J1611−2215. The *K*-band region is similar to VISTA J1605−2130 ($J = 17.79 \pm 0.02$, $J - K = 1.43 \pm 0.03$). Overall, we classify this source as intermediate between the earliest source and VISTA J1605−2130.

(iii) VISTA J1605−2130 is relatively brighter than VISTA J1559−2214 in *J* and *K*. The blue part of the *H* band exhibits more flux, while the red part of the *H* band is identical.

(iv) VISTA J1614−2331 ($J = 17.46 \pm 0.01$, $J - K = 1.44 \pm 0.02$) is identical to VISTA J1605−2130, so we assign one subtype later than the earliest source to both objects.

(v) VISTA J1611−2215 ($J = 17.86 \pm 0.02$, $J - K = 1.96 \pm 0.03$) is similar to VISTA J1613−2124 in *J*, but relatively much brighter in *H* and *K*.

(vi) VISTA J1609−2222 ($J = 17.87 \pm 0.02$, $J - K = 1.68 \pm 0.03$) shows almost no absorption in the VO band at 1.06 μm, displays a stronger CO absorption band at 2.3 μm and has a flatter *H* band than any other source in our sample, suggesting that it is a field L4.5 dwarf rejected as a member of the association.

(vii) VISTA J1609−2229 ($J = 17.94 \pm 0.02$, $J - K = 1.84 \pm 0.03$) is similar to VISTA J1613−2124 in *J* but twice as bright as VISTA J1613−2124 and fainter than VISTA J1611−2215 in *H* and *K*. Its overall SED is intermediate between VISTA J1613−2124 and VISTA J1609−2222 and exhibits features of youth, such as VO absorption at 1.06 μm and the peaked *H* band.

(viii) VISTA J1602−2057 ($J = 18.50 \pm 0.03$, $J - K = 2.12 \pm 0.04$) is difficult to classify: it shows a much more straight *J*-band spectrum with weak VO absorption than other objects in our sample. It also has a flat *H* band with weak water bands and a more depressed red part of the *K* band. However, it is almost as bright as VISTA J1611−2215 in *H* and *K*. Nonetheless, we cast doubts on its membership.

(ix) VISTA J1607−2146 ($J = 18.04 \pm 0.02$, $J - K = 1.78 \pm 0.03$) is identical to VISTA J1614−2211 ($J = 18.25 \pm 0.02$, $J - K = 1.84 \pm 0.04$) and VISTA J1605−2403 ($J = 18.32 \pm 0.03$, $J - K = 1.94 \pm 0.04$). They are similar to VISTA J1609−2229 in *J*, but appear slightly brighter in *H* and have similar flux level in *K*. We note that VISTA J1607−2146 shows an excess at 1.27–1.32 μm and is the reddest in our sample at these wavelengths. We also note that VISTA J1605−2403 displays extra flux in the 2.08–2.015 μm region, which might be due to a problem with merging of X-shooter orders.

(x) VISTA J1604−2241 ($J = 18.17 \pm 0.03$, $J - K = 1.77 \pm 0.04$) and VISTA J1604−2134 ($J = 18.41 \pm 0.03$, $J - K = 1.90 \pm 0.04$) are identical. They are similar to VISTA J1607−2146, with a shallower VO absorption band at 1.06 μm, similar flux in *H* and slightly more flux in *K*. They are relatively brighter than VISTA J1611−2215 in *H* and *K*, hence later than both VISTA J1607−2146 and VISTA J1611−2215.

(xi) VISTA J1615−2229 ($J = 19.34 \pm 0.06$, $J - K = 2.17 \pm 0.08$) and VISTA J1601−2212 ($J = 19.27 \pm 0.07$, $J - K = 2.22 \pm 0.08$) are very similar. They are the reddest objects in our sample and show the strongest water absorption bands. The VO absorption at 1.06 μm is weaker than for earlier sources, but the disappearance of this feature might be the result of lower temperature, because both

of them show clear features characteristic of youth (peaked *H* band, weak gravity-sensitive doublets).

5.2.3 Tentative absolute near-infrared classification

In this section, we attempt to define a tentative spectral classification by comparison with the known sequence of field L dwarfs using templates downloaded from the SpeX archive.[3]

We also compared our spectra with the two known mid-L dwarfs reported as photometric and spectroscopic members in USco: 1RXS J1609291−210524 ($L4^{+1}_{-2}$: Lafrenière, Jayawardhana & van Kerkwijk 2008, 2010) and USco J1551502−213457 (L6 ± 1: Peña Ramírez et al. 2016), as well as a sample of young L dwarfs for which spectra are available from J. Gagné's webpage (Gagné et al. 2015)[4] and in the Pleiades (Zapatero Osorio et al. 2014). We should point out that 1RXS J1609291−210524 might harbour a disc (Wu et al. 2015), so we should be cautious using it as a spectral template. We detail our comparisons below, going from the brightest to the faintest sources. The results are given in Table 7 and shown in Fig. 4.

(i) VISTA J1559−2214 is the earliest member in our sample. Its overall shape is best reproduced by an early-L dwarf; the *J*-band is best fitted by an L1, while the $H + K$ resemble a L0. We assign a near-infrared spectral type of L1.0 ± 0.5 to this source (Fig. 4), consistent with the overall SED of 2MASS J23255604−0259508 (L1γ; Gagné et al. 2015).

(ii) The spectra of VISTA J1613−2124 and VISTA J1614−2331 look similar and are well reproduced by the SpeX spectrum of Kelu 1 (L2opt; L3ir_pec: Ruiz, Leggett & Allard 1997; Kirkpatrick et al. 1999; Stumpf et al. 2008). Therefore, we classify VISTA J1613−2124 as L1.5 and VISTA J1614−2331 as an L2 member of UpSco with an uncertainty of half a subclass.

(iii) The spectrum of VISTA J1605−2130 looks similar to the SpeX spectrum of Kelu 1. The absorption at 1.06 μm is almost absent and the *H*-band spectrum is not as peaky as for the other candidates, casting doubt on its spectroscopic membership. We classify this object as a L2 dwarf.

(iv) VISTA J1611−2215 is best fitted by the SpeX spectrum of a field L6 dwarf (Fig. 4), although the water bands in *H* and *K* suggest a slightly earlier spectral type. It is brighter in *H* and *K* than 1RXS J1609291−210524 ($L4^{+1}_{-2}$; Lafrenière et al. 2008, 2010) and shows an excess in the colour–magnitude diagrams using WISE passbands (Section 4; Fig. 11), so we assign it a spectral type of L5 throughout the article, but keep in mind that its spectral type is most likely L2exc ± 1 with an infrared excess.

(v) VISTA J1609−2222 is well fitted by a field L4.5 dwarf from the SpeX archive. As described earlier, its spectrum does not show features of youth, a fact corroborated by comparison with a young L3γ (Gagné et al. 2015). Hence, we discard this source as a member of UpSco and assign it a spectral type of dL3.0 ± 0.5.

(vi) The spectrum of VISTA J1609−2229 is perfectly fitted by the spectrum of 2MASS J01531463−6744181 (L3γ: Reid et al. 2008; Gagné et al. 2015). The object shows clear features of youth, such as the VO absorption at 1.06 μm and the peaked *H* band, so we classify it as a L3.0 ± 0.5 member of UpSco.

(vii) VISTA J1607−2146, VISTA J1614−2211 and VISTA J1605−2403 show SEDs similar to the SpeX L4.5 template and comparable with the near-infrared spectrum of

[3] http://pono.ucsd.edu/~adam/browndwarfs/spexprism/index_old.html
[4] http://www.astro.umontreal.ca/~gagne/MSL.php

Table 7. Coordinates (J2000) of VISTA candidates, for which we derive near-infrared spectral types (SpT_{NIR}), measured pseudo-equivalent widths (in nm) of the Na I line at 1.138 μm and two potassium doublets in the *J* band (Fig. 14) and radial velocities from the positions of the potassium doublets and via the cross-correlation technique (RV_CC). To infer the true radial velocity from the lines, we should subtract −9.05 ± 4.83 km s^{-1}, which is the radial velocity of the reference star VISTA J1559−2214. We note that VISTA J1611−2215 might be of earlier type, with an infrared excess (L2.0exc).

ID	Name VISTA J	*J* mag	SpT_{NIR}	EW_{NaI} nm	λ_{KI} EW_{KI} (nm, nm) (nm, nm)	λ_{KI} EW_{KI} (nm, nm) (nm, nm)	RV_index km s^{-1}	RV_CC km s^{-1}
1	15593638−2214159	16.970	L1.0 ± 0.5	0.37	(1243.11,1252.10) (0.18,0.23)	(1168.90,1177.05) (0.25,0.35)	−9.11 ± 4.83	Reference
2	16130231−2124285	17.175	L1.5 ± 0.5	0.33	(1243.05,1252.03) (0.21,0.23)	(1168.93,1177.12) (0.27,0.48)	−8.9 ± 14.5	−3.7 ± 1.3
3	16142256−2331178	17.456	L2.0 ± 0.5	0.41	(1243.12,1252.12) (0.16,0.22)	(1169.02,1177.13) (0.44,0.43)	−10.4 ± 38.8	14.5 ± 1.3
4	16051705−2130449	17.788	dL2.0 ± 0.5	0.36	(1243.17,1252.09) (0.27,0.26)	(1168.90,1177.17) (0.67,0.79)	−0.2 ± 17.7	17.2 ± 2.6
5	16114437−2215446	17.861	L5.0 ± 1.0	0.43	(1243.03,1252.06) (0.14,0.16)	(1168.76,1177.05) (0.19,0.32)	−23.9 ± 15.9	0.6 ± 11.6
6	16095636−2222457	17.867	dL3 ± 0.5	0.35	(1243.15,1252.10) (0.67,0.66)	(1169.02,1177.16) (0.68,0.66)	9.4 ± 19.1	13.7 ± 6.7
7	16091868−2229239	17.940	L3.0 ± 0.5	0.25	(1243.11,1252.08) (0.25,0.27)	(1168.94,1177.13) (0.30,0.36)	−1.2 ± 9.2	6.8 ± 7.0
8	16073161−2146544	18.040	L4.5 ± 0.5	0.24	(1243.11,1252.02) (0.16,0.21)	(1168.88,1176.92) (0.30,0.37)	−8.1 ± 9.4	2.4 ± 6.1
9	16041304−2241034	18.167	L6.0 ± 1.0	0.31	(1243.10,1252.17) (0.21,0.26)	(1168.89,1177.06) (0.14,0.40)	−4.1 ± 24.1	9.0 ± 7.8
10	16140756−2211522	18.251	L4.5 ± 0.5	0.38	(1243.05,1252.05) (0.14,0.20)	(1168.95,1177.00) (0.21,0.37)	−4.5 ± 15.1	1.4 ± 5.8
11	16053909−2403328	18.320	L4.5 ± 0.5	0.43	(1243.14,1252.08) (0.13,0.28)	(1169.03,1177.23) (0.27,0.41)	6.6 ± 24.5	3.8 ± 7.9
12	16020000−2057341	18.500	????	0.50	(1242.97,1252.24) (0.32,0.37)	(1169.02,1176.88) (0.26,0.48)	−10.9 ± 63.1	1.5 ± 7.5
13	16042042−2134530	18.413	L6.0 ± 1.0	0.26	(1243.06,1252.12) (0.19,0.21)	(1168.88,1177.19) (0.22,0.34)	−1.9 ± 9.6	5.5 ± 6.9
14	16013692−2212027	19.270	L7.0 ± 1.0	0.15	(1243.12,1252.13) (0.13,0.20)	(1168.89,1177.00) (0.33,0.35)	2.3 ± 7.2	13.4 ± 10.4
15	16151270−2229492	19.339	L7.0 ± 1.0	–	(1243.07,1252.10) (0.15,0.30)	(1168.75,1177.13) (0.40,0.40)	−5.9 ± 7.5	18.3 ± 13.1

1RXS J1609291−210524. Hence, we classify them as L4.5 ± 0.5 members of UpSco. We note that VISTA J1607−2146 exhibits a possible excess in $w2$, as discussed in Section 5.1.

(viii) VISTA J1602−2057 is difficult to classify and we could not assign it a spectral type, because none of the field or young L dwarf templates display a good fit. We do not detect strong water bands in its infrared spectrum. We leave its classification open at this stage.

(ix) VISTA J1604−2134 and VISTA J1604−2241 are well fitted by the spectrum of USco J1551502−213457 (L6 ± 1: Peña Ramírez et al. 2016). They are redder than VISTA J1611−2215, which we classify as L5 and earlier than the two coolest sources (see next bullet). Their infrared spectra compare well with the SpeX L7 template, except for a stronger VO absorption and peaked H-band feature. Therefore, we classify them as L6 ± 1 members of UpSco.

(x) VISTA J1601−2212 and VISTA J1615−2229 are the coolest members and appear later than any other of our targets. In the classification of field L dwarfs, the reddest sources in H and K have spectral types of L7 and L7.5. Moreover, the 1.5–2.4 μm region is very similar to the SED of Calar 21 (L7 ± 1: Zapatero Osorio et al. 2014). Both of them are fairly well fitted by a field L7 spectrum, except for a stronger VO absorption, a peaked H-band feature and more flux in K. Therefore, we assign to them the latest spectral type, L7 ± 1.

Overall, this absolute spectral classification agrees well with the relative classification described in the previous section. The spectral sequence progresses from L1–L2 for the brightest VISTA candidates to mid-L for the group of sources around $J \sim 18$ mag to late-L for the two faintest objects with $J \sim 19.3$ mag. We define the first sequence for young L dwarf members of the UpSco association with an age of ∼5–10 Myr that should serve as a 'benchmark' for comparison with other young systems discussed in the literature or to be discovered in the near future.

5.2.4 *Optical spectral classification*

We proceed, in a similar manner to the near-infrared classification, to assign optical spectral types to the targets with GTC/OSIRIS low-resolution spectra (Section 3.2). In Fig. 7, we plot the optical spectra of all sources classified as L dwarfs in the near-infrared and observed in 2016 June (left panel) and 2017 May (right panel).

From Figs 7 and 8, we see Hα in emission in four L-type objects: VISTA J1615−2229, VISTA J1607−2146, VISTA J1602−2057 and VISTA J1611−2215 (Table 5). The line strength is moderate in VISTA J1615−2229 and this object does not show evidence of mid-infrared flux excesses up to 4.5 μm. Therefore, the origin of the Hα emission could be chromospheric. Chromospheric emission is expected in young M and L dwarfs (see review by Luhman 2012). VISTA J1607−2146 also has moderate Hα emission and significant mid-infrared flux excess at 4.5 μm (see object #8 in Figs 11 and 12), which implies the presence of a warm disc and possible accretion. VISTA J1602−2057 and VISTA J1611−2215, however, show considerably strong Hα emission, although it is not resolved at the resolution of our data. Both objects could be accreting material and their optical spectra may be affected by some veiling (Fig. 8), thus contributing to unreliable determinations of spectral type at optical wavelengths. This scenario is reinforced by the presence of possible mid-infrared flux excesses in VISTA J1611−2215 (object #5 in Fig. 13), which suggests the existence of a disc from which the central source is still accreting even at the age of UpSco (5–10 Myr). As discussed in the review by Luhman (2012), it seems that discs manage to survive at ages of ∼10 Myr around very low-mass sources; see also Luhman & Mamajek (2012). VISTA J1607−2146 and VISTA J1611−2215, the masses of which are likely below 15$M_{\rm Jup}$, prove that both discs and accretion phenomena can persist up to ∼10 Myr, unless these sources are much younger than the cluster (which is possible only for VISTA J1611−2215, given the fact that it is brighter than all other related objects at all magnitudes). VISTA J1607−2146 and VISTA J1611−2215 should be added to the limited number of planetary-mass objects harbouring discs, e.g. SOri 60 (Zapatero Osorio et al. 2007; Luhman et al. 2008) or 2MASS J04414489+2301513 (Adame et al. 2011).

In Fig. 7 we overplotted in green the Sloan optical spectra of old field L dwarfs that best match the spectra of targets, to assign tentative spectral types. We classify our targets into several groups, best fitted by L1–L2, L2–L3 and L4 in the optical by direct comparison with Sloan spectra. We classify the two faintest targets in our sample as L4opt ± 1 (compared with L7ir). Consequently, we find a trend towards earlier spectral types in the optical than in the near-infrared, marked by the presence of TiO and VO at optical wavelengths for sources classified as early-L dwarfs in the near-infrared. We find an optical sequence going from late-M dwarfs to early- and mid-L dwarfs that matches the photometric and near-infrared spectral sequences in UpSco, where the brightest sources exhibit earlier spectral types. We overplotted in red two known young members of Taurus, KPNO6 (M8.5) and KPNO 4 (M9.5) (Briceño et al. 1998; Luhman et al. 2003a), which reproduce the optical spectra of the late-M UpSco members well, thus reinforcing our classification scheme and the young nature of these UpSco candidates.

Puzzled by this systematic trend, we increased the sample of optical spectra of UpSco members classified as M9–L1 in the near-infrared (Gemini/GNIRS spectra in table 1 and fig. 1 of Lodieu et al. 2008). We plot these optical spectra in Fig. 9, where the earliest object is at the bottom, and quote both optical and near-infrared spectral types next to their names. We compare them with the two young sources discussed above and UScoCTIO 108B to assign optical spectral types between M8.5 and M9.5. We observe a smaller spectral type interval at optical than at infrared wavelengths (M8.5–M9.5 versus M9–L1), which most likely reflects the fact that oxides remain stronger at low gravities, due to low pressures, although VO and TiO have been severely depleted in field early-L dwarfs. We clearly detect Hα in emission in three of these UpSco members (Table 5).

5.2.5 *Adopted spectral classification*

We have decided to assign both optical and near-infrared spectral types to our targets. Nonetheless, we have adopted the near-infrared spectral types, based on three arguments.

(i) A significant fraction of the flux of late-M and L dwarfs is emitted at near-infrared wavelengths. The optical flux up to 1.0 μm barely represents <10 per cent of the total flux. Both optical and near-infrared wavelengths have spectral features that depend on temperature, gravity and metallicity. Fig. 16 shows the comparison of the combined optical and near-infrared spectral energy distributions (SEDs) of UpSco dwarfs against SEDs of spectral types based on the optical and near-infrared classifications. The overall SED of UpSco dwarfs is better matched by the SEDs corresponding to the near-infrared classification.

(ii) The TiO and VO bands, which are the basis of the optical spectral scheme, depend strongly on gravity, as we can see from the

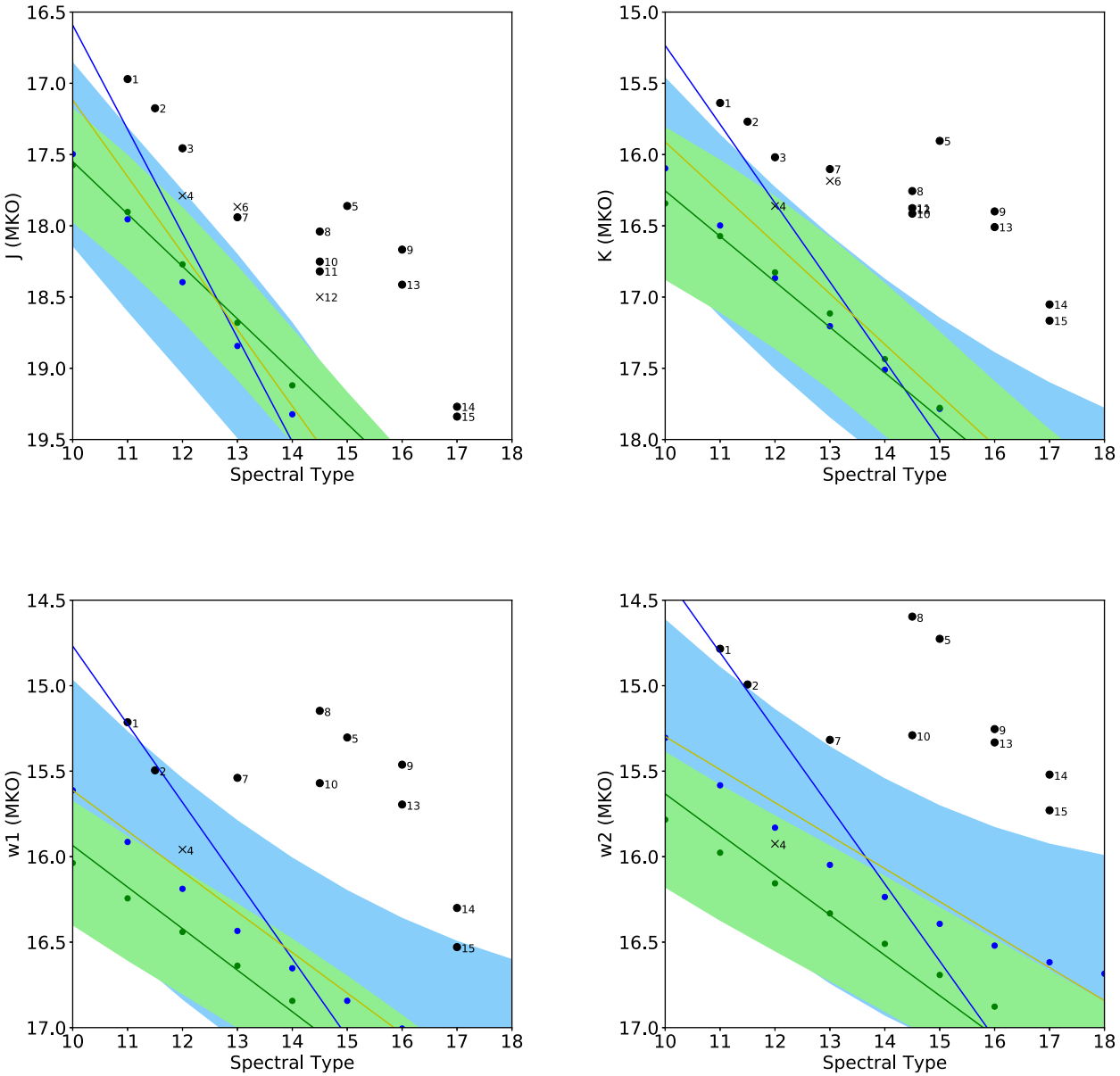

Figure 13. Observed *J*, *K*, *w*1, *w*2 magnitudes versus NIR spectral type for all UpSco candidates with X-shooter spectra (black dots). Our targets are labelled with numbers following the order listed in Table 6. Photometric error bars are plotted, but are usually smaller than the symbol size for *J* and *K* magnitudes. We overplotted the polynomials of the sequences of young and field L dwarfs from Faherty et al. (2016) with blue and green dots, with their dispersion (light blue and light green). We also added the polynomial fits for the field, INT-G and VLG samples of Liu et al. (2016) in green, yellow and blue, respectively. The axis represents spectral type, where 10≡L0, 12≡L2, etc....

presence of VO at 1.06 μm (Fig. 16). Nonetheless, the optical-to-infrared slope of the spectra is best reproduced by the slope of the near-infrared spectral types.

(iii) The UpSco spectral sequence spans ∼2.4 mag in *J* (17.0–19.3 mag), which would correspond to field L dwarfs with spectral types in the L0–L6 range, in agreement with our near-infrared spectral range but larger than our optical spectral range.

We do not share the opinion of constructing a spectral classification for young L dwarfs based on optical spectral types ignoring the differences between visible and infrared spectra, as described in Luhman et al. (2017). This is a valid proposal for field L dwarfs, but we argue that the low gravity affecting the sodium and potassium doublets in the infrared should have an even stronger effect on the optical spectral energy distribution of young L dwarfs than on the infrared, since the optical region is mainly shaped by alkalis. The redness of some L dwarf members of young moving groups with intermediate ages might originate from the presence of dust and/or clouds in their atmospheres or debris discs (Zakhozhay et al. 2017).

5.2.6 *Photometric versus spectroscopic sequence*

We have shown that our targets define a photometric sequence in colour–magnitude and colour–colour diagrams and span a ∼2.5 mag

Table 8. Summary of the membership of all candidates with near-infrared spectroscopy presented in this article. We give their ID plotted in several figures and names. We then list several criteria in the following columns: (5) photometric sequence, (6) near-infrared spectral types, (7) strength of the VO absorption at 1.06 μm, (8) presence of the peaked *H* band, (9) pseudo-equivalent widths of gravity-sensitive features and (10) radial velocities. 'Y' stands for 'Yes, it is a member', 'N' for 'non-member' and '?' for 'maybe'. We consider an object as a member if it satisfies five or six of the criteria. We note that VISTA J1611−2215 might be of earlier type with an infrared excess (L2.0exc).

ID	Name VISTA J	SpT_{NIR}	SpT_{OPT}	phot	SpT	VO	*H* peak	EW	RV
1	1559−2214	L1.0 ± 0.5	M8.5 ± 0.5	Y	Y	Y	Y	Y	Y
2	1613−2124	L2.0 ± 0.5	M9.0 ± 0.5	Y	Y	Y	Y	Y	Y
3	1614−2331	L1.5 ± 0.5	M9.5 ± 0.5	Y	Y	Y	Y	Y	Y
4	1605−2130	dL2.0 ± 0.5	L1–L2	?	Y	?	N	?	?
5	1611−2215	L5.0 ± 1.0	L2–L3	Y	Y	Y	Y	Y	Y
6	1609−2222	dL4.5 ± 0.5	L3	Y	N	N	N	N	Y
7	1609−2229	L3.0 ± 0.5	L2–L3	Y	Y	Y	Y	Y	Y
8	1607−2146	L4.5 ± 0.5	L2–L3	Y	Y	Y	Y	Y	Y
9	1604−2241	L6.0 ± 1.0	L1–L2	Y	Y	Y	Y	Y	Y
10	1614−2211	L4.5 ± 0.5	L1–L2	Y	Y	Y	Y	Y	Y
11	1605−2403	L4.5 ± 0.5	L2.0 ± 0.5	Y	Y	Y	Y	Y	Y
12	1602−2057	????	????	?	?	N	N	?	Y
13	1604−2134	L6.0 ± 1.0	L1–L2	Y	Y	Y	Y	Y	Y
14	1601−2212	L7.0 ± 1.0	L4.0 ± 1.0	Y	Y	N	Y	Y	Y
15	1615−2229	L7.0 ± 1.0	L4.0 ± 1.0	Y	Y	N	Y	Y	Y

range, from $J \sim 17.0$ mag down to $J = 19.3$ mag. They also define a spectroscopic sequence, from L1 to L7 in the near-infrared and from M8.5 to L4 in the optical. We naturally expect such an agreement if our candidates are members of the same region, although additional parameters can enter into the game, such as binarity and the presence of discs at the age of UpSco (∼5–10 Myr).

In Table 8, we summarize the various criteria used in this work to assign membership to the 15 UpSco candidates with near-infrared spectral types. In Fig. 13, we plot observed magnitudes (*J*, *K*, *w*1, *w*2) as a function of near-infrared spectral type to put together the photometric and spectroscopic sequences. We see that the two objects (VISTA J1609−2222, #6; VISTA J1602−2057, #12) classified as non-members do not stand out in these diagrams. However, VISTA J1605−2130 (#4) lies well below the sequences in all diagrams and its near-infrared spectrum did not show the clear presence of VO absorption and the presence of a peaked *H* band (Section 5.2.3), suggesting that it is a contaminant. Object number 5 (VISTA J1611−2215) tends to lie above the sequence, due to its late type compared with the photometric sequence, but we cannot discard it as an earlier type member with an infrared excess (L2exc versus normal L5) at this stage, because all other features typical of young objects are present.

5.3 Spectral indices

We have compiled a large number of spectral indices defined in the literature to classify M, L and T dwarfs in the field and at low ages by independent teams (Tokunaga & Kobayashi 1999; Reid et al. 2001; Testi et al. 2001; Burgasser et al. 2002, 2006; Geballe et al. 2002; McLean et al. 2003; Slesnick, Hillenbrand & Carpenter 2004; Allers et al. 2007; Allers & Liu 2013). We refer the reader to these articles for the definitions of the indices. We computed these spectral indices for a variety of L dwarfs, including the SDSS sequence spanning optical spectral types between L0 and L8 (Schmidt et al. 2010), L dwarfs downloaded from Sandy Leggett's web page,[5] those in Reid et al. (2001) and young L0–L5 dwarfs classified as β and γ following Cruz et al. (2009), Bonnefoy et al. (2014), Allers & Liu (2013) and Gagné et al. (2015)[6], plus the recent additions of PSO J318.5338−22.8603 (L7pec: Liu et al. 2013) and VHS J125601.92−125723.9 (L7pec: Gauza et al. 2015). We report the values of the spectral indices for all sources in Table A1 and plot them as a function of spectral type in Fig. A1 in Appendix A, in which we plot the infrared spectral types of our UpSco sources and the spectral types published in the literature for comparison samples of old field, beta and gamma L dwarfs. We note that the spectral types come from various sources in the literature, which does not necessarily represent a one-to-one correlation with effective temperature. We distinguish field L dwarfs from their younger counterparts by the colours of the symbols: green for old field dwarfs, blue triangles for β L dwarfs, red pentagons for γ L dwarfs and black dots for our UpSco sample. We plot all the spectral indices, along with second-order polynomial fits, in the figures in Appendix A. We plot a subsample of three indices discussed below in Fig. 15.

We carried out a Kolmogorov–Smirnov statistical test to identify the spectral indices most sensitive to gravity. We compared the distributions of our UpSco objects with those of old field L dwarfs for each index individually. After ordering them, we identified the following indices as most sensitive to age (in this order): H-cont, CH4-H, FeHH, VOz and H20-K. We repeated this procedure comparing the γ L dwarfs and the old field L dwarfs (both samples from the literature) and identified four of the indices aforementioned among the five best (H-cont, CH4-H, VOz and H20-K). We inspected these indices visually and indeed observed a strong dependence on gravity for those indices. We conclude that H-cont, VOz, CH4-H, H2O-K and FeH-H can be used primarily to show the youth of members of moving groups (e.g. Gagné et al. 2014, 2015; Malo et al. 2014; Faherty et al. 2016). In contrast, we identified some spectral

[5] http://staff.gemini.edu/~sleggett/LTdata.html

[6] https://docs.google.com/spreadsheets/d/1136rRdcjHZJoe00mt4kPeWU8ZNORcPe-w4cipkDKGRc/

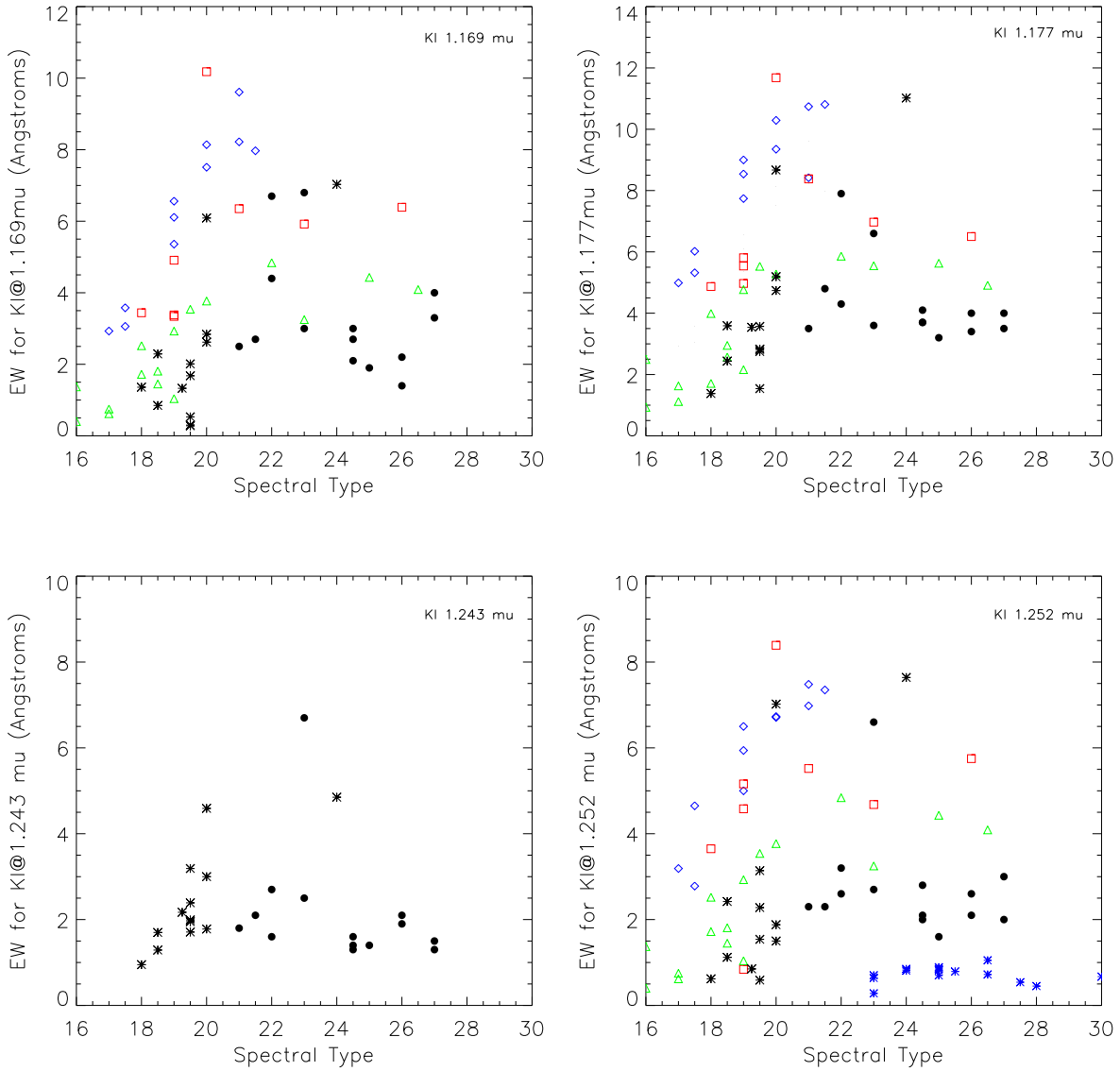

Figure 14. Pseudo-equivalent widths of four gravity-sensitive lines/doublets as a function of NIR spectral type (20≡L0, 25≡L5, etc...) for our USco targets (filled dots), compared with field dwarfs (blue diamonds), low-gravity dwarfs (red squares), very low-gravity sources (green triangles: Allers & Liu 2013) and other young objects from the literature (black asterisks: Bonnefoy et al. 2014; Manjavacas et al. 2014).

indices that appear to be nearly independent of the gravity (age) of L dwarfs, despite the scatter observed in the measurements. The K1 index, which measures the rise of the spectra between 2.0 and 2.14 μm (Tokunaga & Kobayashi 1999), is convenient for spectral classification independent of gravity.

We observe that most of the water-vapour indices defined in the literature are fairly insensitive to gravity, with a few exceptions like H2O-K, and tend to either increase or decrease with later spectral types, demonstrating that the community has used water bands as the main features for L dwarf classification. Moreover, we observe significant differences between our sample and objects in the literature, which we attribute to the lower signal-to-noise ratios in the NIR spectra of our UpSco targets (especially close to the main telluric bands) compared with other studies using high-quality spectra to derive those indices. Summarizing, the H-cont, VOz, CH4-H and FeH-H spectral indices can be used to discriminate on the basis of surface gravity for late-M and L spectral types, while water-based indices are proxies for spectral typing, with the only exception being H2O-K.

5.4 Gravity-sensitive features

Brown-dwarf members of open clusters, star-forming regions and young moving groups are known to exhibit features characteristic of youth, including pseudo-equivalent widths of potassium and sodium doublets weaker than for older field dwarfs, as well as the presence of a peaked *H* band (Martín et al. 1996; Luhman et al. 1998; Béjar, Zapatero Osorio & Rebolo 1999; Lucas & Roche 2000; Zapatero Osorio et al. 2000; Cushing, Tokunaga & Kobayashi 2000; Gorlova et al. 2003; McGovern et al. 2004; Slesnick et al. 2004, 2008; Lodieu et al. 2008; Scholz et al. 2012a; Alves de Oliveira et al. 2012, 2013; Bonnefoy et al. 2014; Manjavacas et al. 2014; Mužić et al. 2014, 2015). In Fig. 14, we plot the pseudo-equivalent widths of the potassium (K I) doublets at

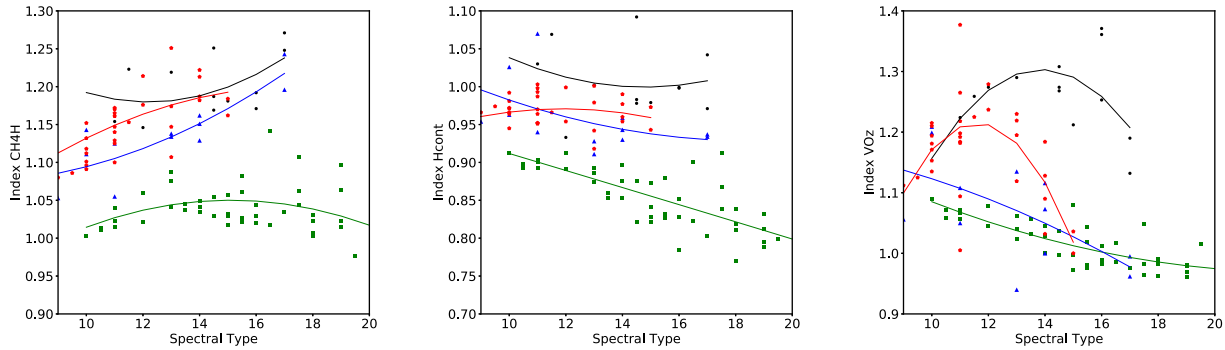

Figure 15. Near-infrared spectral indices defined in the literature versus NIR spectral types for our UpSco candidates (black dots), young β (blue triangles) and γ (red pentagons) L dwarfs (Allers & Liu 2013; Bonnefoy et al. 2014; Gagné et al. 2015) and field L dwarfs with spectral types taken from the literature (green squares: Reid et al. 2001; Geballe et al. 2002; McLean et al. 2003; Knapp et al. 2004; Golimowski et al. 2004; Chiu et al. 2006). The CH4-H, H-cont and VO indices are among the best indices to discriminate between young and old field L dwarfs based on our statistical test.

1.169/1.177 μm and 1.243/1.252 μm as a function of spectral type. We can see clearly that most of our measurements lie below the sequence of field M and L dwarfs (blue symbols) and are consistent with very low gravity dwarfs (green symbols) as defined by Allers & Liu (2013). These objects would correspond to γ L dwarfs on the scale of Cruz et al. (2009). Our sample of UpSco members is comparable in size to the sample of very low gravity sources in Allers & Liu (2013), with the main difference that ours belong to the same region. Only two objects have stronger gravity-sensitive features: VISTA J1609−2222 (#6; dL4.5) shows stronger potassium features consistent with young L dwarfs or field dwarfs and USco 1605−2130 (#4) exhibits stronger absorption at 1.169/1.177 μm but not at 1.243/1.252 μm, suggesting that the doublet with the bluest wavelength might be more gravity-dependent than the other, which is more often used in the literature.

We find that all X-shooter spectra exhibit weaker potassium (1.169/1.177 μm, 1.243/1.252 μm) doublets, except for two objects (VISTA J1605−2130, #4; VISTA J1609−2222, #6). We also find that all but three (VISTA J1605−2130, #4; VISTA J1609−2222, #6; VISTA J1602−2057, #12) show a peaked *H* band, adding strong credit to the membership of the UpSco association of 12 of our VISTA candidates (Fig. 3; Table 7). We also observe a weak sodium doublet at around 0.82 μm in the GTC OSIRIS optical spectra of the two brightest sources, a conclusion confirmed further by direct comparison with spectral templates of similar spectral types from the Taurus and Chamaeleon star-forming regions kindly provided by Kevin Luhman (Fig. 7). Despite the low resolution and poor signal-to-noise ratio of the optical spectra of the other targets, the sodium doublets of the L2–L3 opt dwarfs appear weaker than those of the SDSS template spectra, whereas we cannot draw any definite conclusion for the two faintest sources. We find the same features in the X-shooter spectra of known UpSco members (Luhman & Mamajek 2012) (Fig. 6) and M9–L1 dwarfs from Lodieu et al. (2008) observed with GTC/OSIRIS (Fig. 9). These findings are corroborated by the spectral indices displayed in the bottom panels of Fig. 15.

The other striking feature present in the near-infrared spectrum of young dwarfs is the VO absorption at 1.05–1.08 μm (Cushing, Rayner & Vacca 2005). Allers & Liu (2013) defined a specific index centred on that absorption to assign gravity classes of L0–L4 dwarfs (see Appendix A for comparison with our sources). Indeed, at these spectral types, the lower the gravity, the stronger the depression around 1.06 μm due to condensation effects and hydride opacities. This feature is visible in the spectrum of USco J1551502−213457 (L6 ± 1: Peña Ramírez et al. 2016). Two of the 15 spectra (VISTA J1609−2222, #6 and VISTA J1602−2057, #12) lack this feature (Fig. 3), while a tiny amount of absorption is seen in the spectrum of USco 1605−2130 (#4), which, together with other criteria, casts doubt on their youth and hence membership of the UpSco association. The two faintest sources with the latest spectral types show weaker absorption at 1.06 μm, but the comparison with field L7 dwarfs shown in Fig. 16 demonstrates that VO is still present in ∼5–10 Myr old late-L dwarfs.

In Fig. 16, we show the full spectral energy distribution combining GTC/OSIRIS optical and VLT/X-shooter infrared spectra of our L dwarf members of UpSco. This figure shows the impact of gravity on the full 600–2500 nm region for L dwarfs, in particular the remnants of alkali lines and oxide bands. For this reason, we have decided to assign both optical and near-infrared spectral types to our targets.

5.5 Radial velocities

We computed the radial velocities of our 15 VISTA candidates in two ways. We used, on the one hand, a cross-correlation function using the spectrum with highest signal-to-noise ratio as reference and, on the other hand, the positions of the individual lines of the gravity-sensitive doublets.

We used the `fxcor` task under IRAF to measure the offsets between each candidate and the reference chosen as VISTA J1559−2214, the brightest candidate ($J = 16.97$ mag) with the highest signal-to-noise ratio X-shooter spectrum. We cleaned the spectra for the strongest telluric bands and smoothed them by a factor of seven. We included the keywords necessary to correct the relative Doppler shifts for the Earth's barycentric motion. We considered four regions free of telluric bands for the correlation, located at 1.02–1.10 μm, 1.17–1.33 μm, 1.49–1.77 μm and 2.05–2.36 μm. The relative radial velocities and their associated error bars (between 1.3 and 13.1 km s^{-1}, typically increasing with lower signal-to-noise spectra) are quoted in Table 7. The final radial velocities (Fig. 17) are obtained by subtracting the value of -9.05 ± 4.83 km s^{-1} obtained for VISTA J1559−2214 from the spectral lines (see next paragraph). The true uncertainty on these measurements is set by the slit of 1.2 arcsec used in the NIR arm of X-shooter, giving a

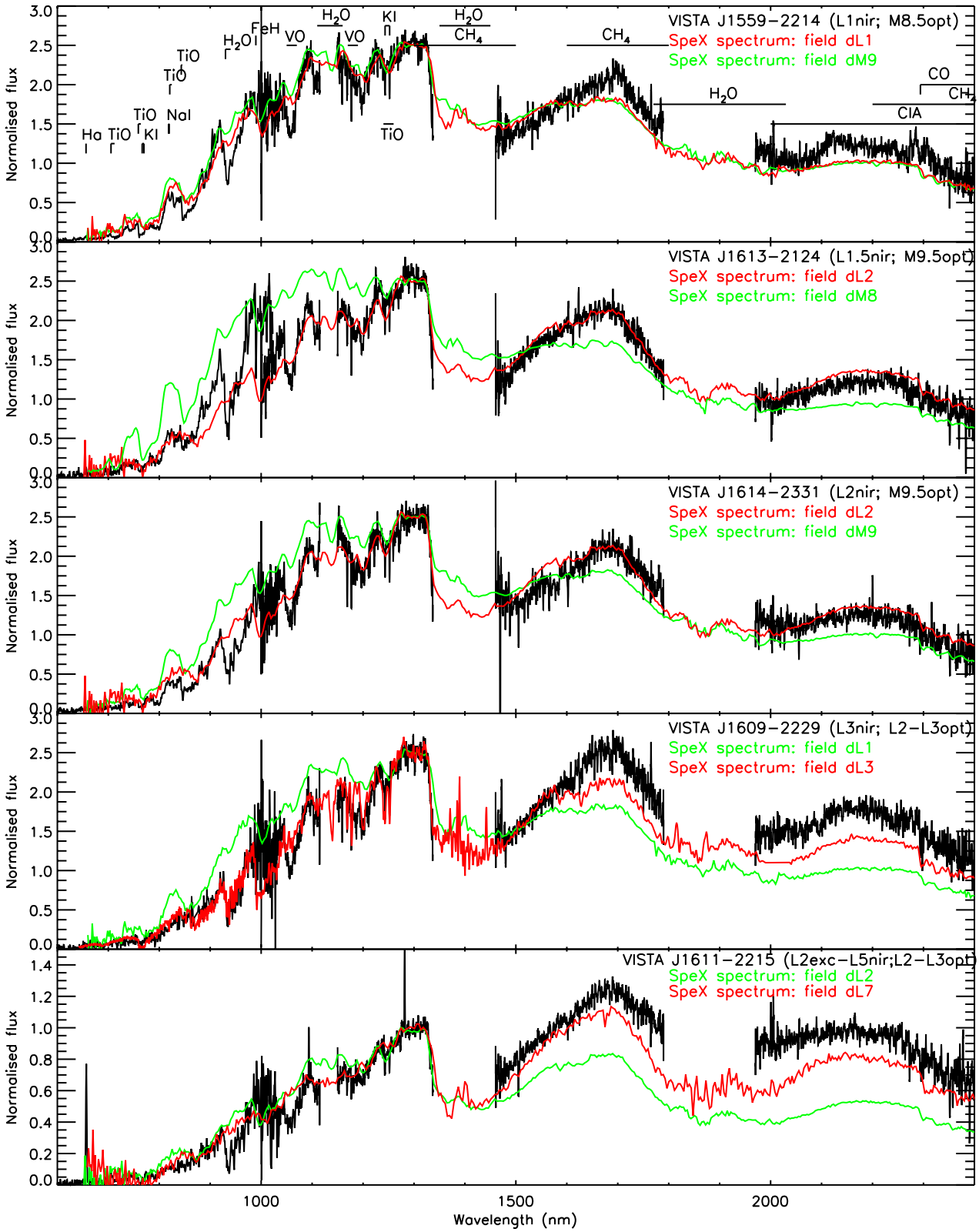

Figure 16. Optical (black) plus near-infrared (red; smoothed by a factor of 21) spectral energy distributions for UpSco targets with spectroscopic data from GTC/OSIRIS and VLT/X-shooter, respectively. First page, from top to bottom: VISTA J1559−2214 (M8.5opt, L1ir); VISTA J1613−2124 (M9opt, L1.5ir); VISTA J1614−2331 (M9.5opt, L2ir); VISTA J1609−2229 (L2–L3opt, L3ir); VISTA J1611−2215 (L2–L3opt, L2exc–L5ir). Second page, from top to bottom: VISTA J1607−2146 (L2–L3opt, L4.5ir); VISTA J1614−2211 (L1–L2opt, L4.5ir); VISTA J1605−2403 (L2opt, L4.5ir); VISTA J1604−2241 (L1–L2opt, L6ir); VISTA J1604−2134 (L1–L2opt, L6ir). Third page, from top to bottom: the two latest member candidates VISTA J601−2212 (L4opt, L7ir) and VISTA J615−2229 (L4opt, L7ir). Overplotted are SpeX spectra for spectral types corresponding to the infrared and optical classifications of our targets, demonstrating that the overall spectral energy distribution matches the infrared classification best. All spectra are normalized at 1.30–1.32 μm.

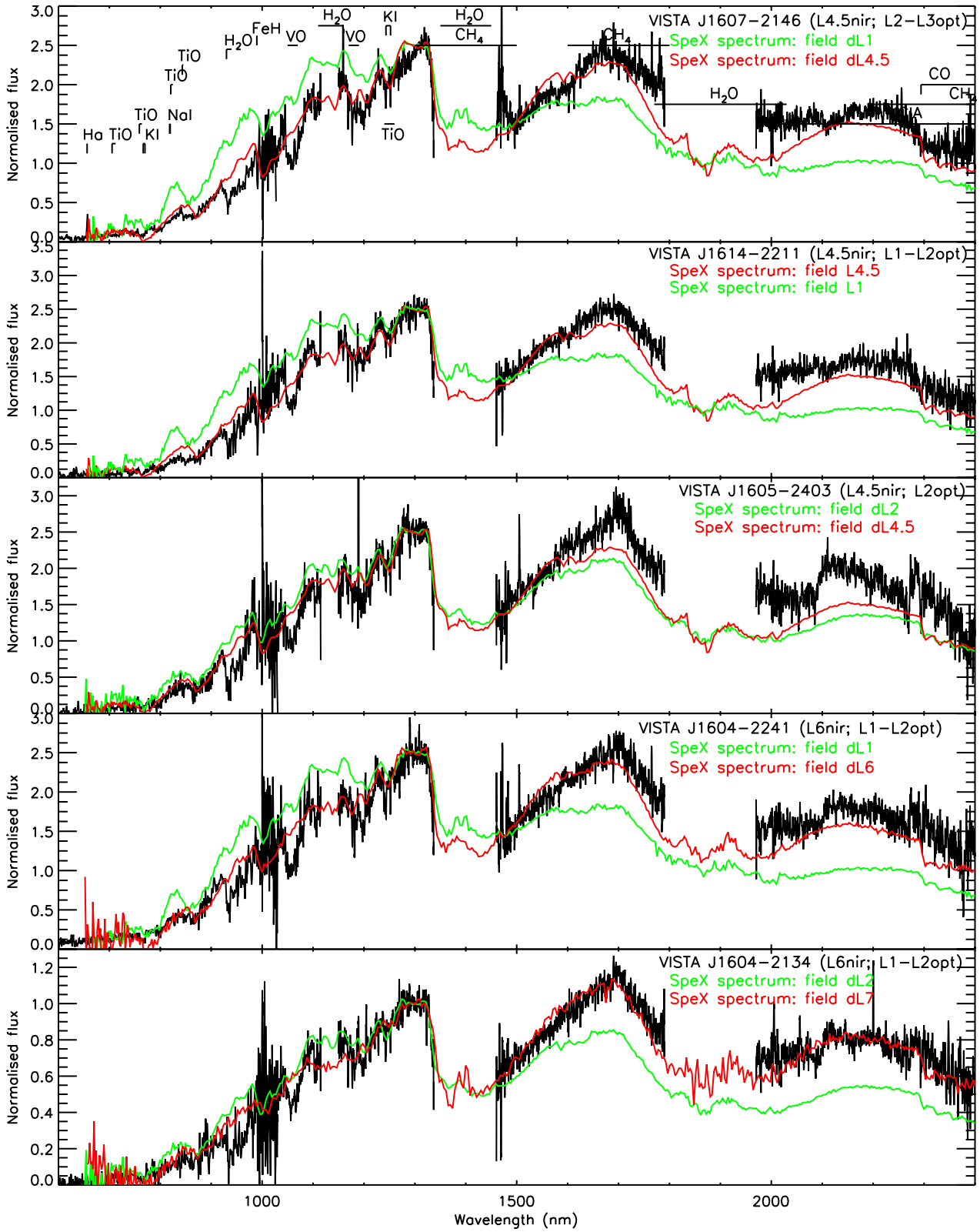

Figure 16 – *continued.*

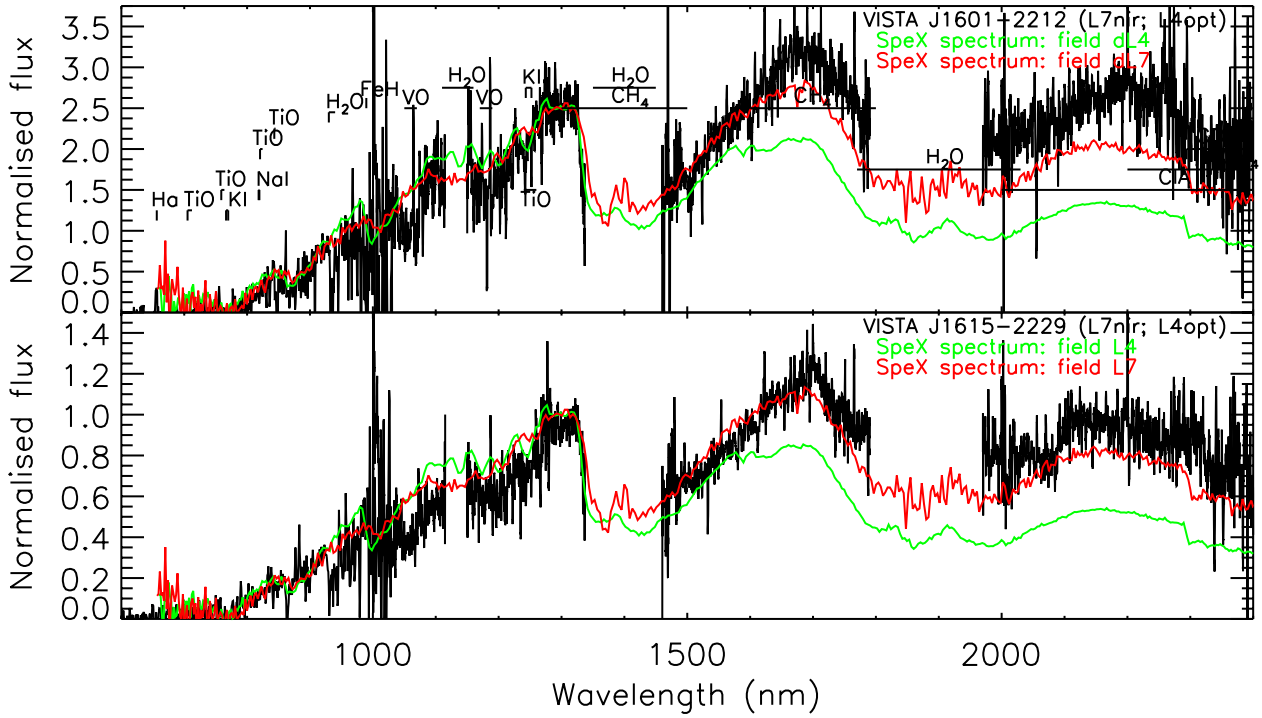

Figure 16 – *continued.*

resolution of ∼4000 (i.e. a spectral point every 0.06 nm), corresponding to an uncertainty in radial velocity of ∼15 km s^{-1}.

We also measured the observed positions of the potassium (K I) doublets at 1.169/1.177 μm and 1.243/1.252 μm. We compared these values with the nominal values taken from the NIST atomic spectra data base.[7] We multiplied the difference by the speed of light to derive a Doppler shift in km s^{-1} after correcting for the barycentric velocities. We calculated the error bars for each object based on the dispersion in the four different measurements (or three only when one was clearly discrepant). The final error bars represent the quadratic sum of the individual measurements and the uncertainty of the reference object (4.83 km s^{-1}). These uncertainties are much larger than the ones from the cross-correlation technique, but more in line with the spectral resolution of the X-shooter spectra and the faintness of our objects. We list the final radial velocities in Table 7.

We find that both methods give compatible values within 1σ of the error bars. We plot the Doppler shifts from the cross-correlation technique corrected for the radial velocity of our reference (VISTA J1559−2214; −9.05 ± 4.83 km s^{-1}) in Fig. 17. We compare the distribution of our candidates with the distribution of radial velocities of higher mass members (values in table 12 of Pecaut et al. 2012, and references therein; see also Duflot, Figon & Meyssonnier 1995; Barbier-Brossat & Figon 2000; Gontcharov 2006; Chen et al. 2011; Dahm, Slesnick & White 2012), values of which range from −10 to 0 km s^{-1}. The two faintest members exhibit large radial velocities but with larger uncertainties, also consistent with the mean velocities of UpSco members. The only source that lies 2σ away from the higher mass members with the largest Doppler shifts is VISTA J1605−2130 (dL2), so we set its radial velocity membership to '?'. It is worth noting that this source was also a doubtful member, because it displays blue infrared colour, its near-infrared spectrum did not show obvious youth features and

[7] https://physics.nist.gov/PhysRefData/ASD/lines_form.html

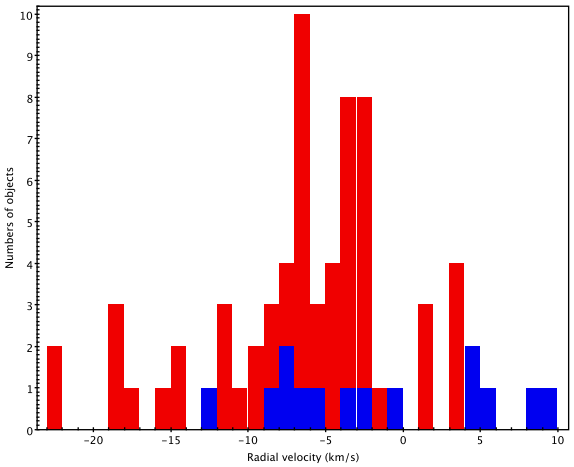

Figure 17. Histogram of our radial velocity measurements (blue) compared with observed radial velocities of high-mass members of UpSco (red; table 12 in Pecaut et al. 2012).

it has a discrepant radial velocity. All the other candidates with X-shooter spectra cannot be discarded as members, based on the low accuracy of our radial velocity measurements (Table 8). Overall, we have identified two clear non-members based on their *I*-band photometry, two non-members from their near-infrared spectroscopy and/or radial velocity and one doubtful currently unclassified. We infer a minimum contamination level of 4/28–5/28 = 14–18 per cent among photometric candidates and 2/15–3/15 = 13.3–20 per cent among candidates with spectroscopic follow-up.

5.6 Effective temperatures and gravities

We have used the spectral energy distribution (SED) analyser tool implemented in the Spanish virtual observatory (VOSA: Bayo

Table 9. Results of the best fits to the photometric spectral energy distribution of UpSco members with spectral type (SpT) from this study through direct comparison with theoretical models using the VOSA tool. Uncertainties in temperatures, gravities and metallicities are ± 50 K, ± 0.25–0.50 dex and ± 0.2 dex, respectively. These errors include neither the systematics nor the accuracy of the procedure (± 500 K in $T_{\rm eff}$). The last column gives the spectral type from template fitting using the spectral library from NIRSPEC (1), the L and T dwarf archive (2) and the IRTF/SpeX archive (3).

ID	Name VISTA J	SpT_{NIR}	Model	$T_{\rm eff}$ K	log (g) cgs	[M/H]	Template
1	1559−2214	L1.0	bt-settl	1800	5.0	0.0	L0 (1)
2	1613−2124	L1.5	bt-dusty	1800	4.5	0.0	T0 (2)
3	1614−2331	L2.0	bt-dusty	1900	4.5	0.0	L0 (1)
4	1605−2130	dL2.0	bt-settl	1800	5.0	0.0	L3 (3)
5	1611−2215	L5.0	bt-settl-cifist	1700	4.0	0.0	L6 (2)
6	1609−2222	dL4.5	bt-dusty	1600	5.0	0.0	L2 (1)
7	1609−2229	L3.0	bt-settl-cifist	1800	5.0	0.0	L2 (1)
8	1607−2146	L4.5	bt-settl-cifist	1800	5.0	0.0	L2 (1)
9	1604−2241	L6.0	bt-dusty	1600	5.5	0.0	L4 (2)
10	1614−2211	L4.5	bt-settl-cifist	1500	2.5	0.0	L4.5 (2)
11	1605−2403	L4.5	bt-settl	1600	3.5	0.0	L2 (1)
12	1602−2057	????	bt-dusty	1600	4.5	0.0	L3 (2)
13	1604−2134	L6.0	bt-settl-cifist	1750	5.0	0.0	L5 (2)
14	1601−2212	L7.0	bt-settl-cifist	1700	4.0	0.0	L6 (2)
15	1615−2229	L7.0	bt-settl-cifist	1700	4.0	0.0	L6 (2)

et al. 2008) to infer the effective temperatures ($T_{\rm eff}$), surface gravities and metallicities of our UpSco candidates by comparison with a set of theoretical models. We investigated the validity of the VOSA fitting tool on known field late-M, L and T dwarfs, before applying it to our sample. We input in VOSA the samples of ultracool dwarfs with effective temperature derived by Dahn et al. (2002) and Vrba et al. (2004). We used the VOSA photometry tool to extract optical and infrared photometry from various large-scale surveys, including Sloan, 2MASS, UKIDSS, VISTA and WISE, to construct their spectral energy distributions. We kept in the final sample only sources with at least five photometric points in the near- and mid-infrared. We fit their distribution with three different types of models incorporated in VOSA: BT-Settl (Allard, Homeier & Freytag 2012), BT-DUSTY (Allard et al. 2012) and BT-CIFIST (Baraffe et al. 2015) for the L dwarfs and only BT-Settl for the T dwarfs, because of the validity range of the other two models. We plot the $T_{\rm eff}$ from VOSA with black dots in Fig. 19 and compare them with the values of Dahn et al. (2002) and Vrba et al. (2004), shown in green and red, respectively. We observe that the models reproduce the overall trend in temperature well for the full high-gravity late-M, L and T dwarf sequence (Dahn et al. 2002; Vrba et al. 2004), but with a very large dispersion of about 500 K. We find that model fits tend to underestimate the $T_{\rm eff}$ for L dwarfs by a few hundred K, but this trend is only valid for old field dwarfs (the effect is unknown at low ages).

For our purposes, we compared the photometric SEDs, including GTC OSIRIS *i*-band photometry, VISTA *ZYJ* magnitude (L13), UKIDSS *HK* photometry (∼0.88–2.5 μm: Hewett et al. 2006) and WISE $w1 + w2$ passbands (3.4 and 4.6 μm), with three sets of models with a limited range of parameters: BT-Settl (Allard et al. 2012), BT-DUSTY (Allard et al. 2012) and BT-CIFIST (Baraffe et al. 2015) for $T_{\rm eff}$ = 1200–3500 K, surface gravities between 2.5 and 5.5 dex and metallicities ranging from −0.5 to 0.5 dex. In other words, we assumed solar metallicity for members of UpSco, which is expected for such a young nearby OB association. We also assumed a mean distance of ∼145 pc for UpSco (de Bruijne et al. 1997).

We list the physical parameters derived from the photometric fits in Table 9 and show the SEDs in Fig. 18. We note that the best fit is obtained for different models depending on the targets. All our targets have solar metallicity, with a typical error of ± 0.2 dex. All objects exhibit gravity in the log (g) = 3.5–5.0 range, with uncertainties of 0.5 dex (the steps of the models). We expect log (g) = 4.0 dex for brown dwarfs still contracting at the age of UpSco, while log (g) = 2.5 is derived for VISTA J1614−2211, the gravity of which is too low according to model predictions. The effective temperatures lie between 1500 and 1900 K, with uncertainties less than 60 K. One source, VISTA J1604−2241, is best fitted with log (g) of 5.5 dex, which is quite high for young brown dwarfs, highlighting current uncertainties in fitting schemes and atmospheric models. Keeping in mind current flaws in theoretical models reproducing the spectra of brown dwarfs, the large dispersion of temperatures observed for L dwarfs and the fact that young L dwarfs might be ∼100–300 K cooler than their old counterparts (Filippazzo et al. 2015), our $T_{\rm eff}$ represents a first-guess estimate. More accurate temperatures could be inferred if we knew the range of radii for UpSco L-type brown dwarfs, but such a measurement is currently available only for one (isolated) eclipsing brown dwarf binary in Orion (0.48–0.68 $R_\odot$: Stassun, Mathieu & Valenti 2006, 2007).

We have also taken advantage of the template fitting procedure in VOSA, which uses a sequence of spectral libraries: the NIRSPEC Brown Dwarf spectroscopic survey (McLean et al. 2003, 2007), L and T dwarf data archive (Knapp et al. 2004; Golimowski et al. 2004; Chiu et al. 2006), SpeX prism library,[8] Keck LRIS spectra of late-M, L and T dwarfs (Kirkpatrick, Henry & McCarthy 1991; Kirkpatrick et al. 1999) and the data base of Collinder 69 (Bayo et al. 2011). We observe that the best fits were returned from the first three archives, which use mainly near-infrared spectra instead of the full optical/near-infrared/mid-infrared range. We see that a few targets are fitted well by known templates, although the majority tend to

[8] http://pono.ucsd.edu/~adam/browndwarfs/spexprism/index_old.html

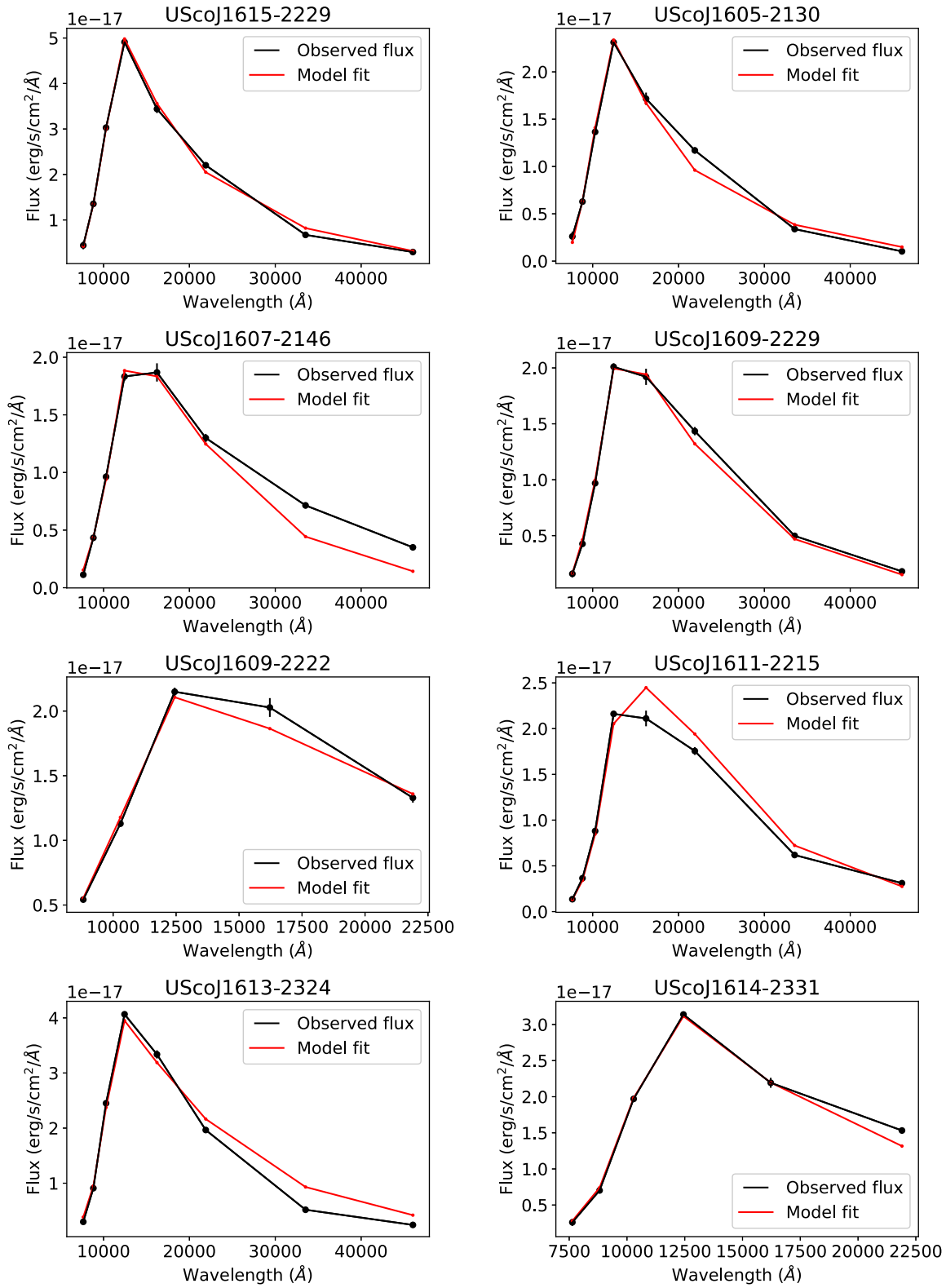

Figure 18. Spectral energy distributions (red dots) of UpSco candidates compared with theoretical models (blue spectra) to derive temperatures, gravities and metallicities.

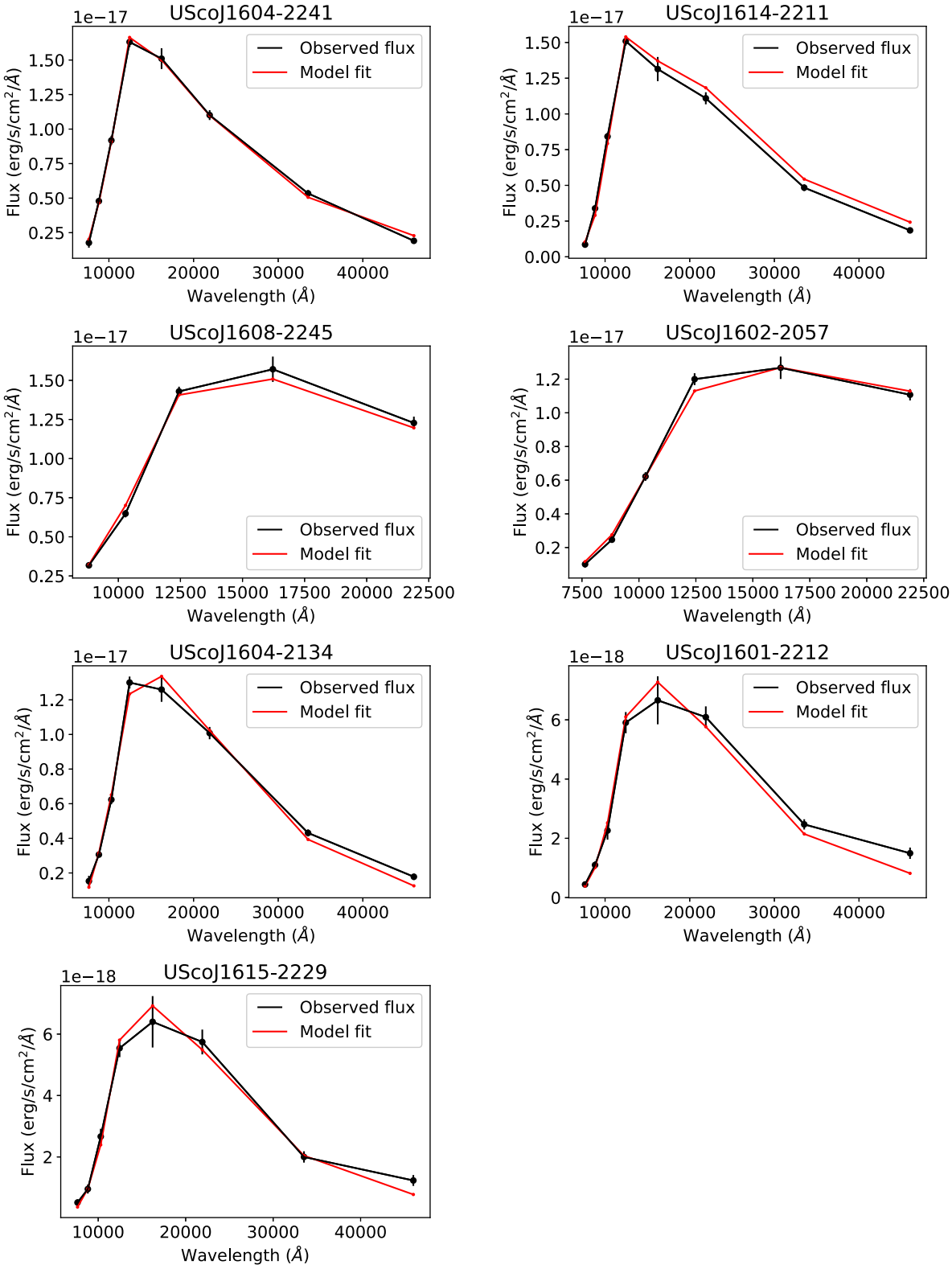

Figure 18 – *continued.*

return earlier spectral types, consistent within 2–3 subclasses with those assigned in this article (Section 5.2.3; Table 8), except for VISTA J1613−2124, classified as a T0 dwarf from direct comparison with a 1.0–2.5 μm spectrum. On the light of the discrepancies observed between photometric and spectroscopic spectral types, we caution the use of the template fitting procedure to assign temperatures, especially at low ages. We list the assigned spectral types from template fitting in the last column of Table 9.

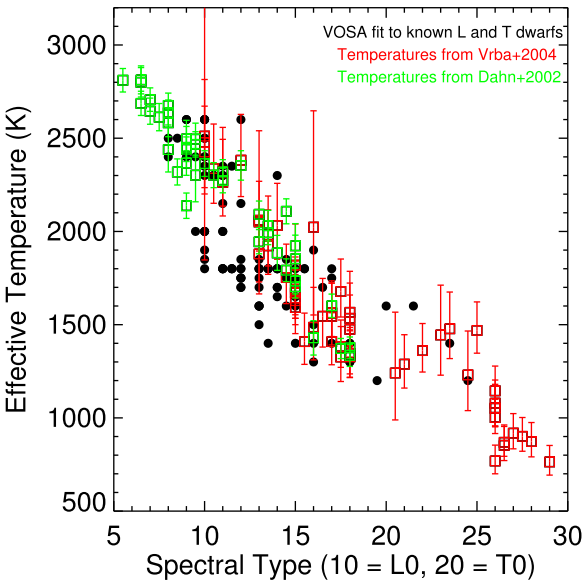

Figure 19. Effective temperatures of known late-M, L and T dwarfs with spectral types published by Dahn et al. (2002, green symbols) and Vrba et al. (2004, red symbols) compared with the model-dependent $T_{\rm eff}$ derived from the VOSA fitting tool (black dots). The typical error bar of VOSA temperatures is around 50–100 K.

5.7 Bolometric corrections

We computed bolometric corrections (BCs) for our UpSco candidates, assuming that the observed spectroscopic and photometric fluxes come from a single source (i.e. the target). First, we computed the BCs including the optical and near-infrared spectra from the GTC and VLT, respectively. We integrated the spectra from ∼563–2480 nm and added the flux from the WISE passbands (up to 5.34 μm). We did not include those objects lacking WISE photometry (Table 6). We integrated the solar metallicity BT-Settl models for log (g) of 4.5 dex and temperatures of 2000, 1800 and 1600 K for L1–L2, L4 ± 1 and L6–L7 dwarfs, respectively. We integrated the BT-Settl models for wavelengths shortwards of 563 nm and longer than 5.56 μm (upper limit of the WISE $w2$ filter). The contribution from the 2000- and 1600-K models represents only ∼2.6 and ∼5.4 per cent, respectively. We assumed an absolute solar bolometric magnitude of 4.74 for the Sun, following the IAU recommendation. We report bolometric magnitudes and corrections in the top panel of Table 10 and plot the J- and K-band BCs as red dots in Fig. 20, compared with the BCs of field L dwarfs (black dots) taken from Dahn et al. (2002) and Golimowski et al. (2004). In Fig. 20, we added the polynomial fits and their associated dispersions reported for young and old field L dwarfs in blue and grey, respectively (Filippazzo et al. 2015).

In a second step, we calculate the BCs for our candidates by integrating their near-infrared spectra only and adding the WISE photometry to gauge the contribution of the optical spectrum. The flux concentrated in the aforementioned models shortwards of 1000 nm and longwards of the WISE $w2$ passband represent 10 per cent at most in all cases. We obtained similar BCs within ± 0.04 mag for all sources with both optical+infrared and infrared-only contributions, suggesting that the contribution from the optical regions is very small in our targets. We list the BCs for the candidates with WISE photometry and infrared spectra in the bottom panel of Table 10 and plot their BCs as green dots in Fig. 20. We note that our K-band BC for our L1 member of UpSco is comparable to the value obtained by Todorov, Luhman & McLeod (2010) for M9.5–L0 members of Taurus ($BC_K \sim 3.40$ mag).

In the top panel of Fig. 20, depicting BC_J as a function of spectral type, we observe a decreasing trend of BC with later spectral type for young UpSco members and field L dwarfs. Our BC_J lie within the dispersion of field L dwarfs derived by Filippazzo et al. (2015). In the case of BC_K (bottom panel in Fig. 20), we see a slight increase towards later spectral types, a different trend from the one observed for the samples of field and young L dwarfs presented in Filippazzo et al. (2015). This has a clear impact on the luminosity and, more

Table 10. Bolometric corrections in several filters for the three UpSco candidates with optical and near-infrared spectroscopy (top) and near-infrared spectroscopy only (bottom). The Δ_{BC_J} and Δ_{BC_K} represent the difference between our measurements for UpSco L dwarfs and the mean values taken from the polynomial fits for field dwarfs from Filippazzo et al. (2015).

ID	Name	SpT_{NIR}	m_{bol} mag	BC_J mag	BC_K mag	BC_{w1} mag	BC_{w2} mag	Δ_{BC_J} mag	Δ_{BC_K} mag
1	1559−2214	L1.0	19.34	2.01	3.37	4.13	4.56	0.09	0.16
2	1613−2124	L1.5	19.57	2.04	3.46	4.08	4.58	0.14	0.22
7	1609−2229	L3.0	19.92	1.80	3.62	4.40	4.57	0.12	0.32
8	1607−2146	L4.5	19.75	1.63	3.39	4.65	5.20	−0.01	0.07
10	1614−2211	L4.5	20.18	1.72	3.51	4.61	4.89	0.08	0.19
5	1611−2215	L5.0	19.75	1.50	3.69	4.55	4.98	−0.09	0.37
9	1604−2241	L6.0	20.18	1.64	3.49	4.71	4.92	0.14	0.19
13	1604−2134	L6.0	20.30	1.60	3.56	4.61	4.98	0.10	0.26
14	1601−2212	L7.0	20.97	1.40	3.68	4.67	5.45	−0.04	0.42
15	1615−2229	L7.0	20.94	1.42	3.67	4.41	5.21	−0.01	0.40
1	1559−2214	L1.0	19.41	2.02	3.38	4.20	4.63	0.09	0.16
2	1613−2124	L1.5	19.60	2.06	3.49	4.10	4.61	0.16	0.25
7	1609−2229	L3.0	19.92	1.79	3.59	4.38	4.55	0.00	0.30
8	1607−2146	L4.5	19.75	1.60	3.35	4.61	5.16	0.04	0.03
10	1614−2211	L4.5	20.17	1.73	3.50	4.60	4.88	0.09	0.18
5	1611−2215	L5.0	19.75	1.51	3.68	4.54	4.97	−0.09	0.36
9	1604−2241	L6.0	20.18	1.66	3.50	4.72	4.93	0.16	0.20
13	1604−2134	L6.0	20.30	1.61	3.56	4.61	4.97	0.11	0.26
14	1601−2212	L7.0	20.95	1.37	3.66	4.65	5.43	−0.06	0.39
15	1615−2229	L7.0	20.90	1.39	3.64	4.37	5.17	−0.04	0.37

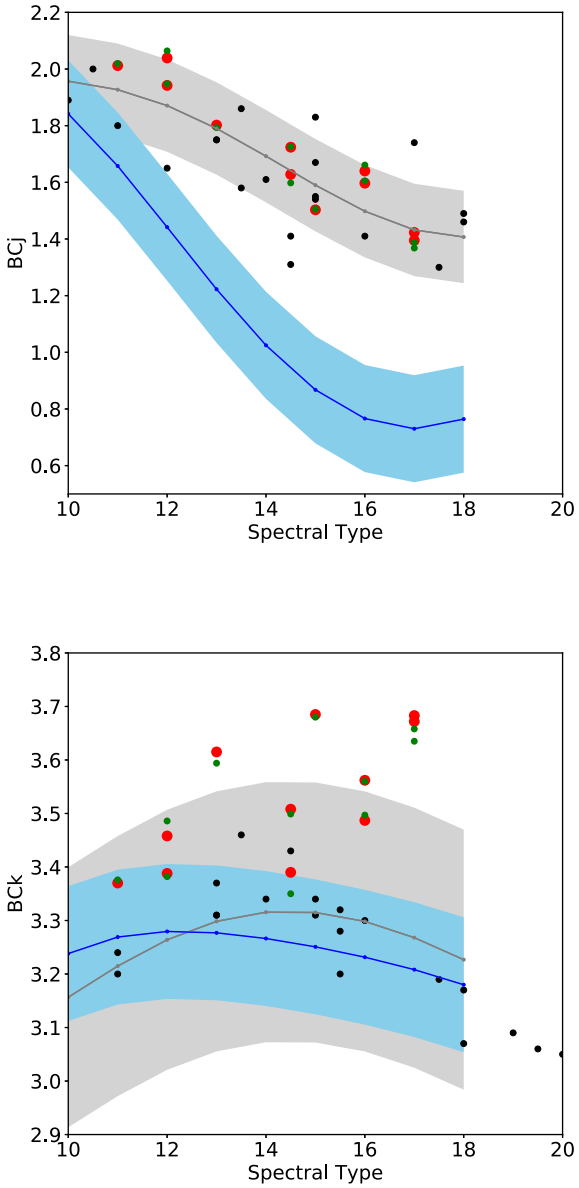

Figure 20. *J*-band (top) and *K*-band (bottom) bolometric correction versus spectral type for field L dwarfs (black dots: Dahn et al. 2002; Golimowski et al. 2004), along with our UpSco candidates with optical and infrared spectroscopy (red dots) and infrared spectroscopy only (green dots). We overplotted the polynomial fits and dispersions of the BC_J and BC_K relations presented in Filippazzo et al. (2015) for field (grey) and young (blue) L dwarfs. Note for *x*-axis: 10≡L0, 12≡L2, etc....

importantly, on the mass of young L dwarfs, because higher values of BC_K indicate that objects become less luminous, therefore less massive. Fig. 20 provides an additional illustration of what is seen in Fig. 16, where the spectra of UpSco objects appear systematically redder in the *K* band than the corresponding high-gravity sources of related near-infrared spectral type.

5.8 Wide companions

We looked for wide companions cross-matching our list of 15 VISTA candidates with known UpSco members (Luhman & Mamajek 2012) within a matching radius of 30 arcsec (corresponding to an upper projected physical separation of 4350 au at the distance of USco), but none was found. The catalogue of UpSco members from Luhman & Mamajek (2012) included the most massive members (e.g. τ Sco; $J = 3.4$ mag) all the way down to the coolest members known at that time, with spectral types around M9/L0 ($J \sim 16.6$–17.2 mag). We repeated the same process with the list of 16 L0–L2 dwarfs in table 1 of Lodieu et al. (2008) without success. In total, we searched for wide companions around 29 L dwarfs (two in common between the aforementioned samples), suggesting a frequency of wide companions to early-L dwarfs below 3.4 per cent at separations larger than ∼1.5 arcsec and spectral types between B0 and M9/L0, corresponding to ∼220 au at the distance of UpSco. Our conclusions also supplement the low frequency of close companions (<7 per cent) from an adaptive optic survey of 14 L0–L1 from Lodieu et al. (2008) by Biller et al. (2011). We conclude that wide pairs with components separated by more than ∼200 au are rare. Only a few systems have indeed been discovered in USco: USco CTIO 108B (∼670 au: Ardila et al. 2000; Béjar et al. 2008), 1RXS J160929.1−210524 (∼330 au: Lafrenière et al. 2008, 2010) and HIP 78530B (∼700 au: Lafrenière et al. 2011). Our upper limit is consistent with the frequency of ∼4 per cent of wide (250–1000 au) brown dwarf (0.005–0.040 $M_\odot$) companions around higher mass members of UpSco (0.2–10 $M_\odot$: Lafrenière et al. 2014) and the $\sim 0.6 \pm 0.3$ per cent occurrence of wide (400–4000 au) companions down to 0.005 $M_\odot$ around M7.5–M9 members (Aller et al. 2013).

The closest potential system we found cross-matching the above catalogues is located at 69.3 arcsec or ∼10 000 au. It is composed of the X-ray emitter M1 dwarf 2MASS J16063741−2108404 (called 'primary' here) and VISTA J16060629−2335133, classified as a L0 in the infrared (Lodieu et al. 2008) and M9 in the optical (this work). The proper motion in right ascension and declination extracted from the UKIDSS GCS catalogue for the primary and secondary are -10.25 ± 4.11, -15.24 ± 4.11) and (-6.60 ± 2.46, -19.21 ± 2.46) mas yr^{-1}, respectively. The primary has a mass of 0.6 $M_\odot$ and has a previously known companion located at 1.279 ± 0.003 arcsec (position angle of 33.9 ± 0.3 degrees), equivalent to ∼185 au at the distance of UpSco (Köhler et al. 2000). The brightness ratio is 0.917 ± 0.001 in the *K* band. The catalogue of Luhman & Mamajek (2012) contains 863 B–M members over a (conservative) area of ∼72 deg^2, implying ∼0.0033 sources per $arcmin^2$. The probability of finding one member of UpSco in 4.3 $arcmin^2$ is of the order of 41.5 per cent. At this stage we cannot draw any firm conclusion: the probability indicates that companionship might be either true or not. If true, this system, composed of a low-mass star and planetary-mass companion, would be of great interest and would support early theoretical suggestions that primary stars of multiple systems with wide brown dwarf companions tend to be binary themselves (e.g. Delgado-Donate, Clarke & Bate 2003).

CONCLUSIONS AND FUTURE WORK

We presented a dedicated photometric and spectroscopic follow-up of photometric and astrometric candidates identified in a deep and wide near-infrared survey of 13.5 deg^2 in the central region of UpSco. Throughout this work, we argue in favour of a high success rate of our photometric and astrometric selection, higher than 80 per cent. Indeed, two sources are rejected with additional optical photometry among 28 candidates with *i*-band photometric follow-up. Moreover, two candidates are classified as field dwarfs and another one remains doubtful, suggesting at most three contaminants in our near-infrared spectroscopic sample of 15 candidates. As a consequence, the conclusion drawn earlier in L13 remains

valid: the UpSco mass function in the planetary regime is flat or most likely decreasing.

The main results of our study can be summarized as follows.

(i) We derive Sloan *i*-band magnitudes for 25 sources and place lower limits for another three substellar candidates in UpSco.

(ii) We present VLT/X-shooter near-infrared (1.0–2.5 μm) spectra for 15 candidates fainter than $J \sim 17$ mag, equivalent to ∼10 Jupiter masses at the age (∼5–10 Myr) and distance of UpSco.

(iii) We present VLT/X-shooter optical + near-infrared spectra of six late-M dwarf candidates previously recognized as members and classified in the optical.

(iv) We present GTC/OSIRIS low-resolution optical spectra for all L-type members with near-infrared spectra taken with the X-shooter instrument.

(v) We exploit the WISE mid-infrared survey to extend the current UpSco sequence of members to fainter magnitudes and lower masses and look for excesses.

(vi) We classify our targets based on their SED in the near-infrared, rejecting only two of the 15 targets with spectroscopy and casting doubt on another one. This fact demonstrates the strength of our photometric and astrometric selections to pick up substellar and planetary-mass members in UpSco.

(vii) We observe a trend towards earlier spectral types in the optical compared with the infrared for several members classified as M9–L1 in Lodieu et al. (2008) and five of our targets with both optical and infrared spectra. This trend seems to affect sources later than M9 all the way to late-L dwarfs.

(viii) We detect Hα in emission in four L-type sources. Two objects, VISTA J1611−2215 and VISTA J1607−2146, also have likely mid-infrared flux excesses, thus supporting the disc accretion scenario and providing evidence of the persistence of accretion at very low masses and at the age of the UpSco association (5–10 Myr).

(ix) We measure the pseudo-equivalent widths of gravity-sensitive doublets present in the near-infrared, the strengths of which confirm the youth of our candidates.

(x) We present a wide variety of spectral indices, comparing our sample with a sample of young L dwarfs and several field L0–L9 dwarfs. We show that a few indices (H-cont, CO, CH4-H, FeH-H) are highly sensitive to gravity (or age), while most of the water-based indices are good proxies for spectral typing. The VO absorption features at ∼1.06 and ∼1.18 μm are still present in late-L dwarfs at the age of UpSco.

(xi) We measure the radial velocities of confirmed members from the X-shooter infrared spectra. The distribution of velocities is consistent with the mean value reported for higher mass members.

(xii) We infer effective temperatures and gravities, fitting the full photometric spectral energy distribution from 0.8–4.5 μm with different sets of theoretical models. We find that these physical parameters tend to be underestimated with respect to the parameters derived from spectral energy distribution model atmosphere fits to the spectra.

(xiii) We derive bolometric corrections for our L dwarf members and find similar values and trends for BC_J over the L1–L7 range, but a slightly different tendency for BC_K for young L dwarfs compared with field L dwarfs.

(xiv) We search for higher mass wide companions to our planetary-mass members and place an upper limit of 3.4 per cent on the frequency of systems with projected physical separations greater than 100 au.

Our deep survey is currently limited by the depth of the *Y* band, because the final stack is only 0.7 mag deeper in *Y* than in *J* (21.2 mag versus 20.5 mag completeness limits), while the colours of the coolest sources confirmed spectroscopically are in the 1.4–1.8 mag range (see fig. 3 of L13). Hence, our deep *J* band might contain some yet-to-be-found T-type dwarfs with an age of ∼5–10 Myr. Assuming that our survey reaches members with masses as low as $5M_{\rm Jup}$, we might still be far from being able to test opacity limit for the fragmentation, i.e. the mass at which one object is unable to contract further because it cannot radiate its heat to collapse further (Low & Lynden-Bell 1976; Rees 1976; Boss 2001). Indeed, according to the COND03 models (Baraffe et al. 2002), a $1M_{\rm Jup}$ brown dwarf is 4.0 and 5.4 mag fainter in *J* than a $5M_{\rm Jup}$ one at 5 and 10 Myr, respectively. In the future, we might receive some hints on the theory of fragmentation from upcoming space missions like the *James Webb Space Telescope* (*JWST*: Clampin 2008),[9] *Wide Field Infrared Survey Telescope* (*WFIRST*)[10] and *Euclid* (Mellier 2016)[11], as well as the Large Synoptic Survey Telescope from the ground (Ivezic et al. 2008).[12]

ACKNOWLEDGEMENTS

NL was partly funded by the Ramón y Cajal fellowship number 08-303-01-0. NL and VJSB are supported by programme AYA2015-69350-C3-2-P and MRZO by programme AYA2016-79425-C3-2-P from the Spanish Ministry of Economy and Competitiveness (MINECO).

KPR acknowledges CONICYT PAI Concurso Nacional de Inserción en la Academia, Convocatoria 2016 Folio PAI79160052. NL thanks Kevin Luhman for providing his own spectra of young brown dwarfs. We thank the referee for comments that improved the clarity of the article.

This work is based on observations (programmes GTC4-14A and GTC25-16A, PI Lodieu; and GTC2-17A EMIR Science Verification, PI Zapatero Osorio) made with the Gran Telescopio Canarias (GTC), operated on the island of La Palma in the Spanish Observatorio del Roque de los Muchachos of the Instituto de Astrofísica de Canarias. We are thankful to F. Garzón and the EMIR consortium for the development of this instrument on the GTC.

Based on observations collected at the European Organization for Astronomical Research in the Southern hemisphere under ESO programme(s) 095.C-0812(A) and 089-C.0102(ABC).

Based on data from the UKIRT Infrared Deep Sky Survey (UKIDSS). The UKIDSS project is defined in Lawrence et al. (2007) and uses the UKIRT Wide Field Camera (WFCAM: Casali et al. 2007). The photometric system is described in Hewett et al. (2006) and the calibration is described in Hodgkin et al. (2009). The pipeline processing and science archive are described in Irwin et al. (in preparation) and Hambly et al. (2008).

This publication makes use of VOSA, developed under the Spanish Virtual Observatory project supported from the Spanish MICINN through grant AyA2011-24052.

This research has made use of the Simbad and Vizier (Ochsenbein, Bauer & Marcout 2000) data bases, operated at the Centre de Données Astronomiques de Strasbourg (CDS), and NASA's Astrophysics Data System Bibliographic Services (ADS). This research has also made use of the IRTF spectral library at http://irtfweb.ifa.hawaii.edu/~spex/IRTF_Spectral_Library/index.html.

[9] https://www.jwst.nasa.gov/
[10] https://wfirst.gsfc.nasa.gov/
[11] http://sci.esa.int/euclid/
[12] https://www.lsst.org/

REFERENCES

Adame L. et al., 2011, ApJ, 726, L3
Allard F., Hauschildt P. H., Alexander D. R., Tamanai A., Schweitzer A., 2001, ApJ, 556, 357
Allard F., Homeier D., Freytag B., 2011, in Johns-Krull C. M., Browning M. K., West A. A., eds. ASP Conf. Ser. Vol. 448, 16th Cambridge Workshop on Cool Stars, Stellar Systems, and the Sun. Astron. Soc. Pac., San Francisco, p. 91
Allard F., Homeier D., Freytag B., 2012, Phil. Trans. R. Soc. A, 370, 2765
Aller K. M. et al., 2013, ApJ, 773, 63
Allers K. N., Liu M. C., 2013, ApJ, 772, 79
Allers K. N. et al., 2007, ApJ, 657, 511
Alonso R., Deeg H. J., Hoyer S., Lodieu N., Palle E., Sanchis-Ojeda R., 2015, A&A, 584, L8
Alves de Oliveira C., Moraux E., Bouvier J., Bouy H., Marmo C., Albert L., 2010, A&A, 515, A75
Alves de Oliveira C., Moraux E., Bouvier J., Bouy H., 2012, A&A, 539, A151
Alves de Oliveira C., Moraux E., Bouvier J., Duchêne G., Bouy H., Maschberger T., Hudelot P., 2013, A&A, 549, A123
Ardila D., Martín E., Basri G., 2000, AJ, 120, 479
Baraffe I., Chabrier G., Allard F., Hauschildt P. H., 2002, A&A, 382, 563
Baraffe I., Homeier D., Allard F., Chabrier G., 2015, A&A, 577, A42
Baraffe I., Elbakyan V. G., Vorobyov E. I., Chabrier G., 2017, A&A, 597, A19
Barbier-Brossat M., Figon P., 2000, A&AS, 142, 217
Barrado y Navascués D., Zapatero Osorio M. R., Béjar V. J. S., Rebolo R., Martín E. L., Mundt R., Bailer-Jones C. A. L., 2001, A&A, 377, L9
Barrado y Navascués D. et al., 2007, ApJ, 664, 481
Batalha N. M., 2014, Proc. Natl Acad. Sci., 111, 12647
Bayo A., Rodrigo C., Barrado y Navascués D., Solano E., Gutiérrez R., Morales-Calderón M., Allard F., 2008, A&A, 492, 277
Bayo A. et al., 2011, A&A, 536, A63
Bayo A., Barrado y Navascués D., Huélamo N., Morales-Calderón M., Melo C., Stauffer J., Stelzer B., 2012, A&A, 547, A80
Béjar V. J. S., Zapatero Osorio M. R., Rebolo R., 1999, ApJ, 521, 671
Béjar V. J. S. et al., 2001, ApJ, 556, 830
Béjar V. J. S., Zapatero Osorio M. R., Pérez-Garrido A., Álvarez C., Martín E. L., Rebolo R., Villó-Pérez I., Díaz-Sánchez A., 2008, ApJ, 673, L185
Béjar V. J. S., Zapatero Osorio M. R., Rebolo R., Caballero J. A., Barrado D., Martín E. L., Mundt R., Bailer-Jones C. A. L., 2011, ApJ, 743, 64
Best W. M. J. et al., 2017, ApJ, 837, 95
Bihain G. et al., 2009, A&A, 506, 1169
Biller B., Allers K., Liu M., Close L. M., Dupuy T., 2011, ApJ, 730, 39
Bonnefoy M., Chauvin G., Lagrange A.-M., Rojo P., Allard F., Pinte C., Dumas C., Homeier D., 2014, A&A, 562, A127
Borucki W. J. et al., 2010, Science, 327, 977
Boss A. P., 2001, ApJ, 551, L167
Bouvier J. et al., 2008, A&A, 481, 661
Briceño C., Hartmann L., Stauffer J., Martín E., 1998, AJ, 115, 2074
Burgasser A. J. et al., 2002, ApJ, 564, 421
Burgasser A. J., Kirkpatrick J. D., McGovern M. R., McLean I. S., Prato L., Reid I. N., 2004, ApJ, 604, 827
Burgasser A. J., Geballe T. R., Leggett S. K., Kirkpatrick J. D., Golimowski D. A., 2006, ApJ, 637, 1067
Burgess A. S. M., Moraux E., Bouvier J., Marmo C., Albert L., Bouy H., 2009, A&A, 508, 823
Caballero J. A. et al., 2007, A&A, 470, 903
Casali M. et al., 2007, A&A, 467, 777
Cepa J. et al., 2000, Proc. SPIE, 4008, 623
Chabrier G., 2005, in Corbelli E., Palla F., Zinnecker H., eds, The Initial Mass Function 50 Years Later, Vol. 327 of Astrophysics and Space Science Library, The Initial Mass Function: from Salpeter 1955 to 2005. p. 41
Chen C. H., Mamajek E. E., Bitner M. A., Pecaut M., Su K. Y. L., Weinberger A. J., 2011, ApJ, 738, 122
Chiang P., Chen W. P., 2015, ApJ, 811, L16
Chiang P., Chen W.-P., Albert L., Liu M., Magnier E. A., 2015, MNRAS, 448, 522
Chiu K., Fan X., Leggett S. K., Golimowski D. A., Zheng W., Geballe T. R., Schneider D. P., Brinkmann J., 2006, AJ, 131, 2722
Clampin M., 2008, Adv. Space Res., 41, 1983
Covey K. R. et al., 2007, AJ, 134, 2398
Cruz K. L., Reid I. N., Liebert J., Kirkpatrick J. D., Lowrance P. J., 2003, AJ, 126, 2421
Cruz K. L., Kirkpatrick J. D., Burgasser A. J., 2009, AJ, 137, 3345
Cushing M. C., Tokunaga A. T., Kobayashi N., 2000, AJ, 119, 3019
Cushing M. C., Rayner J. T., Vacca W. D., 2005, ApJ, 623, 1115
Cutri R. M. et al., 2003, 2MASS All Sky Catalog of Point Sources. University of Massachusetts and Infrared Processing and Analysis Center (IPAC/California Institute of Technology), 2246, 0
D'Odorico S. et al., 2006, in Moorwood A. F. M., Iye M., eds, Society of Photo-Optical Instrumentation Engineers (SPIE) Conf. Ser. Vol. 6269, X-shooter UV- to K-band Intermediate-Resolution High-Efficiency Spectrograph for the VLT: Status Report at the Final Design Review, p. 626933
Dahm S. E., Slesnick C. L., White R. J., 2012, ApJ, 745, 56
Dahn C. C. et al., 2002, AJ, 124, 1170
David T. J., Hillenbrand L. A., Cody A. M., Carpenter J. M., Howard A. W., 2016, ApJ, 816, 21
David T. J. et al., 2016, Nat, 534, 658
Dawson P., Scholz A., Ray T. P., 2011, MNRAS, 418, 1231
Dawson P., Scholz A., Ray T. P., Marsh K. A., Wood K., Natta A., Padgett D., Ressler M. E., 2013, MNRAS, 429, 903
Dawson P., Scholz A., Ray T. P., Peterson D. E., Rodgers-Lee D., Geers V., 2014, MNRAS, 442, 1586
de Bruijne J. H. J., Hoogerwerf R., Brown A. G. A., Aguilar L. A., de Zeeuw P. T., 1997, in ESA SP-402: Hipparcos – Venice '97 Improved Methods for Identifying Moving Groups. p. 575
de Zeeuw P. T., Hoogerwerf R., de Bruijne J. H. J., Brown A. G. A., Blaauw A., 1999, AJ, 117, 354
Delgado-Donate E. J., Clarke C. J., Bate M. R., 2003, MNRAS, 342, 926
Duflot M., Figon P., Meyssonnier N., 1995, A&AS, 114, 269
Dupuy T. J., Liu M. C., 2012, ApJS, 201, 19
Fang Q., Herczeg G. J., Rizzuto A., 2017, ApJ, 842, 123
Faherty J. K. et al., 2016, ApJS, 225, 10
Filippazzo J. C., Rice E. L., Faherty J., Cruz K. L., Van Gordon M. M., Looper D. L., 2015, ApJ, 810, 158
Fukugita M., Ichikawa T., Gunn J. E., Doi M., Shimasaku K., Schneider D. P., 1996, AJ, 111, 1748
Gagné J., Lafrenière D., Doyon R., Malo L., Artigau É., 2014, ApJ, 783, 121
Gagné J., Lafrenière D., Doyon R., Malo L., Artigau É., 2015, ApJ, 798, 73
Gagné J. et al., 2015, ApJS, 219, 33
Garzón F., EMIR Team 2016, in Skillen I., Barcells M., Trager S., eds, ASP Conf. Ser. Vol. 507, Multi-Object Spectroscopy in the Next Decade: Big Questions, Large Surveys, and Wide Fields, EMIR, the NIR MOS and Imager for the GTC. Astron. Soc. Pac., San Francisco, p. 297
Gauza B., Béjar V. J. S., Pérez-Garrido A., Zapatero Osorio M. R., Lodieu N., Rebolo R., Pallé E., Nowak G., 2015, ApJ, 804, 96
Geballe T. R. et al., 2002, ApJ, 564, 466
Geers V., Scholz A., Jayawardhana R., Lee E., Lafrenière D., Tamura M., 2011, ApJ, 726, 23
Golimowski D. A. et al., 2004, AJ, 127, 3516
Gontcharov G. A., 2006, Astron. Lett., 32, 759
Gorlova N. I., Meyer M. R., Rieke G. H., Liebert J., 2003, ApJ, 593, 1074
Greenstein J. L., Trimble V. L., 1967, ApJ, 149, 283
Hambly N. C. et al., 2008, MNRAS, 384, 637
Harrington R. S., Dahn C. C., 1980, AJ, 85, 454
Herczeg G. J., Cruz K. L., Hillenbrand L. A., 2009, ApJ, 696, 1589
Hewett P. C., Warren S. J., Leggett S. K., Hodgkin S. T., 2006, MNRAS, 367, 454
Hillenbrand L. A., Hoffer A. S., Herczeg G. J., 2013, AJ, 146, 85
Hodgkin S. T., Irwin M. J., Hewett P. C., Warren S. J., 2009, MNRAS, 394, 675

Ingraham P., Albert L., Doyon R., Artigau E., 2014, ApJ, 782, 8
Jameson R. F., Casewell S. L., Bannister N. P., Lodieu N., Keresztes K., Dobbie P. D., Hodgkin S. T., 2008, MNRAS, 384, 1399
Kausch W. et al., 2015, A&A, 576, A78
Kirkpatrick J. D., Henry T. J., McCarthy D. W., 1991, ApJS, 77, 417
Kirkpatrick J. D. et al., 1999, ApJ, 519, 802
Kirkpatrick J. D., Barman T. S., Burgasser A. J., McGovern M. R., McLean I. S., Tinney C. G., Lowrance P. J., 2006, ApJ, 639, 1120
Knapp G. R. et al., 2004, AJ, 127, 3553
Köhler R., Kunkel M., Leinert C., Zinnecker H., 2000, A&A, 356, 541
Kraus A. L., Ireland M. J., Martinache F., Lloyd J. P., 2008, ApJ, 679, 762
Kraus A. L., Cody A. M., Covey K. R., Rizzuto A. C., Mann A. W., Ireland M. J., 2015, ApJ, 807, 3
Kroupa P., Weidner C., Pflamm-Altenburg J., Thies I., Dabringhausen J., Marks M., Maschberger T., 2013, in Oswalt T. D., Gilmore G., eds, Planets, Stars and Stellar Systems, Vol. 5, Galactic Structure and Stellar Populations. Springer Science+Business Media, Dordrecht, p. 115
Kunkel M., 1999, PhD thesis, Julius-Maximilians-Universität Würzburg
Lafrenière D., Jayawardhana R., van Kerkwijk M. H., 2008, ApJ, 689, L153
Lafrenière D., Jayawardhana R., van Kerkwijk M. H., 2010, ApJ, 719, 497
Lafrenière D., Jayawardhana R., Janson M., Helling C., Witte S., Hauschildt P., 2011, ApJ, 730, 42
Lafrenière D., Jayawardhana R., van Kerkwijk M. H., Brandeker A., Janson M., 2014, ApJ, 785, 47
Lawrence A. et al., 2007, MNRAS, 379, 1599
Lépine S., Shara M. M., 2005, AJ, 129, 1483
Lissauer J. J., Dawson R. I., Tremaine S., 2014, Nature, 513, 336
Liu M. C. et al., 2013, ApJ, 777, L20
Liu M. C., Dupuy T. J., Allers K. N., 2016, ApJ, 833, 96
Lodieu N., 2013, MNRAS, 431, 3222
Lodieu N., Hambly N. C., Jameson R. F., 2006, MNRAS, 373, 95
Lodieu N., Hambly N. C., Jameson R. F., Hodgkin S. T., Carraro G., Kendall T. R., 2007, MNRAS, 374, 372
Lodieu N., Hambly N. C., Jameson R. F., Hodgkin S. T., 2008, MNRAS, 383, 1385
Lodieu N., Zapatero Osorio M. R., Rebolo R., Martín E. L., Hambly N. C., 2009, A&A, 505, 1115
Lodieu N., Dobbie P. D., Hambly N. C., 2011a, A&A, 527, A24
Lodieu N., Hambly N. C., Dobbie P. D., Cross N. J. G., Christensen L., Martin E. L., Valdivielso L., 2011b, MNRAS, 418, 2604
Lodieu N., Dobbie P. D., Cross N. J. G., Hambly N. C., Read M. A., Blake R. P., Floyd D. J. E., 2013, MNRAS, 435, 2474
Lodieu N. et al., 2015, A&A, 584, A128
Low C., Lynden-Bell D., 1976, MNRAS, 176, 367
Lucas P. W., Roche P. F., 2000, MNRAS, 314, 858
Lucas P. W., Roche P. F., Allard F., Hauschildt P. H., 2001, MNRAS, 326, 695
Luhman K. L., 2004, ApJ, 602, 816
Luhman K. L., 2012, ARA&A, 50, 65
Luhman K. L., Mamajek E. E., 2012, ApJ, 758, 31
Luhman K. L., Rieke G. H., 1999, ApJ, 525, 440
Luhman K. L., Rieke G. H., Lada C. J., Lada E. A., 1998, ApJ, 508, 347
Luhman K. L., Briceño C., Stauffer J. R., Hartmann L., Barrado y Navascués D., Caldwell N., 2003a, ApJ, 590, 348
Luhman K. L., Stauffer J. R., Muench A. A., Rieke G. H., Lada E. A., Bouvier J., Lada C. J., 2003b, ApJ, 593, 1093
Luhman K. L., Allers K. N., Jaffe D. T., Cushing M. C., Williams K. A., Slesnick C. L., Vacca W. D., 2007, ApJ, 659, 1629
Luhman K. L., Hernández J., Downes J. J., Hartmann L., Briceño C., 2008, ApJ, 688, 362
Luhman K. L., Esplin T. L., Loutrel N. P., 2016, ApJ, 827, 52
Luhman K. L., Mamajek E. E., Shukla S. J., Loutrel N. P., 2017, AJ, 153, 46
Malo L., Artigau É., Doyon R., Lafrenière D., Albert L., Gagné J., 2014, ApJ, 788, 81
Manjavacas E. et al., 2014, A&A, 564, A55
Mann A. W. et al., 2016, AJ, 152, 61
Marsh K. A., Kirkpatrick J. D., Plavchan P., 2010a, ApJ, 709, L158
Marsh K. A., Plavchan P., Kirkpatrick J. D., Lowrance P. J., Cutri R. M., Velusamy T., 2010b, ApJ, 719, 550
Martín E. L., Zapatero Osorio M. R., 2003, ApJ, 593, L113
Martín E. L., Rebolo R., Zapatero Osorio M. R., 1996, ApJ, 469, 706
Martín E. L., Zapatero Osorio M. R., Barrado y Navascués D., Béjar V. J. S., Rebolo R., 2001a, ApJ, 558, L117
Martín E. L., Dougados C., Magnier E., Ménard F., Magazzù A., Cuillandre J.-C., Delfosse X., 2001b, ApJ, 561, L195
Martín E. L., Delfosse X., Guieu S., 2004, AJ, 127, 449
Martin E. C. et al., 2017, ApJ, 838, 73
McGovern M. R., Kirkpatrick J. D., McLean I. S., Burgasser A. J., Prato L., Lowrance P. J., 2004, ApJ, 600, 1020
McLean I. S. et al., 2000, ApJ, 533, L45
McLean I. S., McGovern M. R., Burgasser A. J., Kirkpatrick J. D., Prato L., Kim S. S., 2003, ApJ, 596, 561
McLean I. S., Prato L., McGovern M. R., Burgasser A. J., Kirkpatrick J. D., Rice E. L., Kim S. S., 2007, ApJ, 658, 1217
Mellier Y., 2016, in 41st COSPAR Scientific Assembly, abstracts from the meeting that was to be held 30 July–7 August at the Istanbul Congress Center (ICC), Turkey, but was cancelled. See http://cospar2016.tubitak.gov.tr/en/, Abstract H0.2-1-16. Vol. 41 of COSPAR Meeting, Euclid and the Dark Universe
Miller G. E., Scalo J. M., 1979, ApJS, 41, 513
Monet D. G. et al., 2003, AJ, 125, 984
Mužić K., Scholz A., Geers V., Jayawardhana R., Tamura M., 2012, ApJ, 744, 134
Mužić K., Scholz A., Geers V. C., Jayawardhana R., López Martí B., 2014, ApJ, 785, 159
Mužić K., Scholz A., Geers V. C., Jayawardhana R., 2015, ApJ, 810, 159
Ochsenbein F., Bauer P., Marcout J., 2000, A&AS, 143, 23
Pecaut M. J., 2016, in Kastner J. H., Stelzer B., Metchev S. A., eds, IAU Symp. Vol. 314, Anomalous Spectral Types and Intrinsic Colours of Young Stars, p. 85
Pecaut M. J., Mamajek E. E., Bubar E. J., 2012, ApJ, 746, 154
Peña Ramírez K., Zapatero Osorio M. R., Béjar V. J. S., Rebolo R., Bihain G., 2011, A&A, 532, A42
Peña Ramírez K., Béjar V. J. S., Zapatero Osorio M. R., Petr-Gotzens M. G., Martín E. L., 2012, ApJ, 754, 30
Peña Ramírez K., Zapatero Osorio M. R., Béjar V. J. S., 2015, A&A, 574, A118
Peña Ramírez K., Béjar V. J. S., Zapatero Osorio M. R., 2016, A&A, 586, A157
Preibisch T., Zinnecker H., 1999, AJ, 117, 2381
Preibisch T., Zinnecker H., 2002, AJ, 123, 1613
Preibisch T., Guenther E., Zinnecker H., Sterzik M., Frink S., Roeser S., 1998, A&A, 333, 619
Preibisch T., Guenther E., Zinnecker H., 2001, AJ, 121, 1040
Reed B. C., 2003, AJ, 125, 2531
Rees M. J., 1976, MNRAS, 176, 483
Reid I. N., Burgasser A. J., Cruz K. L., Kirkpatrick J. D., Gizis J. E., 2001, AJ, 121, 1710
Reid I. N., Cruz K. L., Kirkpatrick J. D., Allen P. R., Mungall F., Liebert J., Lowrance P., Sweet A., 2008, AJ, 136, 1290
Rizzuto A. C., Ireland M. J., Dupuy T. J., Kraus A. L., 2016, ApJ, 817, 164
Ruiz M. T., Leggett S. K., Allard F., 1997, ApJ, 491, L107
Salpeter E. E., 1955, ApJ, 121, 161
Scalo J. M., 1986, Fundamentals of Cosmic Physics, 11, 1
Schmidt S. J., West A. A., Hawley S. L., Pineda J. S., 2010, AJ, 139, 1808
Scholz A., Geers V., Jayawardhana R., Fissel L., Lee E., Lafreniere D., Tamura M., 2009, ApJ, 702, 805
Scholz A., Muzic K., Geers V., Bonavita M., Jayawardhana R., Tamura M., 2012a, ApJ, 744, 6
Scholz A., Jayawardhana R., Muzic K., Geers V., Tamura M., Tanaka I., 2012b, ApJ, 756, 24
Sion E. M., Holberg J. B., Oswalt T. D., McCook G. P., Wasatonic R., 2009, AJ, 138, 1681

Skrutskie M. F. et al., 2006, AJ, 131, 1163
Slesnick C. L., Hillenbrand L. A., Carpenter J. M., 2004, ApJ, 610, 1045
Slesnick C. L., Carpenter J. M., Hillenbrand L. A., 2006, AJ, 131, 3016
Slesnick C. L., Hillenbrand L. A., Carpenter J. M., 2008, ApJ, 688, 377
Smette A. et al., 2015, A&A, 576, A77
Song I., Zuckerman B., Bessell M. S., 2012, AJ, 144, 8
Spezzi L., Alves de Oliveira C., Moraux E., Bouvier J., Winston E., Hudelot P., Bouy H., Cuillandre J.-C., 2012, A&A, 545, A105
Stassun K. G., Mathieu R. D., Valenti J. A., 2006, Nature, 440, 311
Stassun K. G., Mathieu R. D., Valenti J. A., 2007, ApJ, 664, 1154
Stumpf M. B., Brandner W., Henning T., Bouy H., Koehler R., Hormuth F., Joergens V., Kasper M., 2008, A&A, preprint (arXiv:0811.0556)
Suenaga T., Tamura M., Kuzuhara M., Yanagisawa K., Ishii M., Lucas P. W., 2014, PASJ, 66, 33
Testi L. et al., 2001, ApJ, 552, L147
Todorov K., Luhman K. L., McLeod K. K., 2010, ApJ, 714, L84
Tody D., 1986, in Crawford D. L., ed., Proc. SPIE Conf. Ser. Vol. 627, Instrumentation in Astronomy VI. SPIE, Bellingham, p. 733
Tody D., 1993, in Hanisch R. J., Brissenden R. J. V., Barnes J., eds, Astronomical Data Analysis Software and Systems II, ASP Conf. Ser. Vol. 52, IRAF in the Nineties. Astron. Soc. Pac., San Francisco, p. 173
Tokunaga A. T., Kobayashi N., 1999, AJ, 117, 1010
Tokunaga A. T., Simons D. A., Vacca W. D., 2002, PASP, 114, 180
van Leeuwen F., 2007, A&A, 474, 653
Vernet J. et al., 2011, A&A, 536, A105
Vrba F. J. et al., 2004, AJ, 127, 2948
Walter F. M., Vrba F. J., Mathieu R. D., Brown A., Myers P. C., 1994, AJ, 107, 692
Weights D. J., Lucas P. W., Roche P. F., Pinfield D. J., Riddick F., 2009, MNRAS, 392, 817
Wesemael F., Greenstein J. L., Liebert J., Lamontagne R., Fontaine G., Bergeron P., Glaspey J. W., 1993, PASP, 105, 761
West A. A., Hawley S. L., Bochanski J. J., Covey K. R., Reid I. N., Dhital S., Hilton E. J., Masuda M., 2008, AJ, 135, 785
Wright E. L. et al., 2010, AJ, 140, 1868
Wu Y.-L. et al., 2015, ApJ, 807, L13
Zakhozhay O. V., Zapatero Osorio M. R., Béjar V. J. S., Boehler Y., 2017, MNRAS, 464, 1108
Zapatero Osorio M. R., Béjar V. J. S., Martín E. L., Rebolo R., Barrado y Navascués D., Bailer-Jones C. A. L., Mundt R., 2000, Science, 290, 103
Zapatero Osorio M. R., Béjar V. J. S., Martín E. L., Rebolo R., Barrado y Navascués D., Mundt R., Eislöffel J., Caballero J. A., 2002, ApJ, 578, 536
Zapatero Osorio M. R. et al., 2007, A&A, 472, L9
Zapatero Osorio M. R. et al., 2008, A&A, 477, 895
Zapatero Osorio M. R., Béjar V. J. S., Miles-Páez P. A., Peña Ramírez K., Rebolo R., Pallé E., 2014a, A&A, 568, A6
Zapatero Osorio M. R. et al., 2014b, A&A, 568, A77

SUPPORTING INFORMATION

Supplementary data are available at *MNRAS* online.

Please note: Oxford University Press is not responsible for the content or functionality of any supporting materials supplied by the authors. Any queries (other than missing material) should be directed to the corresponding author for the article.

APPENDIX A: NEAR-INFRARED SPECTRAL INDICES

We report the values of the spectral indices for all sources in Table A1 and plot them as a function of spectral type in Fig. A1, in which we plot the infrared spectral types of our UpSco sources and the spectral types published in the literature for comparison samples of old field, beta and gamma L dwarfs.

Table A1. Values of spectral indices defined in the literature by various authors and computed for field L dwarfs, young L dwarfs and our UpSco L-type objects. References for the definitions of the spectral indices are as follows: Reid et al. (2001), Tokunaga & Kobayashi (1999), Burgasser et al. (2006), (Geballe et al. 2002), Burgasser et al. (2002), Allers et al. (2007), McLean et al. (2003), Slesnick et al. (2004), Allers & Liu (2013) and (Testi et al. 2001).

#SpT	H2OA	H2OB	K1	K2	H2OJ	CH4J	H2OH	CH4H	H2OK	CH4K	H2O15	KJ	KH	YJ	HJ	H2Oc	Jcont	Hcont	FeHJ	FeHH	CO	H2OD2	H2O	H2OD	H2O1	H2O2	sHJ	sKJ	sH2OJ	sH2OH1	sH2OH2	sH2OK	VOz	Target
10.0	0.705	0.827	−0.885	0.043	0.961	0.909	0.855	1.110	0.969	1.103	1.194	0.366	0.590	0.768	0.670	1.544	1.068	1.007	0.942	0.908	0.775	0.883	1.122	1.073	0.684	0.887	0.368	0.894	0.060	0.257	0.376	0.033	1.130	
10.0	0.724	0.768	−0.670	0.014	0.896	0.910	0.823	1.091	0.925	1.079	1.269	0.475	0.643	0.631	0.793	1.433	1.176	0.972	0.967	0.923	0.771	0.877	1.159	1.000	0.700	0.887	0.232	0.680	0.154	0.304	0.325	0.119	1.135	
14.0	0.770	0.819	−0.553	−0.026	0.885	0.951	0.864	1.029	0.881	1.040	1.228	0.539	0.702	0.581	0.810	1.432	1.198	0.927	1.033	0.959	0.721	0.808	1.180	0.932	0.744	0.841	0.242	0.550	0.181	0.221	0.308	0.192	1.015	
12.0	0.655	0.700	−0.604	0.015	0.860	0.896	0.775	1.112	0.876	1.091	1.422	0.492	0.667	0.608	0.813	1.612	1.230	0.944	0.987	0.918	0.756	0.786	1.236	0.962	0.619	0.819	0.191	0.608	0.197	0.428	0.406	0.197	1.193	
10.0	0.707	0.760	−0.666	0.015	0.877	0.949	0.812	1.112	0.919	1.085	1.274	0.470	0.626	0.664	0.803	1.606	1.182	0.964	0.977	0.913	0.770	0.806	1.147	1.011	0.690	0.873	0.212	0.677	0.167	0.350	0.383	0.130	1.210	
10.0	0.679	0.776	−0.616	0.038	0.857	0.933	0.798	1.101	0.937	1.097	1.311	0.505	0.673	0.614	0.808	1.403	1.291	0.971	1.009	0.931	0.764	0.856	1.263	0.998	0.654	0.849	0.224	0.642	0.230	0.338	0.303	0.111	1.153	
10.0	0.733	0.829	−0.805	−0.019	0.956	0.921	0.874	1.010	0.885	1.036	1.202	0.407	0.563	0.864	0.760	1.553	0.881	0.918	0.792	0.976	0.743	0.861	1.154	1.007	0.696	0.885	0.288	0.802	−0.112	0.182	0.391	0.131	1.082	
15.0	0.680	0.648	0.165	0.020	0.627	0.915	0.741	1.184	0.872	1.082	1.520	1.102	0.951	0.425	1.290	1.458	1.764	0.973	1.278	0.884	0.843	0.783	1.255	0.889	0.660	0.848	−0.260	−0.152	0.536	0.564	0.289	0.220	1.036	
13.5	0.700	0.699	−0.406	−0.022	0.792	0.882	0.769	1.073	0.806	1.038	1.471	0.614	0.713	0.508	0.942	1.589	1.354	0.879	1.070	0.932	0.727	0.748	1.319	0.853	0.647	0.812	0.087	0.407	0.298	0.431	0.394	0.288	1.029	
9.5	0.698	0.799	−0.863	0.027	0.959	0.902	0.847	1.086	0.935	1.096	1.234	0.371	0.584	0.814	0.683	1.538	1.034	0.974	0.927	0.936	0.771	0.859	1.135	1.048	0.665	0.876	0.348	0.868	0.027	0.267	0.392	0.097	1.125	
14.0	0.675	0.627	−0.349	0.010	0.721	0.866	0.709	1.182	0.886	1.086	1.513	0.646	0.764	0.470	0.951	1.540	1.488	0.960	1.102	0.872	0.792	0.765	1.296	0.935	0.645	0.830	0.036	0.359	0.390	0.564	0.363	0.210	1.090	
11.0	0.730	0.701	−0.549	0.029	0.843	0.915	0.751	1.147	0.908	1.109	1.390	0.522	0.674	0.578	0.856	1.546	1.297	0.970	1.014	0.892	0.770	0.795	1.235	0.991	0.697	0.819	0.128	0.562	0.242	0.441	0.371	0.161	1.184	
12.0	0.666	0.677	−0.313	0.051	0.742	0.911	0.748	1.214	0.882	1.135	1.468	0.669	0.778	0.478	0.984	1.485	1.508	0.999	1.085	0.859	0.773	0.753	1.268	0.949	0.629	0.822	0.019	0.327	0.400	0.535	0.331	0.202	1.237	
11.0	0.658	0.719	−0.702	0.000	0.882	0.885	0.780	1.073	0.856	1.076	1.400	0.448	0.618	0.595	0.789	1.649	1.207	0.913	0.998	0.937	0.737	0.794	1.250	0.951	0.630	0.825	0.231	0.696	0.176	0.382	0.435	0.210	1.117	
11.0	0.690	0.767	−0.743	0.009	0.909	0.905	0.819	1.047	0.857	1.090	1.316	0.423	0.606	0.619	0.766	1.589	1.166	0.919	0.946	0.955	0.718	0.781	1.196	0.973	0.639	0.824	0.281	0.750	0.140	0.310	0.416	0.195	1.113	
11.0	0.718	0.790	−0.786	−0.022	0.912	0.899	0.833	1.037	0.833	1.048	1.276	0.414	0.590	0.582	0.750	1.635	1.053	0.905	0.943	0.957	0.716	0.834	1.209	0.958	0.683	0.832	0.289	0.762	0.072	0.276	0.427	0.208	1.083	
14.0	0.666	0.616	−0.253	0.059	0.744	0.888	0.697	1.222	0.827	1.159	1.466	0.683	0.802	0.506	0.998	1.643	1.566	0.990	1.137	0.845	0.757	0.713	1.385	0.871	0.587	0.814	−0.007	0.276	0.427	0.535	0.383	0.307	1.184	
10.0	0.715	0.759	−0.693	0.026	0.899	0.922	0.818	1.126	0.921	1.090	1.299	0.459	0.638	0.634	0.778	1.516	1.171	0.978	0.977	0.909	0.770	0.835	1.186	1.005	0.694	0.867	0.232	0.702	0.153	0.354	0.371	0.120	1.145	
14.0	0.674	0.666	0.110	0.019	0.639	0.838	0.726	1.213	0.864	1.085	1.525	1.031	0.952	0.433	1.223	1.398	1.722	0.977	1.276	0.863	0.830	0.772	1.319	0.890	0.644	0.839	−0.222	−0.106	0.523	0.602	0.280	0.233	1.032	
10.5	0.792	0.867	−0.775	−0.009	0.997	0.938	0.910	1.009	0.916	1.033	1.157	0.429	0.580	0.730	0.762	1.451	1.066	0.937	0.952	0.970	0.734	0.881	1.108	1.004	0.740	0.881	0.291	0.780	0.055	0.139	0.328	0.085	1.097	
13.0	0.669	0.651	−0.380	0.012	0.794	0.883	0.742	1.145	0.854	1.099	1.495	0.609	0.729	0.514	0.942	1.641	1.417	0.939	1.099	0.881	0.758	0.715	1.303	0.893	0.616	0.781	0.053	0.388	0.336	0.500	0.391	0.263	1.159	
10.0	0.746	0.853	−0.856	−0.008	0.950	0.907	0.887	1.021	0.905	1.040	1.169	0.390	0.575	0.701	0.710	1.497	1.047	0.934	0.941	0.966	0.743	0.911	1.122	1.009	0.735	0.899	0.354	0.852	0.049	0.164	0.364	0.106	1.050	
11.5	0.663	0.719	−0.691	−0.012	0.873	0.893	0.785	1.058	0.835	1.059	1.391	0.455	0.605	0.591	0.819	1.678	1.176	0.897	0.943	0.951	0.728	0.771	1.251	0.947	0.634	0.825	0.205	0.684	0.144	0.369	0.453	0.220	1.082	
13.0	0.644	0.650	−0.477	0.038	0.764	0.899	0.752	1.209	0.868	1.121	1.492	0.555	0.729	0.506	0.877	1.657	1.460	0.994	1.064	0.866	0.776	0.763	1.282	0.924	0.618	0.817	0.129	0.497	0.356	0.528	0.399	0.219	1.193	
10.0	0.782	0.730	−0.574	0.023	0.870	0.988	0.795	1.152	0.949	1.089	1.309	0.516	0.668	0.622	0.832	1.467	1.215	0.992	0.986	0.897	0.774	0.858	1.177	0.996	0.749	0.879	0.152	0.595	0.186	0.397	0.324	0.106	1.181	
10.0	0.600	0.733	−0.882	0.012	0.882	0.847	0.789	1.089	0.848	1.100	1.362	0.355	0.557	0.655	0.705	1.803	1.178	0.930	0.994	0.930	0.702	0.745	1.230	0.937	0.555	0.802	0.334	0.875	0.151	0.371	0.526	0.233	1.093	
12.5	0.758	0.820	−0.842	−0.032	0.928	0.895	0.849	1.008	0.851	1.019	1.259	0.385	0.557	0.632	0.735	1.568	1.076	0.898	0.935	0.974	0.702	0.830	1.168	0.948	0.742	0.855	0.341	0.844	0.082	0.235	0.401	0.189	1.044	
14.0	0.677	0.736	−0.481	0.053	0.758	1.003	0.715	1.184	0.863	1.138	nan	0.548	0.707	nan	0.845	nan	nan	1.042	nan	0.882	0.786	0.757	1.295	0.820	0.611	0.828	0.119	0.523	nan	nan	0.337	0.295	−nan	
17.0	0.726	0.598	0.528	−0.020	0.604	0.921	0.680	1.196	0.764	1.026	1.681	1.586	1.107	0.423	1.513	1.415	1.871	0.937	1.481	0.878	0.834	0.726	1.353	0.753	0.684	0.832	−0.452	−0.506	0.616	0.676	0.265	0.362	0.962	
17.0	0.618	0.519	0.633	−0.043	0.559	0.843	0.643	1.243	0.728	1.015	1.864	1.748	1.133	0.516	1.627	1.511	1.864	0.934	1.481	0.861	0.777	0.680	1.488	0.738	0.576	0.769	−0.562	−0.644	0.586	0.753	0.273	0.399	0.995	
13.0	0.607	0.615	−0.262	0.045	0.682	0.852	0.717	1.251	0.826	1.144	1.604	0.693	0.818	0.423	0.994	1.624	1.604	1.001	1.129	0.847	0.768	0.711	1.321	0.905	0.575	0.775	−0.011	0.268	0.459	0.650	0.400	0.270	1.195	
10.0	0.662	0.761	−0.629	0.015	0.801	0.932	0.825	1.112	0.933	1.084	1.294	0.476	0.660	nan	0.807	1.560	1.484	0.942	1.060	0.919	0.799	0.825	1.202	0.911	0.626	0.825	0.231	0.655	0.364	0.420	0.374	0.126	−nan	
10.0	0.630	0.797	−0.773	−0.014	0.940	0.861	0.855	0.998	0.868	1.051	1.234	0.413	0.609	nan	0.733	1.429	1.013	0.892	0.874	0.969	0.739	0.761	1.104	0.876	0.641	0.849	0.338	0.770	0.011	0.267	0.338	0.183	−nan	
8.5	0.704	0.832	−0.970	0.019	0.952	0.871	0.881	1.087	0.991	1.063	1.149	0.332	0.571	nan	0.618	1.502	1.071	0.965	0.976	0.935	0.814	0.929	1.110	0.985	0.673	0.931	0.447	0.975	0.051	0.283	0.375	0.022	−nan	
10.0	0.674	0.683	−0.460	0.042	0.719	0.934	0.778	1.196	0.939	1.124	1.340	0.564	0.699	nan	0.910	1.461	1.574	0.982	1.163	0.860	0.783	0.792	1.223	0.924	0.625	0.840	0.078	0.494	0.422	0.533	0.315	0.141	−nan	
9.2	0.685	0.785	−0.802	0.033	0.860	0.911	0.854	1.133	0.973	1.093	1.240	0.406	0.561	nan	0.781	1.596	1.156	0.904	0.956	0.918	0.768	0.868	1.141	0.985	0.653	0.909	0.233	0.818	0.124	0.523	0.423	0.041	−nan	
14.0	0.528	0.621	−0.459	−0.015	0.721	0.852	0.730	1.106	0.743	1.072	1.566	0.561	0.701	nan	0.895	1.861	1.562	0.856	1.204	0.893	0.724	0.616	1.326	0.714	0.519	0.765	0.136	0.458	0.444	0.607	0.509	0.409	−nan	
0.0	0.509	0.371	0.892	0.076	0.511	0.844	0.494	1.359	0.669	1.207	2.587	2.198	1.755	nan	1.520	1.771	2.533	0.964	1.708	0.844	0.942	0.566	1.720	0.611	0.496	0.673	−0.490	−0.881	0.840	1.144	0.384	0.552	−nan	
9.5	0.611	0.659	−0.557	0.103	0.797	0.881	0.753	1.257	0.935	1.203	1.400	0.511	0.739	nan	0.806	1.874	1.365	1.021	0.996	0.853	0.817	0.834	1.198	0.943	0.562	0.830	0.183	0.594	0.277	0.606	0.446	0.134	−nan	
9.5	0.656	0.683	−0.552	0.086	0.770	0.898	0.795	1.211	0.929	1.172	1.360	0.526	0.733	nan	0.817	1.517	1.473	0.989	1.071	0.857	0.810	0.801	1.179	0.917	0.623	0.864	0.194	0.577	0.333	0.545	0.335	0.139	−nan	
9.5	0.649	0.706	−0.706	0.049	1.024	0.909	0.797	1.155	0.909	1.127	1.361	0.434	0.651	nan	0.716	1.605	1.086	0.945	0.925	0.901	0.803	0.780	1.210	0.903	0.595	0.828	0.267	0.731	0.010	0.505	0.407	0.151	−nan	
14.0	0.650	0.623	−0.167	0.014	0.691	0.933	0.694	1.162	0.793	1.113	1.635	0.752	0.822	0.437	1.030	1.699	1.547	0.943	1.149	0.881	0.745	0.693	1.384	0.840	0.608	0.779	−0.032	0.195	0.420	0.604	0.421	0.351	1.000	
14.0	0.592	0.620	−0.389	−0.012	0.741	0.826	0.706	1.129	0.850	1.076	1.561	0.606	0.749	0.449	0.920	1.613	1.450	0.930	1.088	0.910	0.749	0.753	1.330	0.851	0.578	0.789	0.080	0.382	0.358	0.549	0.408	0.315	1.116	
9.0	0.708	0.817	−0.929	0.005	0.975	0.885	0.866	1.053	0.933	1.069	1.216	0.344	0.535	0.826	0.682	1.547	1.016	0.954	0.936	0.968	0.760	0.870	1.127	0.922	0.684	0.890	0.353	0.926	0.007	0.237	0.396	0.146	1.056	
11.0	0.756	0.803	−0.669	0.002	0.905	0.946	0.835	1.055	nan	1.073	1.240	0.468	0.593	0.640	0.846	nan	1.150	0.940	0.970	0.953	0.755	0.841	1.192	nan	0.700	0.861	0.167	0.671	0.125	0.255	0.307	nan	1.108	
13.0	0.635	0.638	−0.366	0.015	0.786	0.890	0.735	1.138	0.809	1.093	1.512	0.642	0.749	0.549	0.949	1.628	1.404	0.928	1.029	0.904	0.736	0.748	1.304	0.795	0.575	0.817	0.058	0.392	0.313	0.525	0.386	0.293	1.135	
13.0	0.619	0.622	−0.486	0.019	0.786	0.872	0.737	1.147	nan	1.110	1.501	0.558	0.703	0.544	0.896	nan	1.423	0.942	1.069	0.894	0.746	nan	1.283	nan	0.582	0.794	0.110	0.497	0.349	0.505	0.352	nan	1.230	
9.0	0.695	0.791	−0.829	0.043	0.946	0.901	0.840	1.080	0.933	1.112	1.242	0.388	0.609	0.781	0.690	1.595	1.065	0.966	0.945	0.941	0.776	0.879	1.150	1.043	0.667	0.874	0.345	0.836	0.058	0.273	0.405	0.095	1.112	
14.0	0.597	0.610	−0.227	0.020	0.663	0.867	0.697	1.187	0.846	1.106	1.602	0.728	0.823	0.438	1.020	1.674	1.640	0.954	1.142	0.872	0.796	0.747	1.353	0.899	0.572	0.786	−0.019	0.232	0.473	0.610	0.410	0.265	1.128	
12.0	0.652	0.728	−0.503	0.077	0.654	0.984	0.740	1.176	nan	1.156	1.387	0.554	0.686	0.400	0.907	nan	2.000	0.954	1.217	0.882	0.790	0.640	1.391	nan	0.603	0.804	0.131	0.572	0.597	0.463	0.417	nan	1.279	
15.0	0.650	0.623	−0.167	0.014	0.691	0.933	0.694	1.162	0.793	1.113	1.635	0.752	0.822	0.437	1.030	1.699	1.547	0.943	1.149	0.881	0.745	0.693	1.384	0.840	0.608	0.779	−0.032	0.195	0.420	0.604	0.421	0.351	1.000	
11.0	0.724	0.709	−0.606	−0.011	0.811	0.950	0.758	1.140	nan	1.081	1.362	0.490	0.644	0.468	0.830	nan	1.517	0.952	1.182	0.905	0.738	nan	1.307	nan	0.675	0.777	0.161	0.606	0.369	0.411	0.284	nan	1.005	
11.0	0.654	0.722	−0.793	0.064	0.830	0.889	0.797	1.161	0.945	1.122	1.393	0.429	0.597	0.659	0.768	1.740	1.290	1.003	1.055	0.925	0.765	0.906	1.149	1.101	0.628	0.923	0.198	0.790	0.223	0.472	0.421	0.006	1.377	
11.0	0.683	0.684	−0.501	0.015	0.850	0.895	0.757	1.170	nan	1.113	nan	0.549	0.701	0.538	0.896	nan	1.218	0.987	0.958	0.887	0.730	nan	1.224	nan	0.653	0.804	0.083	0.483	0.182	nan	0.335	nan	1.198	
10.0	0.687	0.733	−0.349	−0.003	0.840	0.901	0.797	1.111	nan	nan	nan	nan	0.703	0.729	1.046	nan	1.247	0.963	1.024	0.923	nan	nan	1.202	nan	0.657	nan	−0.060	0.378	0.210	nan	nan	nan	1.199	
11.0	0.668	0.706	−0.713	−0.067	0.834	0.883	0.768	1.100	nan	1.008	1.381	0.460	0.604	0.540	0.796	nan	1.252	0.952	1.013	0.923	0.728	nan	1.219	nan	0.603	0.819	0.199	0.704	0.215	0.383	0.380	nan	1.094	

MNRAS 473, 2020–2059 (2018)

Table A1. – *continued.*

#SpT	H2OA	H2OB	K1	K2	H2OJ	CH4J	H2OH	CH4H	H2OK	CH4K	H2O15	KJ	KH	YJ	HJ	H2Oc	Jcont	Hcont	FeHJ	FeHH	CO	H2OD2	H2O	H2OD	H2O1	H2O2	sHJ	sKJ	sH2OJ	sH2OH1	sH2OH2	sH2OK	VOz	Target
10.0	0.679	0.750	−0.812	0.049	0.932	0.907	0.811	1.118	0.950	1.126	1.305	0.393	0.562	0.809	0.758	1.538	1.086	0.981	0.951	0.926	0.785	0.874	1.182	0.944	0.629	0.866	0.225	0.821	0.076	0.356	0.383	0.136	1.171	
10.0	0.717	0.701	−0.679	0.066	0.943	0.916	0.769	1.096	nan	1.166	1.389	0.449	0.667	0.670	0.756	nan	1.087	0.945	0.950	0.917	0.807	0.888	1.182	nan	0.674	0.844	0.230	0.673	0.091	0.387	0.296	nan	1.215	
11.0	0.638	0.683	−0.604	0.030	0.857	0.859	0.756	1.125	nan	1.107	1.395	0.498	0.710	0.581	0.797	nan	1.230	0.951	0.975	0.900	0.741	nan	1.226	nan	0.600	0.824	0.210	0.597	0.199	0.421	0.330	nan	1.182	
13.0	0.628	0.665	−0.447	0.005	0.785	0.864	0.747	1.107	nan	1.111	1.451	0.573	0.722	0.564	0.912	nan	1.275	0.918	1.003	0.925	0.820	nan	1.301	nan	0.601	0.776	0.098	0.450	0.232	0.451	0.393	nan	1.119	
10.0	0.708	0.760	−0.630	0.057	0.970	0.924	0.821	1.143	nan	1.148	1.262	0.493	0.671	0.716	0.817	1.434	1.065	1.026	0.891	0.868	0.783	nan	1.090	nan	0.687	0.880	0.180	0.631	0.040	0.331	0.314	nan	1.209	
11.0	0.763	0.926	−0.582	−0.005	0.857	0.944	0.823	1.125	0.898	1.077	1.189	0.492	0.651	0.588	0.823	1.456	1.274	1.070	1.095	0.897	0.737	0.691	1.090	1.024	0.714	0.776	0.161	0.573	0.210	0.244	0.412	0.234	1.050	
11.0	0.634	0.721	−0.759	0.035	0.861	0.836	0.807	1.172	0.939	1.112	1.321	0.422	0.615	0.657	0.756	1.666	1.254	0.998	1.023	0.895	0.773	0.789	1.192	1.054	0.603	0.828	0.253	0.782	0.232	0.402	0.445	0.050	1.192	
13.0	0.577	0.678	−0.174	0.019	0.806	0.850	0.726	1.134	nan	1.205	1.502	0.675	0.815	0.491	1.023	nan	1.497	0.911	1.012	0.895	0.743	0.622	1.396	nan	0.548	0.769	0.004	0.217	0.324	0.500	0.333	nan	0.940	
11.0	0.728	0.691	−0.504	0.025	0.772	0.924	0.758	1.165	nan	1.111	1.390	0.555	0.710	0.557	0.877	nan	1.358	0.993	1.039	0.891	0.757	nan	1.204	nan	0.675	0.789	0.121	0.510	0.312	0.449	0.321	nan	1.265	
13.0	0.669	0.627	−0.346	−0.003	0.762	0.918	0.722	1.174	nan	1.073	1.518	0.636	0.759	0.523	0.944	nan	1.418	0.979	1.020	0.886	0.754	nan	1.270	nan	0.615	0.785	0.049	0.372	0.328	0.546	0.320	nan	1.219	
10.0	0.615	0.699	−0.618	0.007	0.860	0.869	0.789	1.132	0.924	1.061	1.350	0.497	0.673	0.596	0.804	1.316	1.235	0.966	1.010	0.907	0.798	0.972	1.221	0.996	0.604	0.845	0.195	0.615	0.213	0.407	0.272	0.176	1.194	
14.0	0.697	0.666	−0.319	0.015	0.744	0.887	0.731	1.151	0.851	1.100	1.469	0.666	0.767	0.468	0.986	1.563	1.433	0.959	1.059	0.882	0.748	0.754	1.265	0.940	0.674	0.791	0.017	0.328	0.348	0.525	0.360	0.221	1.073	
11.5	0.656	0.679	−0.282	0.063	0.832	0.934	0.766	1.153	nan	1.151	1.410	0.687	0.756	0.560	1.000	nan	1.338	0.966	1.020	0.891	0.792	nan	1.214	nan	0.615	0.857	−0.015	0.330	0.277	0.450	0.278	nan	1.225	
11.0	0.712	0.687	−0.529	−0.018	0.817	0.900	0.757	1.129	nan	1.059	1.423	0.531	0.682	0.569	0.868	nan	1.293	0.964	0.991	0.906	0.717	nan	1.244	nan	0.650	0.838	0.121	0.518	0.242	0.438	0.301	nan	1.218	
10.5	0.676	0.796	−0.842	−0.023	0.911	0.883	0.836	1.011	0.852	1.042	1.275	0.384	0.565	0.646	0.728	0.000	1.108	0.893	0.953	0.979	0.728	0.792	1.193	0.958	0.642	0.852	0.337	0.836	0.100	0.244	−2.000	0.189	1.059	
11.0	0.727	0.789	−0.692	−0.016	0.931	0.926	0.832	1.023	0.834	1.053	1.265	0.458	0.612	0.657	0.806	1.509	1.103	0.903	0.886	0.965	0.724	0.780	1.200	0.946	0.678	0.821	0.257	0.694	0.087	0.252	0.365	0.222	1.071	
11.0	0.616	0.737	−0.881	−0.019	0.878	0.848	0.799	1.040	0.824	1.059	1.369	0.360	0.560	0.638	0.703	0.000	1.142	0.893	0.957	0.961	0.715	0.758	1.236	0.944	0.591	0.813	0.364	0.873	0.130	0.330	−2.000	0.236	1.057	
12.0	0.642	0.698	−0.617	−0.020	0.829	0.870	0.765	1.059	0.819	1.061	1.438	0.488	0.647	0.527	0.834	0.000	1.263	0.891	0.999	0.945	0.727	0.740	1.283	0.904	0.611	0.798	0.200	0.609	0.226	0.404	−2.000	0.267	1.078	
13.0	0.643	0.706	−0.639	−0.042	0.838	0.883	0.767	1.041	0.805	1.019	1.446	0.489	0.631	0.505	0.837	0.000	1.260	0.874	0.985	0.952	0.735	0.746	1.289	0.900	0.601	0.820	0.208	0.627	0.218	0.394	−2.000	0.261	1.062	
13.0	0.609	0.691	−0.603	−0.012	0.803	0.873	0.756	1.076	0.794	1.065	1.484	0.496	0.656	0.479	0.836	0.000	1.359	0.892	1.046	0.929	0.723	0.709	1.305	0.881	0.573	0.787	0.197	0.600	0.289	0.443	−2.000	0.301	1.040	
13.5	0.579	0.673	−0.755	−0.056	0.802	0.834	0.745	1.045	0.774	1.004	1.528	0.429	0.590	0.507	0.783	1.866	1.260	0.860	0.988	0.956	0.742	0.727	1.326	0.859	0.537	0.808	0.269	0.745	0.227	0.448	0.560	0.305	1.032	
14.5	0.000	0.702	−0.231	−0.030	0.746	0.936	0.759	1.054	0.770	1.044	1.451	0.731	0.756	0.436	1.047	0.000	1.485	0.875	1.130	0.950	0.673	0.724	1.304	0.854	0.658	0.784	−0.020	0.235	0.371	0.417	−2.000	0.325	0.998	
14.0	0.598	0.686	−0.595	−0.033	0.817	0.840	0.758	1.049	0.732	1.046	1.461	0.498	0.715	0.464	0.761	1.661	1.284	0.876	1.050	0.947	nan	0.677	1.345	0.838	0.562	0.756	0.285	0.575	0.239	0.412	0.434	0.375	1.029	
15.0	0.540	0.644	−0.685	−0.088	0.767	0.825	0.721	1.032	0.727	0.953	1.623	0.475	0.599	0.499	0.823	0.000	1.333	0.828	1.059	0.966	0.719	0.711	1.376	0.751	0.498	0.813	0.216	0.674	0.289	0.499	−2.000	0.368	0.998	
15.0	0.518	0.639	−0.726	−0.101	0.770	0.813	0.707	1.029	0.718	0.938	1.651	0.452	0.574	0.489	0.807	0.000	1.363	0.821	1.090	0.973	0.719	0.690	1.395	0.743	0.489	0.821	0.224	0.715	0.294	0.514	−2.000	0.377	0.997	
16.0	0.545	0.638	−0.559	−0.112	0.745	0.830	0.711	1.020	0.714	0.915	1.635	0.555	0.638	0.542	0.872	1.940	1.373	0.828	1.121	0.993	0.760	0.725	1.366	0.731	0.502	0.864	0.133	0.549	0.303	0.501	0.618	0.375	0.982	
17.5	0.600	0.629	−0.227	−0.098	0.715	0.873	0.719	1.062	0.731	0.924	1.607	0.778	0.748	0.572	1.030	0.000	1.467	0.867	1.236	0.971	0.745	0.728	1.321	0.731	0.553	0.855	−0.055	0.224	0.374	0.533	−2.000	0.352	0.964	
17.0	0.440	0.563	−0.750	−0.142	0.720	0.758	0.689	1.034	0.670	0.887	1.806	0.446	0.582	0.580	0.753	2.156	1.418	0.803	1.205	0.988	nan	0.671	1.410	0.668	0.406	0.835	0.257	0.735	0.344	0.621	0.702	0.449	0.975	
18.0	0.516	0.594	−0.502	−0.172	0.695	0.811	0.684	1.007	0.686	0.848	1.715	0.602	0.637	0.572	0.906	1.973	1.501	0.811	1.252	1.023	0.729	0.746	1.408	0.683	0.451	0.884	0.083	0.494	0.393	0.547	0.636	0.393	0.963	
10.0	0.719	0.810	−0.800	−0.029	0.951	0.902	0.867	1.003	0.927	1.022	1.209	0.416	0.607	0.678	0.721	1.442	1.077	0.912	0.941	0.989	0.787	0.942	1.155	1.049	0.682	0.906	0.350	0.792	0.069	0.187	0.345	0.091	1.089	
13.5	0.571	0.659	−0.768	−0.083	0.779	0.831	0.730	1.037	0.800	0.977	1.562	0.422	0.573	0.388	0.774	1.864	1.348	0.853	1.086	0.951	0.690	0.741	1.327	0.853	0.518	0.825	0.273	0.759	0.292	0.459	0.539	0.281	1.056	
10.5	0.680	0.790	−0.918	−0.084	0.894	0.886	0.835	1.013	0.898	0.966	1.285	0.359	0.535	0.553	0.693	1.596	1.143	0.898	0.968	0.965	0.674	0.873	1.176	0.986	0.649	0.890	0.392	0.913	0.131	0.244	0.405	0.127	1.071	
12.0	0.717	0.790	−0.547	0.026	0.983	0.904	0.826	1.021	0.779	1.124	1.256	0.520	0.694	0.549	0.809	1.429	1.128	0.912	1.068	0.954	0.739	0.721	1.180	0.883	0.659	0.773	0.220	0.543	0.113	0.253	0.269	0.322	1.045	
12.5	0.644	0.722	−0.212	−0.034	nan	0.851	0.783	1.085	0.738	1.036	1.391	0.761	0.840	0.499	0.982	1.510	nan	0.926	nan	0.919	0.688	0.739	1.227	0.871	0.634	0.755	0.061	0.207	nan	0.403	0.298	0.322	−nan	
11.0	0.675	0.795	−0.860	−0.083	0.894	0.876	0.835	1.015	0.845	0.966	1.276	0.385	0.579	0.552	0.690	1.588	1.145	0.901	0.968	0.964	0.678	0.877	1.180	0.923	0.645	0.887	0.397	0.854	0.134	0.239	0.404	0.194	1.067	
13.0	0.686	0.671	−0.107	−0.020	0.690	0.901	0.705	1.088	0.748	1.058	1.462	0.814	0.851	0.421	1.055	1.731	1.440	0.886	1.075	0.911	0.712	0.684	1.537	0.791	0.604	0.742	−0.029	0.123	0.365	0.429	0.464	0.368	1.023	
14.0	0.571	0.657	−0.768	−0.082	0.784	0.833	0.727	1.035	0.801	0.978	1.563	0.423	0.575	0.387	0.771	1.868	1.343	0.853	1.086	0.953	0.689	0.740	1.321	0.851	0.524	0.824	0.275	0.760	0.292	0.458	0.538	0.282	1.045	
14.5	0.605	0.647	−0.473	−0.031	0.806	0.873	0.735	1.029	0.722	1.044	1.646	0.563	0.702	0.526	0.872	1.890	1.328	0.821	1.058	0.949	0.685	0.648	1.379	0.747	0.566	0.750	0.170	0.466	0.271	0.508	0.527	0.428	1.037	
14.0	0.581	0.734	−0.425	0.018	0.807	0.913	0.846	1.041	0.757	1.031	1.495	0.603	0.714	0.506	0.939	1.914	1.423	0.897	1.128	0.993	0.796	0.678	1.333	0.910	0.514	0.802	0.091	0.455	0.354	0.417	0.562	0.200	1.000	
15.5	0.571	0.666	−0.629	−0.070	0.798	0.794	0.735	1.022	0.721	0.976	1.605	0.493	0.641	0.526	0.808	1.875	1.300	0.832	1.069	0.959	0.722	0.675	1.350	0.757	0.506	0.805	0.230	0.615	0.256	0.470	0.558	0.394	1.018	
15.5	0.546	0.579	−0.589	−0.154	0.748	0.842	0.680	1.027	0.680	0.875	1.523	0.531	0.625	0.630	0.839	2.139	1.298	0.826	1.085	1.002	0.688	0.696	1.403	0.649	0.507	0.846	0.170	0.585	0.256	0.471	0.683	0.452	0.976	
15.5	0.659	0.657	−0.030	−0.064	0.689	0.837	0.728	1.061	0.770	0.980	1.609	0.914	0.841	0.596	1.154	1.511	1.532	0.879	1.281	0.972	0.772	0.736	1.257	0.808	0.598	0.829	−0.156	0.021	0.418	0.540	0.388	0.310	0.981	
15.5	0.737	0.606	−0.024	−0.050	0.752	0.926	0.715	1.082	0.765	0.996	1.641	0.897	0.818	0.623	1.143	1.641	1.371	0.879	1.179	0.937	0.768	0.712	1.381	0.794	0.632	0.804	−0.177	0.025	0.307	0.554	0.443	0.336	1.043	
15.0	0.528	0.649	−0.633	−0.096	0.803	0.800	0.723	1.018	0.728	0.938	1.572	0.502	0.617	0.493	0.846	1.955	1.250	0.841	1.018	0.979	0.726	0.713	1.324	0.746	0.487	0.819	0.189	0.616	0.219	0.473	0.583	0.376	0.973	
15.0	0.600	0.663	−0.361	−0.050	0.836	0.858	0.734	1.057	0.740	1.003	1.553	0.641	0.705	0.620	0.969	1.816	1.325	0.873	1.081	0.928	0.703	0.694	1.320	0.791	0.580	0.777	0.037	0.352	0.281	0.469	0.508	0.373	1.080	
16.0	0.619	0.645	−0.168	−0.083	0.752	0.848	0.723	1.044	0.710	0.951	1.640	0.806	0.774	0.542	1.057	1.578	1.278	0.852	1.108	0.982	0.757	0.695	1.358	0.713	0.581	0.826	−0.083	0.155	0.251	0.531	0.422	0.396	0.989	
16.5	0.597	0.726	−0.150	−0.098	0.715	0.918	0.714	1.142	0.687	0.937	1.665	0.805	0.725	0.635	1.084	1.963	1.507	0.901	1.307	0.897	0.753	0.674	1.515	0.747	0.600	0.770	−0.153	0.158	0.398	0.552	0.561	0.410	1.017	
16.5	0.593	0.620	−0.610	−0.090	0.759	0.807	0.712	1.017	0.725	0.905	1.654	0.543	0.616	0.630	0.872	2.015	1.288	0.823	1.102	1.001	0.714	0.756	1.322	0.699	0.504	0.886	0.131	0.596	0.252	0.527	0.645	0.348	0.985	
16.0	0.539	0.554	−0.537	−0.080	0.751	0.819	0.651	1.029	0.741	0.979	1.844	0.542	0.645	0.478	0.893	1.911	1.364	0.785	1.070	0.973	0.711	0.688	1.382	0.778	0.511	0.795	0.136	0.528	0.304	0.635	0.581	0.374	1.012	
17.5	0.640	0.605	−0.228	−0.131	0.708	0.857	0.700	1.044	0.710	0.896	1.673	0.762	0.744	0.561	1.019	1.769	1.451	0.838	1.230	0.980	0.723	0.725	1.369	0.709	0.559	0.815	−0.040	0.229	0.358	0.538	0.530	0.399	0.983	
17.5	0.642	0.571	0.212	−0.029	0.635	0.845	0.655	1.107	0.746	1.015	1.727	1.134	0.966	0.514	1.252	1.605	1.697	0.913	1.295	0.930	0.841	0.696	1.398	0.780	0.572	0.836	−0.254	−0.203	0.483	0.571	0.386	0.350	1.048	
18.0	0.520	0.576	−0.438	−0.155	0.728	0.792	0.670	1.023	0.719	0.857	1.731	0.630	0.672	0.518	0.901	1.877	1.373	0.819	1.230	1.001	0.715	0.724	1.411	0.717	0.469	0.860	0.065	0.421	0.329	0.558	0.589	0.364	0.983	
18.0	0.586	0.559	−0.238	−0.121	0.680	0.794	0.657	1.030	0.685	0.908	1.846	0.750	0.770	0.639	0.975	1.707	1.466	0.838	1.259	0.989	0.748	0.669	1.426	0.709	0.505	0.817	−0.012	0.225	0.385	0.620	0.514	0.421	0.990	
18.0	0.467	0.501	−0.787	−0.078	0.747	0.749	0.611	1.003	0.633	0.975	2.103	0.415	0.571	0.686	0.758	2.242	1.244	0.770	1.051	1.015	0.692	0.629	1.622	0.646	0.373	0.779	0.266	0.760	0.228	0.706	0.743	0.540	0.987	
19.0	0.533	0.534	−0.356	−0.257	0.675	0.802	0.649	1.064	0.664	0.787	1.892	0.687	0.681	0.655	0.936	1.832	1.439	0.832	1.206	0.972	0.599	0.719	1.450	0.687	0.470	0.826	0.017	0.343	0.347	0.685	0.582	0.433	0.961	
19.0	0.491	0.598	−0.540	−0.123	0.775	0.770	0.710	1.023	0.708	0.897	1.673	0.563	0.623	0.583	0.885	1.942	1.325	0.812	1.139	0.994	0.745	0.702	1.410	0.683	0.446	0.853	0.101	0.530	0.271	0.541	0.622	0.403	0.980	
19.5	0.588	0.561	−0.538	−0.211	0.633	0.822	0.686	0.977	0.681	0.821	1.834	0.567	0.617	0.640	0.882	2.029	1.490	0.799	1.238	1.042	0.691	0.744	1.441	0.673	0.493	0.851	0.125	0.540	0.396	0.566	0.668	0.420	1.015	
19.0	0.512	0.496	−0.509	−0.150	0.660	0.765	0.621	1.015	0.561	0.877	2.168	0.572	0.656	0.691	0.853	2.408	1.441	0.788	1.265	1.011	0.717	0.606	1.516	0.542	0.398	0.808	0.105	0.490	0.373	0.755	0.823	0.623	0.969	
19.0	0.391	0.587	−0.588	−0.098	0.699	0.683	0.631	1.097	0.639	0.921	1.882	0.518	0.625	0.590	0.832	2.253	1.407	0.795	1.190	0.938	0.693	0.639	1.663	0.653	0.440	0.809	0.127	0.586	0.339	0.722	0.733	0.465	0.979	

Table A1. – *continued.*

#SpT	H2OA	H2OB	K1	K2	H2OJ	CH4J	H2OH	CH4H	H2OK	CH4K	H2O15	KJ	KH	YJ	HJ	H2Oc	Jcont	Hcont	FeHJ	FeHH	CO	H2OD2	H2O	H2OD	H2O1	H2O2	sHJ	sKJ	sH2OJ	sH2OH1	sH2OH2	sH2OK	VOz	Target
11.0	0.673	0.742	−0.640	−0.080	0.934	0.910	0.816	1.154	1.058	1.001	1.253	0.440	0.634	0.692	0.765	1.446	1.171	1.030	0.957	0.897	0.770	0.909	1.198	1.261	0.620	0.808	0.238	0.647	0.123	0.358	0.272	0.053	1.224	
12.0	0.779	0.910	−0.627	−0.074	1.034	0.968	0.868	1.065	0.902	1.005	0.926	0.464	0.617	0.559	0.831	1.085	1.117	1.042	0.812	0.941	0.779	0.829	1.175	1.202	0.734	0.795	0.209	0.631	−0.002	−0.067	0.153	0.116	1.115	
14.5	0.788	0.839	−0.336	0.015	0.950	1.023	0.817	1.251	0.991	1.060	1.014	0.707	0.750	0.550	0.958	1.003	1.287	1.092	0.901	0.819	0.739	0.886	1.278	1.162	0.699	0.948	0.009	0.364	0.132	0.220	0.034	−0.045	1.268	
13.0	0.640	0.659	−0.319	−0.045	0.781	0.890	0.748	1.219	0.937	1.019	1.349	0.641	0.752	0.530	0.957	1.382	1.399	1.002	1.012	0.851	0.773	0.817	1.305	0.975	0.608	0.827	0.030	0.328	0.302	0.462	0.261	0.164	1.290	
13.0	0.794	0.882	−0.354	−0.138	0.966	0.973	0.868	1.070	0.958	0.924	0.945	0.610	0.712	0.439	0.937	0.882	1.228	1.021	0.876	0.933	0.702	0.792	1.270	1.247	0.744	0.813	0.103	0.356	0.083	0.047	−0.038	0.094	1.026	
15.0	0.708	0.687	0.006	−0.047	0.688	0.930	0.775	1.181	0.947	0.995	1.454	0.986	0.866	0.475	1.187	1.265	1.591	0.979	1.187	0.868	0.747	0.932	1.189	0.924	0.690	0.958	−0.168	0.012	0.442	0.516	0.161	0.076	1.212	
11.5	0.586	0.644	−0.692	0.014	0.794	0.875	0.779	1.146	0.904	1.088	1.492	0.449	0.595	0.628	0.805	2.344	1.306	0.933	1.039	0.905	0.715	0.755	1.268	0.930	0.563	0.857	0.189	0.718	0.249	0.504	0.586	0.175	1.274	
12.0	0.700	0.777	−0.635	−0.016	0.949	0.934	0.818	1.223	0.994	1.033	1.172	0.487	0.643	0.604	0.799	1.262	1.217	1.069	0.955	0.855	0.720	0.886	1.202	1.112	0.648	0.926	0.201	0.666	0.162	0.240	0.200	0.012	1.259	
16.0	0.662	0.664	−0.248	−0.073	0.806	0.933	0.797	1.171	0.963	0.986	1.343	0.675	0.764	0.571	0.976	1.662	1.387	0.999	1.047	0.888	0.829	0.864	1.249	1.063	0.628	0.834	0.021	0.278	0.299	0.503	0.309	0.133	1.361	
14.5	0.662	0.723	−0.335	−0.003	0.827	0.923	0.793	1.187	0.917	1.054	1.442	0.695	0.745	0.615	0.959	1.321	1.343	0.978	1.034	0.865	0.712	0.882	1.255	0.969	0.605	0.912	0.016	0.349	0.252	0.486	0.230	0.110	1.308	
14.5	0.653	0.654	−0.184	−0.168	0.761	0.908	0.794	1.169	0.999	0.907	1.566	0.692	0.768	0.408	1.014	1.079	1.502	0.983	1.124	0.905	0.825	0.839	1.217	1.161	0.603	0.802	−0.009	0.210	0.428	0.598	0.093	0.145	1.274	
99.9	0.818	0.831	0.130	−0.158	0.848	1.032	0.844	1.055	1.019	0.873	1.199	1.082	0.899	0.388	1.191	1.001	1.532	1.017	1.133	0.967	0.727	0.910	1.069	1.124	0.817	0.981	−0.175	−0.105	0.316	0.153	−0.007	−0.029	1.123	
16.0	0.663	0.689	−0.181	−0.065	0.775	0.905	0.779	1.192	1.000	0.999	1.487	0.732	0.790	0.559	1.049	1.100	1.438	0.998	1.189	0.873	0.829	0.927	1.193	1.029	0.631	0.897	−0.059	0.196	0.426	0.505	0.097	0.140	1.253	
17.0	0.572	0.651	0.046	0.017	0.624	0.820	0.697	1.271	0.905	1.067	1.854	0.933	0.929	0.202	1.190	3.892	1.648	0.971	0.973	0.811	0.701	0.818	1.361	0.943	0.570	0.829	−0.170	−0.048	0.339	0.708	0.618	0.205	1.190	
17.0	0.698	0.716	0.076	−0.071	0.700	0.968	0.770	1.248	0.975	0.986	1.369	0.908	0.903	0.395	1.192	0.976	1.706	1.042	1.233	0.844	0.829	0.833	1.222	1.246	0.661	0.849	−0.163	−0.038	0.565	0.398	0.000	0.118	1.132	

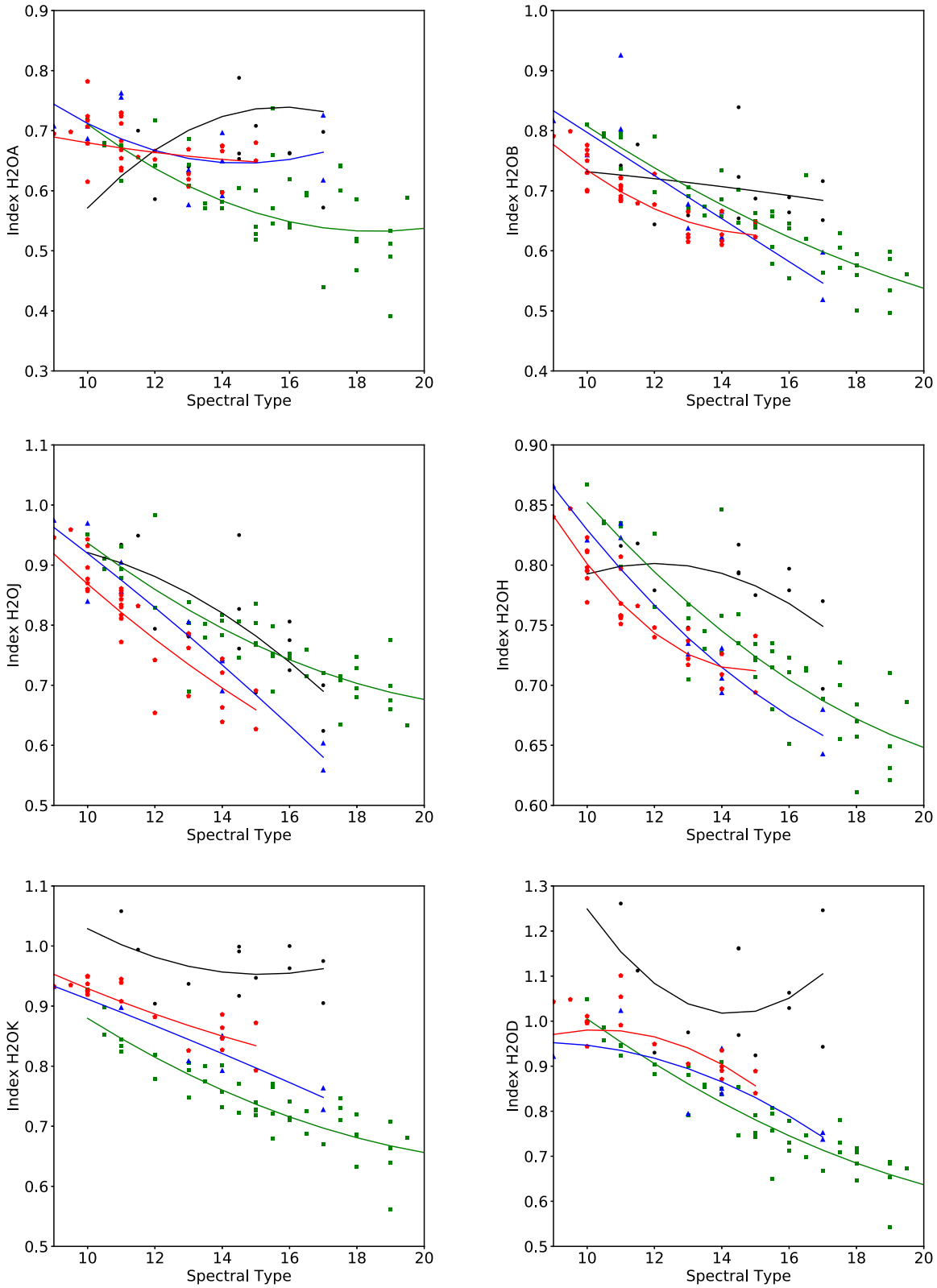

Figure A1. Near-infrared spectral indices defined in the literature versus NIR spectral types for our UpSco candidates (black dots), young L dwarfs (red filled symbols: β = triangles; γ = pentagons; Allers & Liu 2013; Bonnefoy et al. 2014; Gagné et al. 2015) and field L dwarfs (green symbols: Reid et al. 2001; Geballe et al. 2002; McLean et al. 2003; Knapp et al. 2004; Golimowski et al. 2004; Chiu et al. 2006).

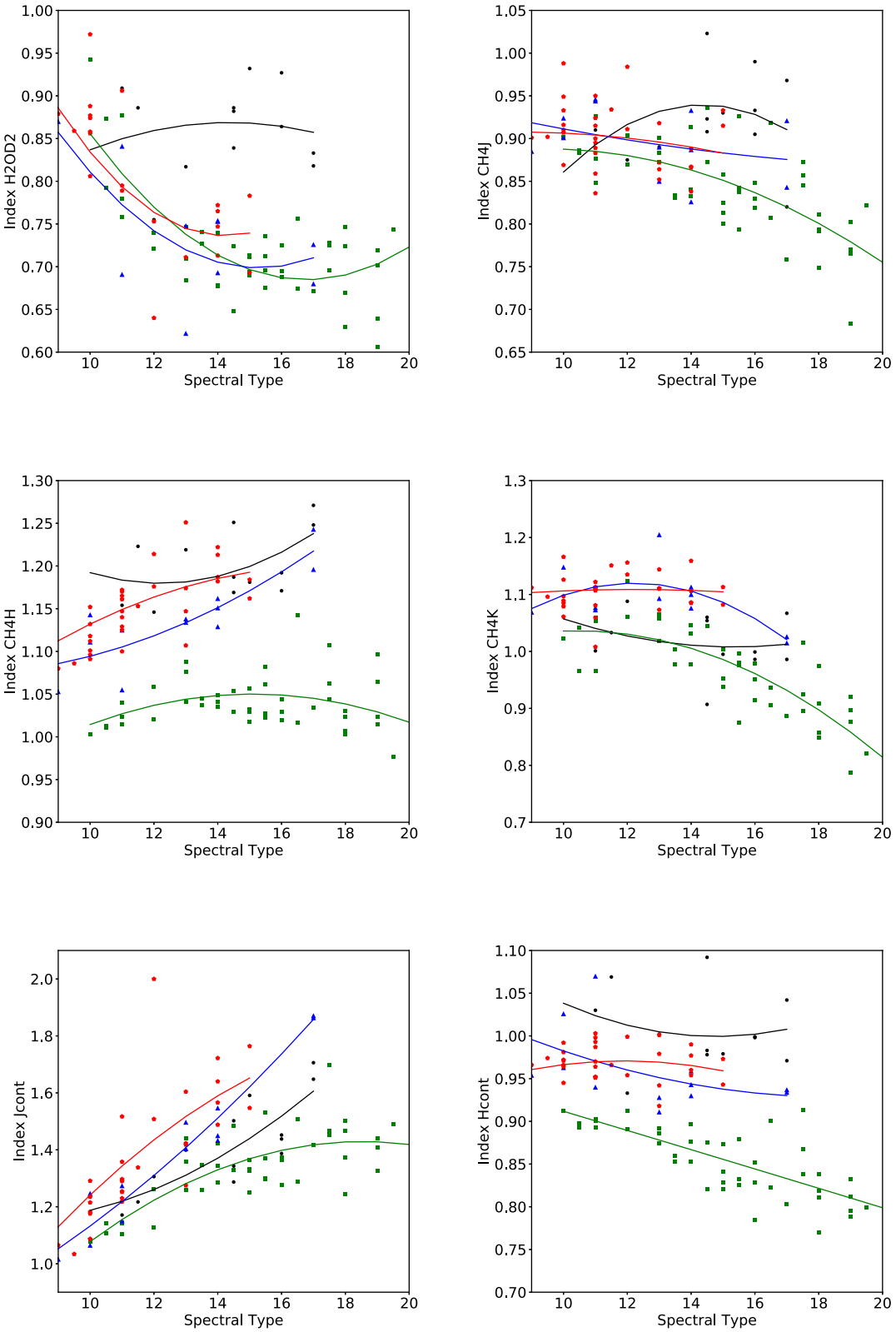

Figure A1 – *continued*

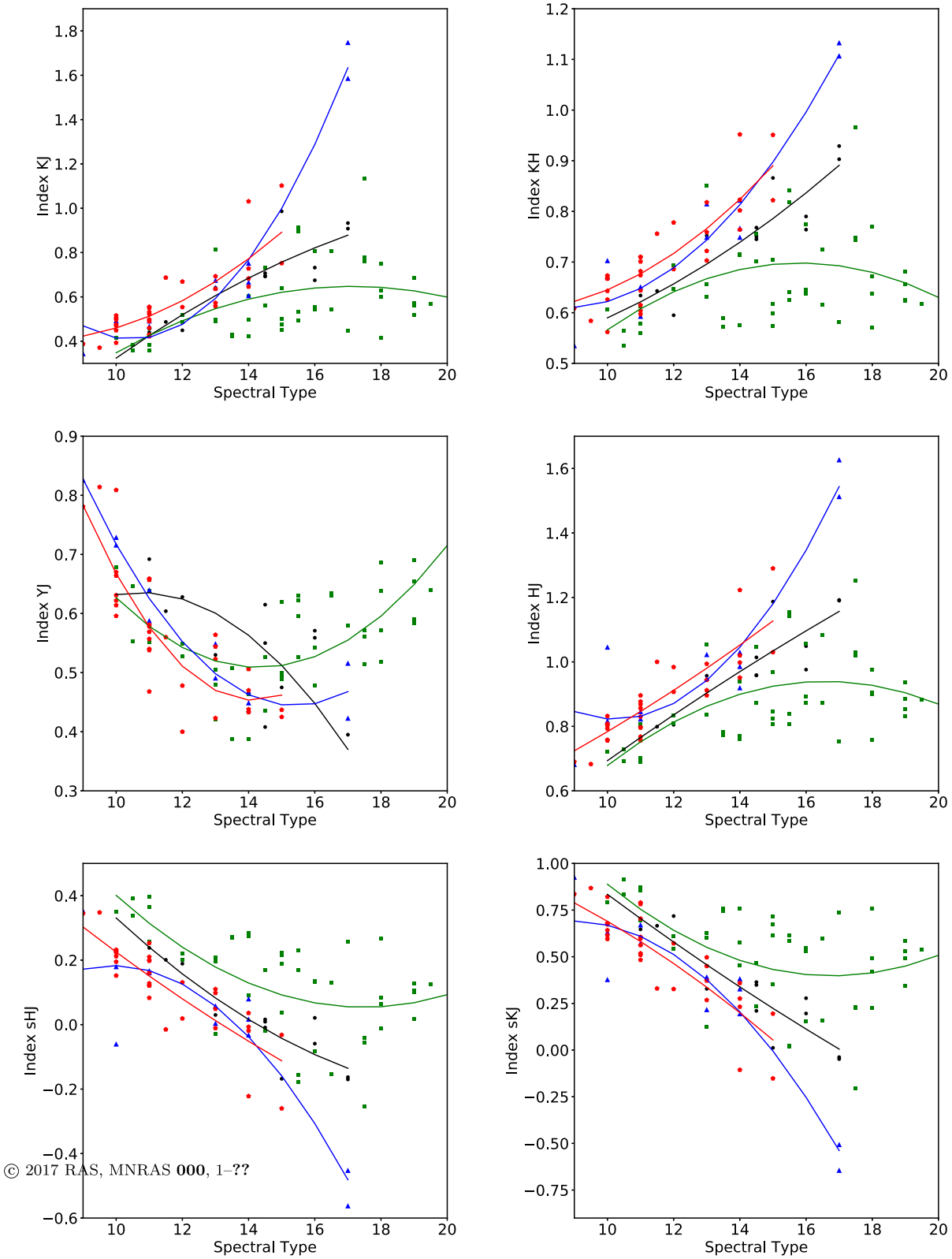

Figure A1 – *continued*

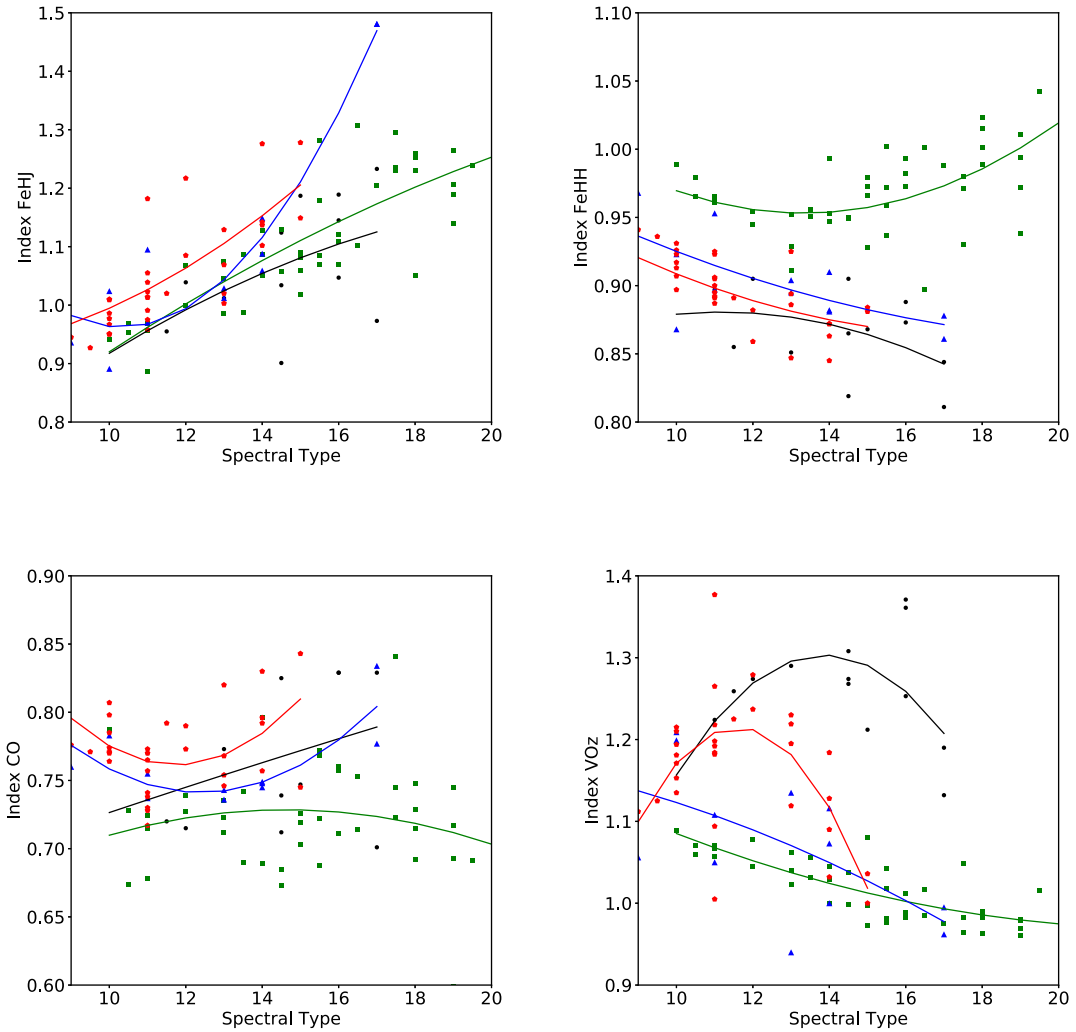

Figure A1 – *continued*

This paper has been typeset from a TEX/LATEX file prepared by the author.